Fall 9-5-2022

Electrocatalysis by Design: Low Dissolution Counter Electrode and Highly Efficient Nanostructured Electrocatalysts

Menna Hasan
menna.hasan@aucegypt.edu

The American University in Cairo
الجامعة الأمريكية بالقاهرة

Graduate Studies

Electrocatalysis by design: Low dissolution counter electrode and highly efficient nanostructured electrocatalysts

A THESIS SUBMITTED BY

Menna Hasan

TO THE

School of Science and Engineering

Nanotechnology program

5 September 2022

in partial fulfillment of the requirements for the degree of

PhD in Applied Sciences

Declaration of Authorship

I, Menna Hasan, declare that this thesis titled, "Electrocatalysis by design: Low dissolution counter electrode and highly efficient nanostructured electrocatalysts" and the work presented in it are my own. I confirm that:

- This work was done wholly or mainly while in candidature for a research degree at this University.
- Where any part of this thesis has previously been submitted for a degree or any other qualification at this University or any other institution, this has been clearly stated.
- Where I have consulted the published work of others, this is always clearly attributed.
- Where I have quoted from the work of others, the source is always given. With the exception of such quotations, this thesis is entirely my own work.
- I have acknowledged all main sources of help.
- Where the thesis is based on work done by myself jointly with others, I have made clear exactly what was done by others and what I have contributed myself.

Signed:

Menna Hasan

Date:

6 September 2022

Abstract

Water Electrolysis is one of the most promising techniques to generate H_2 gas, which is an alternative clean source of energy. Hydrogen provides almost three times the energy provided by gasoline, helping to solve the global warming problem caused by the currently used fossil fuels. As any electrochemical reaction is composed of two half reactions, a setup of working and counter electrodes is used to study the catalytic activity towards the targeted reaction, where each electrode carries one of the two-half reactions. In this dissertation, the stability of a number of the commonly used counter electrodes was examined to identify a stable counter electrode to avoid the deceptive enhancement caused by the dissolution and redeposition of the counter electrode on the working electrode during operation. Commercial titanium mesh has been introduced as an alternative emerging low-dissolution counter electrode, which was proven to be very stable and convenient to study the HER in acidic media. The second part of the dissertation focused on the working electrode, where various nanostructures were explored as catalysts for both hydrogen evolution reaction (HER) and oxygen evolution reaction (OER). First, boron carbon nitride (BCN) nanosheets were studied as an electrocatalyst for HER. BCN comprises the unique physicochemical properties of both graphene and 2D hexagonal boron nitride, including the electrical conductivity, mechanical, and chemical stability. Besides, the heteropolar bonding between N and B can improve its electroactivity. An innovative technique was introduced to fabricate 2D BCN hetero-structure nanosheets with various Cu:BCN weight ratios. The fabricated composites showed unique electrocatalytic properties for HER. Specifically, the overpotential of the 0.125 Cu-BCN composite at a current density of -10 mA/cm^2 vs RHE is 50% lower than that of pristine BCN. Moreover, C_{76} was investigated as a 0D catalyst, which showed tremendous enhancement in the catalytic HER activity due to the synergistic effect between C_{76} and nickel foam substrate. The C_{76}/Ni showed almost the same activity as the benchmark Pt/C catalyst. Finally, NiCoMnFe-phosphide nanosheets deposited on commercial Ti mesh were investigated as a ternary electrocatalyst for both HER and OER. The electrochemical measurements showed the NiCoMnFe-P composite to have the lowest overpotential towards HER (-200 mV) at -10 mAcm^{-2}, lowering the overpotential needed to drive the reaction by almost 40% for HER compared to that of blank Ti mesh. For overall water splitting, a cell voltage of 1.71 V was recorded at a current density of 10 mAcm^{-2}.

Acknowledgements

I thank Allah subhanahu wa ta'ala for all the blessings that He granted me. For blessing me with being a Muslim since birth, for sending his prophet Muhammad peace be upon him with the Quraan, for having a beautiful and loving family. I really appreciate their support, especially my mother and my father, who believed in me and sacrificed their needs so many times to push me a head and expand my potentials. I could not have made it without their care and guidance, and I ask Allah subhanahu wa ta'ala to reward them in this life and the afterlife. I also thank Allah for having a loving sister and brothers, who have been always the source of joy and comfort in my life.

I would also like to thank Dr. Nageh Allam not just for being my advisor, but for also being a mentor throughout my masters and PhD journeys. For expanding my limits and helping me discover new potentials in myself that I did not even know that I have, and for not letting me give up.

I am also very grateful to all EML group members, who taught me the real meaning of being brothers and sisters in Islam and how to be kind, helpful, and many other beautiful and precious meanings.

I also have the deepest gratitude to my schoolteachers, and college professors who taught me.

At the end I would like to thank Youssef Gameel Fellowship for funding my PhD degree.

Contents

List of Figures

List of Tables

List of Abbreviations

Abbreviation	Definition
BCN	Boron Carbon Nitride
SCE	Saturated Calomel electrode
LSV	Linear sweep voltammetry
CA	Chronoamperometry
CB	Conduction Band
CS	Crystallite size
CV	Cyclic Voltammetry
CVD	Chemical Vapor Deposition
DFT	Density Functional Theory
SHE	Standard Hydrogen Electrode
OER	Oxygen Evolution Reaction
ECSA	Electrochemical Surface Area
EDX	Energy Dispersive X-ray Spectroscopy
HER	Hydrogen Evolution Reaction
EIS	Electrochemical Impedance Spectroscopy
TOF	Turn Over Frequency
FESEM	Field Emission Scanning Electron Microscopy
FTIR	Fourier Transform Infrared Spectroscopy
XRD	X-ray diffraction
XPS	X-ray Photoelectron Spectroscopy
RCT	Series Resistance
RS	Charge Transfer Resistance
RHE	Reversible Hydrogen Electrode
TEM	Tunneling Electron Microscopy
XPS	X-ray Photoelectron Spectroscopy

CE	Counter Electrode
Ti mesh	Titanium mesh
Cu:BCN	Copper:Boron Carbon Nitride
rGO	Reduced Graphene Oxide
Cdl	Charge double layer

Chapter 1

Introduction

1.1 Energy crisis and the drawbacks of fossil fuels

The world nowadays mainly depends on fossil fuels as the main source of energy. Though, recent statistics expect that within 50 to 60 years, Fig. 1, the world will suffer from fossil fuels shortage, which will create an energy crisis.[1–3] Moreover, fossil fuels are the main source of CO_2 gas, which is one of the main causes of global warming.[4] Figure 2 illustrates the world energy consumption of fossil fuel and renewable energy in 2015, where 85% of the world's energy consumption is based on fossil fuels. Thus, the need for alternative sources of energy that do not have any of the disadvantages of the currently used fossil fuels became a necessity. In this regard, researchers started to adapt H_2 gas as a potential candidate that fulfills these requirements and provides three times the energy provided by gasoline.[5]

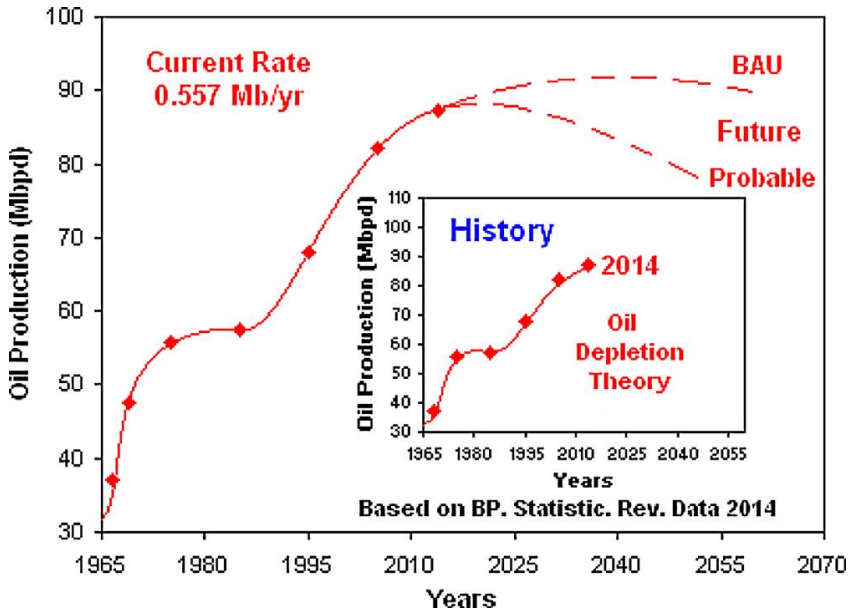

Figure 1 The change in the global oil production along the last 100 years.[1]

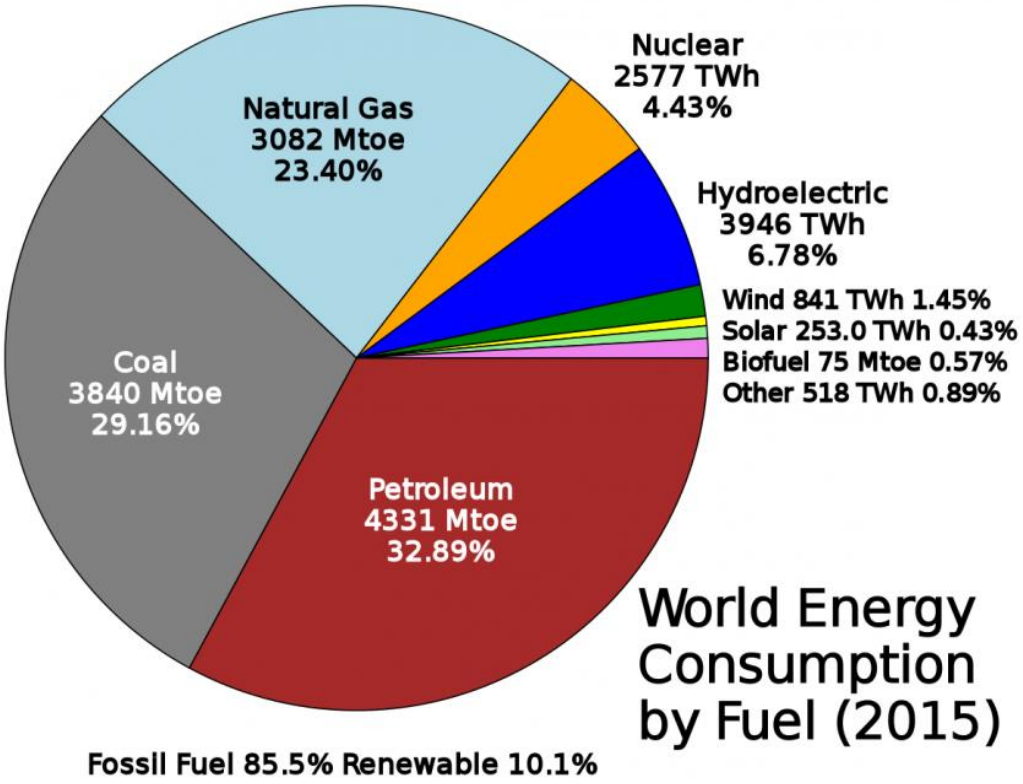

Figure 2 World energy consumption of fossil fuel and renewable energy (2015).[6]

1.2 Hydrogen production techniques

A variety of techniques are being explored to drive the water splitting reaction and produce hydrogen gas. These techniques include photocatalytic water splitting,[7,8] hydrocarbons steam reforming,[9–11] hydrolysis of earth metal borohydrides/hydrides,[12] and water electrolysis.[13] Although all these techniques are explored to produce H_2 gas, the application of many of them is limited. For instance, despite the fact that photocatalytic water splitting is considered a green method for H_2 production, the production rate is still very low (less than 100 mL, even after a few days), making photocatalytic water splitting the least promising approach to generate H_2 gas on large scale.[14,15] Despite the fact that hydrocarbon steam reforming is currently used for large scale production of H_2 gas, it requires high temperature and high pressure, making it as dangerous as fossil fuels, threatening both human health and the environment.[10,11] Another disadvantage of steam reforming technique is the low quality of the H_2 produced, as oxides od C,S, and N are usually obtained as byproducts. This hinders the use of the hydrogen produced from steam

reforming in fuel cells, as these impurities cause active sites poisoning and dramatically reduce the life cycle of the fuel cell.[16,17] As for the hydrolysis of metals, this technique is considered a rapid method for generating large amounts of the H_2 gas. Nevertheless, the metals used are usually toxic. Besides, the production of metal hydrides and borohydrides usually involves industries that contribute to environment pollution.[18,19] Figure 3 demonstrates the setup of one of the reactors used for hydrogen production via metal hydrides.[20]

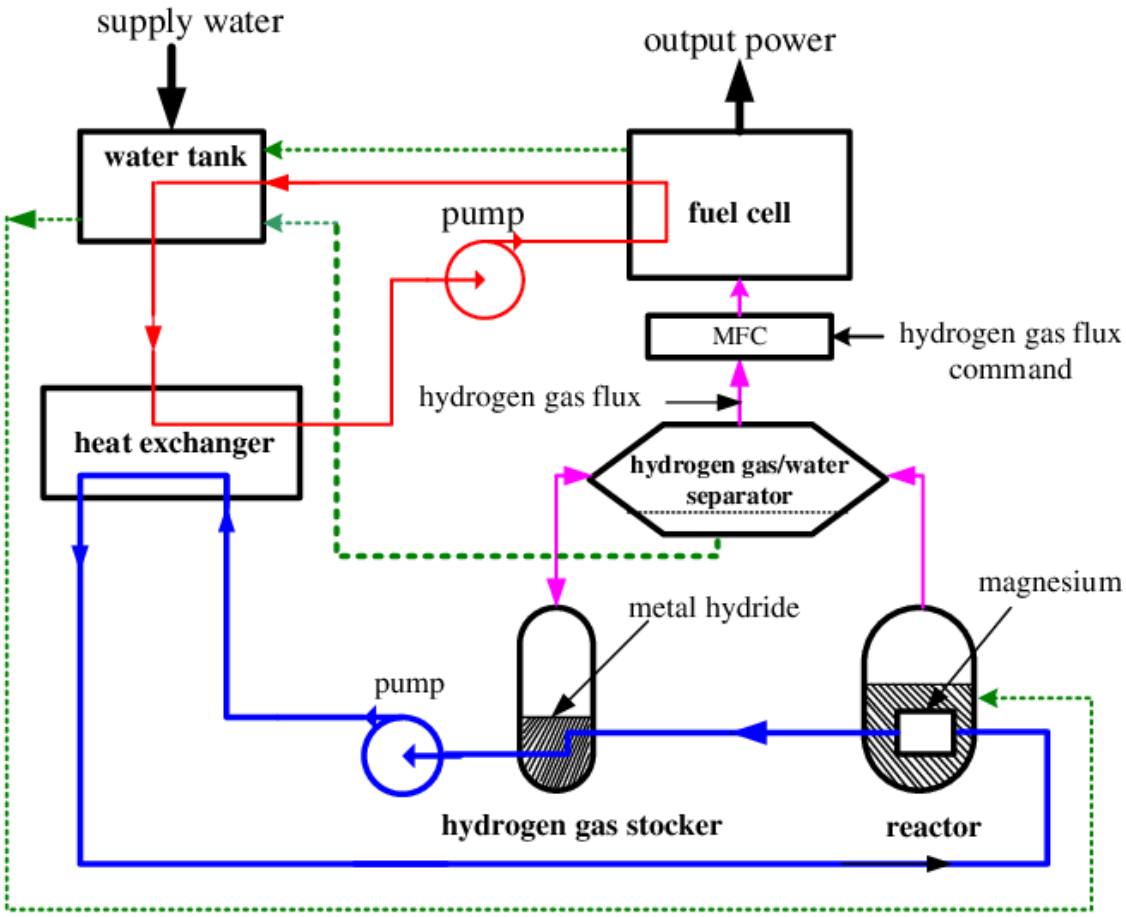

Figure 3 setup of the proposed reactor used for hydrogen production via metal hydrides.[20]

This leaves us with electrolysis, which is considered the best method for producing H_2 gas on large scale in short periods with high purity, avoiding the harmful effects on the environment that are possible from other techniques. Figure 4 shows the simplicity of the setup used in water electrolysis technique.[21] Therefore, through the past few years, many studies devoted to enhance the performance of the electrolysis process.

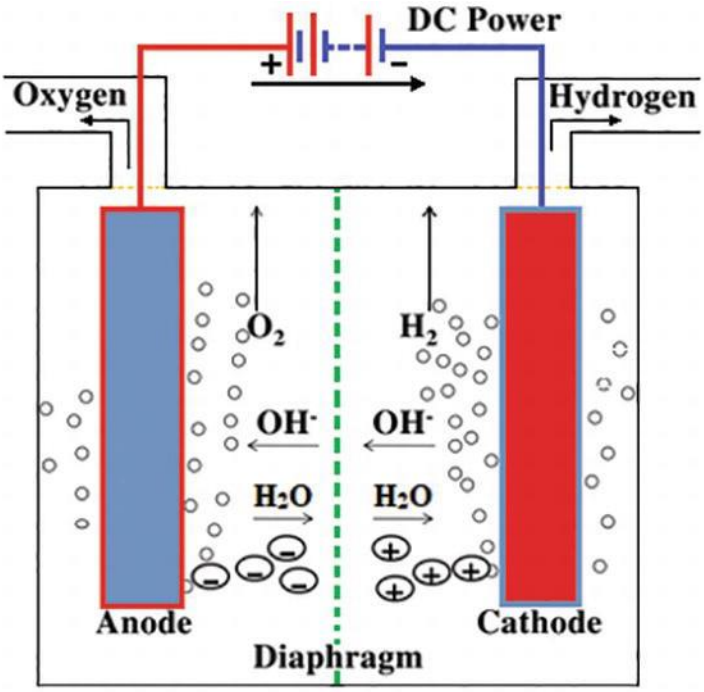

Figure 4 Schematic representation of the electrolysis setup.[21]

1.3 Water electrolysis technology

Water electrolysis is an energy conversion technology that uses electricity to generate hydrogen gas from water via decomposing the water molecule (H_2O) into H_2 and O_2 gas, as illustrated in Figure 5. However, due to the sluggish kinetics of the targeted reactions, an active catalyst is needed to speed up the kinetics of the reaction and accordingly achieve higher conversion rates. Thus, electrocatalysis is adapted as an approach for secondary storage of energy.[17] However, there is an increasing demand for new stable, earth abundant, and nonprecious catalysts that can substitute noble metals, which are the benchmark catalysts for water electrocatalysis.[22]

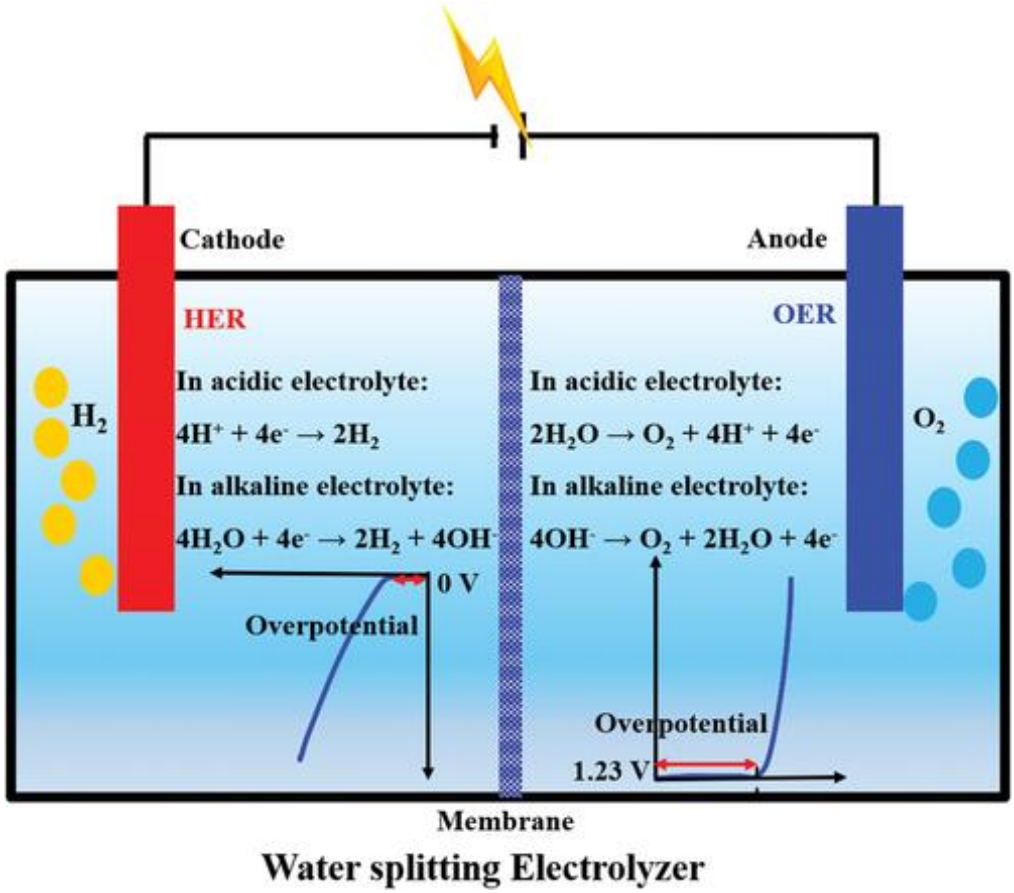

Figure 5 Schematic representation of electrocatalytic water-splitting setup and the possible reaction kinetics in acidic and alkaline media.[22]

1.4 Thesis scope and organization

The aim of this dissertation is to study the setup used for electrolysis and fabricate highly efficient electrocatalysts that possess high catalytic activity with long-term stability. Water electrolysis is one of the most promising techniques that can be used to generate H_2 gas, which is an alternative source of energy that is clean and provides almost three times the energy provided by gasoline, helping to solve the problem of global warming caused by the currently used fossil fuels.

As any electrochemical reaction is composed of two half reactions, thus a setup of working and counter electrodes is used to study the catalytic activity towards the targeted reaction, where each electrode carries one of the two-half reactions. In this thesis, first, the stability of a number

of the commonly used counter electrodes was investigated. In this regard, a stable counter electrode that resists electrochemical dissolution is demonstrated, which helps to avoid the deceptive catalytic enhancement caused by the dissolution and redeposition of the counter electrode on the working electrode. Then, the rest of the dissertation focuses on the working electrode, where various nanostructures were explored as catalysts for both hydrogen evolution reaction (HER) and oxygen evolution reaction (OER). A summary of each chapter in this dissertation is discussed in the following sections.

Chapter 1:

This chapter introduces the energy problem and the effectiveness of hydrogen gas as an alternative energy source. The various techniques used to generate hydrogen gas were discussed with their pros and cons. Finally, the electrolysis technique, which is the core of this dissertation, is demonstrated as the most promising technique for hydrogen production.

Chapter 2:

In this chapter the theoretical background needed to understand the chemistry behind electrolysis, along with the different mechanisms of HER and OER in alkaline and acidic media. Besides, the different electrochemical activity parameters used to study the fabricated catalysts in water electrolysis reaction were presented. Moreover, the different approaches used for electrode fabrication and their advantages and disadvantages are discussed in detail.

Chapter 3:

This chapter represents the literature review of the main challenges in electrochemical water splitting and discussed the proposed solutions. Finally, the research conducted in the recent few decades, the different catalysts, and different structures explored are reviewed.

Chapter 4:

In this chapter, the methodology and the experimental work of each study in this dissertation are presented in detail. Also, the different characterization techniques used throughout the thesis are discussed.

Chapter 5,6,7, and 8 present the results and discussion of the performed research in this dissertation.

Chapter 5:

This chapter investigated the stability of different counter electrodes, highlighting the importance of identifying a stable counter electrode that does not interfere with the obtained results and proposing a low dissolution counter electrode.

Chapter 6:

This chapter introduces a novel methodology to fabricate one of the 2D carbon-based materials, which is boron carbon nitride loaded with different amounts of copper. This material was then tested for hydrogen evolution reaction in acidic medium. Also, the effect of copper loading and the phenomenon of electrochemical exfoliation are studied in detail.

Chapter 7:

In this chapter, the electrocatalytic activity of another carbon-based structure is investigated, which is fullerene (C_{76}). Also, the synergy between C_{76} and nickel foam substrate, as a highly efficient HER catalyst in acidic medium, has been demonstrated and discussed.

Chapter 8:

This chapter demonstrates the fabrication of nanosheets of different combinations of Ni, Co, Mn, and Fe via electrodeposition over commercial Ti mesh. Then, their catalytic activity was tested for HER, OER, and overall water splitting.

Chapter 9:

In this chapter, the conclusion of the conducted research is summarized along with some suggested ideas for future research.

Chapter 2

Theoretical background

This chapter discusses the theoretical background of water electrolysis in different media, along with the key activity parameters used to evaluate the catalytic activity of the catalyst used to perform HER and OER. These parameters include: overpotential (η), Tafel slope, exchange current density (j_0), mass activity, specific activity, electrochemically active surface area (ECSA), turnover frequency (TOF), and faradaic efficiency (FE).

2.1 Basic principles of electrocatalytic water splitting

Water electrolysis is a nonspontaneous reaction, as illustrated in equation 1. Theoretically, under equilibrium conditions, we need to provide the system with 1.23 V vs. SHE to drive water splitting reaction.[23]

$$\mathbf{H_2O(l) \longrightarrow H_2(g) + 1/2O_2(l) \qquad E_0 = 1.23\ V\ vs.\ SHE} \qquad (1)$$

Usually, water electrolysis is carried out in highly alkaline conditions or highly acidic conditions, as these conditions help lowering the energy losses due to the presence of free H^+ and OH^- ions in the electrolyte.[13,24,25] Yet, both conditions show some limitations towards one of the two half reactions. For instance, despite the high efficiency of HER in acidic medium, OER requires high overpotentials except if the reaction is catalyzed by oxides of very expensive metals such as Ir or Ru.[26,27] That is why the bench mark catalysts for electrocatalysis are based on rare and noble metals, such as Ru and Ir for OER and Pt for HER.[25,28,29] Nevertheless, despite the excellent catalytic activity of these materials, when used for large scale production, the price of the produced H_2 per unit volume is very high due to the use of rare and precious metals.[22,30]

2.2 The effect of pH on water electrolysis

The pH of the electrolyte used is another parameter that completely changes the mechanism of OER and HER. In acidic electrolytes, H^+ ions bond for HER and H_2O is formed for oxygen evolution. While in alkaline electrolytes, OH^- bond to the electrode surface for OER and H_2O bonds on it for HER. This makes OER more feasible in alkaline medium, while HER is more favorable in acidic medium.[31] One limitation is the corrosive nature of the electrolytes, which hinders the long term stability of the electrodes. Thus, the goal is to decrease the overpotentials to be able to achieve efficient water splitting for large scale production and to lower the external energy applied to perform the reaction and finally to make a durable and stable electrode.[32]

2.2.1 Water electrolysis in acidic medium

Under acidic conditions, the following reactions take place, equations (2) and (3).[33–35]

$$\mathbf{2H_2O(l) \rightarrow 4H^+(aq) + 4e^- + O_2(g)} \qquad \textbf{(at anode)} \qquad \textbf{(2)}$$

$$\mathbf{4e^- + 4H^+(aq) \rightarrow 2H_2(g)} \qquad \textbf{(at cathode)} \qquad \textbf{(3)}$$

2.2.2 Water electrolysis in alkaline medium

While in alkaline medium, the reaction takes a different pathway.

$$\mathbf{OH^-(aq) \rightarrow 2H_2O(l) + 4e^- + 2O_2(g)} \qquad \textbf{(at anode)} \qquad \textbf{(4)}$$

$$\mathbf{4e^- + 4H_2O(l) \rightarrow 4OH(aq) + 2H_2(g)} \qquad \textbf{(at cathode)} \qquad \textbf{(5)}$$

2.3 Mechanisms of OER:

Many mechanisms were proposed for OER, as it is a four-electron reaction. For OER in acidic medium, four mechanisms were suggested, which are the oxide, electrochemical oxide, the Krasil'shchiko, and Hackerman's mechanism, as described by equations (6-17)

Electrochemical oxide path:[36]

$$S + H_2O \rightarrow S\text{–}OH + H^+(aq) + e^- \quad (6)$$

$$S\text{–}OH \rightarrow S\text{–}O + H^+(aq) + e^- \quad (7)$$

$$2S\text{–}O \rightarrow 2S + O_2(g) \quad (8)$$

Oxide path:[36]

$$S + H_2O \rightarrow S\text{–}OH + H^+(aq) + e^- \quad (9)$$

$$2S\text{–}OH \rightarrow S\text{–}O + S + H_2O \quad (10)$$

$$2S\text{–}O \rightarrow 2S + O_2(g) \quad (11)$$

Krasil'shchkov path:[37]

$$S + H_2O \rightarrow S\text{–}OH + H^+(aq) + e^- \quad (12)$$

$$S\text{–}OH \rightarrow S\text{–}O^- + H^+(aq) \quad (13)$$

$$S\text{–}O^- \rightarrow S\text{–}O + e^- \quad (14)$$

$$2S\text{–}O \rightarrow 2S + O_2(g) \quad (15)$$

Wade and Hackerman's path:[38]

$$2S + 2H_2O \rightarrow S\text{–}O + S\text{–}H_2O + 2H^+(aq) + 2e^- \quad (16)$$

$$S\text{–}O + 2S\text{–}OH^- \rightarrow S\text{–}H_2O + 2S + O_2(g) + 2e^- \quad (17)$$

On the other hand, for alkaline medium, there are five mechanisms suggested for OER. These mechanisms are the oxide, electrochemical oxide, the Krasil'shchkov, Yeager's pathway

and Bockris mechanism. The steps of each mechanism is illustrated in equations (18-34)

Electrochemical oxide path:[36]

$$\mathbf{S + OH^-(aq) \rightarrow S{-}OH + e^-} \quad \mathbf{(18)}$$

$$\mathbf{S{-}OH + OH^-(aq) \rightarrow S{-}O + H_2O + e^-} \quad \mathbf{(19)}$$

$$\mathbf{2S{-}O \rightarrow 2S + O_2(g)} \quad \mathbf{(20)}$$

Oxide path:[36]

$$\mathbf{S + OH^-(aq) \rightarrow S{-}OH + e^-} \quad \mathbf{(21)}$$

$$\mathbf{2S{-}OH \rightarrow S{-}O + S + H_2O} \quad \mathbf{(22)}$$

$$\mathbf{2S{-}O \rightarrow 2S + O_2(g)} \quad \mathbf{(23)}$$

Krasil'shchkov path:[37]

$$\mathbf{S + OH^-(aq) \rightarrow S{-}OH + e^-} \quad \mathbf{(24)}$$

$$\mathbf{S{-}OH + OH^-(aq) \rightarrow S{-}O^- + H_2O} \quad \mathbf{(25)}$$

$$\mathbf{S{-}O^- \rightarrow S{-}O + e^-} \quad \mathbf{(26)}$$

$$\mathbf{2S{-}O \rightarrow 2S + O_2(g)} \quad \mathbf{(27)}$$

Yeager's path:[39]

$$\mathbf{S + OH^-(aq) \rightarrow S{-}OH + e^-} \quad \mathbf{(28)}$$

$$\mathbf{S_z{-}OH \rightarrow S_{z+1} - OH + S + e^-} \quad \mathbf{(29)}$$

$$2S_{z+1}\text{–OH} + 2OH^-(aq) \rightarrow 2S + 2H_2O + O_2(g) \quad (30)$$

Bockris path:[33]

$$S + OH^-(aq) \rightarrow S\text{–OH} + e^- \quad (31)$$

$$S\text{–OH} + OH^-(aq) \rightarrow S\text{–}H_2O_2 + e^- \quad (32)$$

$$S\text{–}H_2O_2 + OH^-(aq) \rightarrow S\text{–}O_2H^- + H_2O \quad (33)$$

$$S\text{–}H_2O_2 + S\text{–}O_2H^- \rightarrow 2S + OH^-(aq) + O_2(g) \quad (34)$$

2.4 Mechanisms of HER

The mechanistic steps for HER are based on the adsorption and desorption of hydrogen. Thus, the mechanism is straightforward. The first step of the HER is hydrogen adsorption, known as the Volmer step. The second step involves hydrogen desorption from the electrode surface, known as 'Volmer–Heyrovsky' step if it involves electrochemical desorption, and if it involves chemical desorption it is called 'Volmer–Tafel' step. Thus, the type of the desorption step is mainly determined by the exposed active surface area.[16]

Tafel Mechanism:

This mechanism involves the adsorption and discharge of H^+, then chemical desorption of H_2, equations (35)&(36).

$$H^+(aq) + S + e^- \rightarrow S\text{-}H \quad (35)$$

$$2\ S\text{–}\ H \rightarrow H_2(g) + 2S \quad (36)$$

Volmer–Heyrovsky Mechanism:

This mechanism involves the adsorption and discharge of H^+, followed by the adsorption

of another proton on the same site, then the discharge and chemical desorption of H_2, equations (37),(38), and (39).

$$H^+_{(aq)} + S + e^- \rightarrow S–H \quad (37)$$

$$S–H + H^+_{(aq)} \rightarrow S–H–H^+ \quad (38)$$

$$S–H–H^+ + e^- \rightarrow H_{2(g)} + S \quad (39)$$

Different intermediates are involved in this reaction, such as metal–oxide, hydroxide, or oxy-hydroxide. In case of 3d-transition metals, the catalytic activity is determined by the electron density of the eg and t_{2g} orbitals. Which affects the intercalation of –OH ions and O_2 cleavage at the surface of the electrode, affecting the overall OER activity. For an efficient OER, the –OH group should stay bound to the electrode until O_2 is formed, then -OH should split effectively. This makes the iron group metals very convenient as a catalyst for OER, copper is also a very good candidate due to its high electron density which hinders the interaction of -OH. Thus, transition metals- based nanostructures are being extensively investigated due to their promising performance in OER.[16]

2.5 Activity parameters of water electrolysis

The following section summarizes the basic electrochemical parameters that is usually used to evaluate the electrocatalytic behavior of the fabricated catalysts in water electrolysis.

2.5.1 Overpotential

As we mentioned previously, electrocatalytic water splitting is a very promising technique compared to other water splitting techniques. However, as the water molecule is thermodynamically stable there are some limitations. According to thermodynamics water splitting reaction is non-spontaneous with the free energy change ΔG of +237 kJ mol^{-1}.[23] Thus, water is not susceptible to splitting into hydrogen and oxygen. For hydrogen evolution reaction, the standard reduction potential is 0 V vs. RHE, while for the oxygen evolution reaction it is 1.23 V. Therefore, theoretically the potential needed to perform the water splitting reaction is 1.23 V. However, due to the external resistances such as the connections of the external circuit, the electrolyte, the conductivity of electrodes, and the distance between the electrodes, besides, the

kinetic steps of both OER and HER drag the excess potentials, all these factors are generally called overpotentials. Besides, the OER is too complicated, as it involves four-proton coupled electron transfer reactions and each reaction causes additional overpotentials.

2.5.1.1 Overpotential at a specific current density (η)

Overpotential is considered the most important activity parameter in water electrolysis.[26] It is usually defined as " the additional potential needed to drive an electrochemical reaction from its reversible potential", the reversible potential of HER is 0, while for OER it is 1.23 V vs. SHE. There for, the overpotential of the two half reactions can be obtained from the equations (40)&(41).

$$\eta_{OER} = E_{RHE} - 1.23\ V \qquad (40)$$

$$\eta_{HER} = E_{RHE} - 0\ V \qquad (41)$$

2.5.1.2 IR drop compensated overpotential (η_{IR})

As electrolysis is usually carried in a three electrode cells, the solution resistance, which is affected by the distance between the counter and the reference electrode, and the ionic strength of the electrolyte causes a reduction in the potential, most researchers apply IR compensation to eliminate the effect of solution resistance. IR drop stands for ($I_{cell} \times R_u$) compensation is usually calculated by multiplying the value of the recorded uncompensated resistance (R_u) by the current density (I_{cell}), then subtracting the resulting value from the experimentally recorded potential. However, for large scale production, the reaction does not work based on IR corrected overpotentials. Most of the overpotentials reported in the published studies are IR corrected, thus, it is very crucial to report both IR compensated and IR uncompensated currents, or at least report the percentage of IR drop compensation.

2.5.2 Tafel slope and exchange current density

Electrons transfer at the electrode/electrolyte interface is determined by the Tafel slope values. There are different methods used to extract Tafel slopes the often used one is from the polarization curves, by plotting the logarithm of the current density against the overpotential, the

Tafel slope value are taken from the values observed in this plot. Tafel slope values help determining the kinetics of different electrodes, besides comparing their activities and their overpotentials. For OER, which involves four-electron transfer at the interface, the value should be around 30 mV dec^{-1}.[40] For HER, the values of the observed Tafel slope reveal whether the electrode undergoes chemical or electrochemical desorption. For instance, If the value is close to 30 mV dec−1, this means that the electrode follows chemical desorption, this behavior is observed in Pt-based catalysts. Therefore, the values of Tafel slope is a feasible way to understand the charge transfer kinetics among different electrodes.[32,40]

Tafel analysis is usually used to understand the kinetics of OER and HER.[41] The Tafel equation is derived from the Buttler-Volmer equation, equation (37) :

$$\mathbf{I = I_0[exp\ (\frac{\alpha_A nF}{RT} \times \eta) - exp\ (\frac{\alpha_C nF}{RT} \times \eta)} \qquad \mathbf{(42)}$$

Where, I is the current, I_0 is the exchange current (current at equilibrium potential), α_A and α_C are the charge transfer coefficients for the anodic and cathodic reactions, respectively, n is the number of electrons transferred, F is the Faraday constant (96485 C), R is the ideal gas constant, T is the absolute temperature in K, η is the overpotential.

Under equilibrium conditions, the cathodic and anodic terms are equal, and the observed current I is equal to I_0. Furthermore, at high overpotentials, Buttler-Volmer equation is simplified to the Tafel equations of the anodic and cathodic curves, equations (38) & (39):

$$\mathbf{lnI = ln\ I_0 + (\frac{\alpha_A nF}{RT} \times \eta)} \qquad \mathbf{(43)}$$

$$\mathbf{lnI = ln\ I_0 + (\frac{\alpha_C nF}{RT} \times \eta)} \qquad \mathbf{(44)}$$

These two equations have the form of (y = b + mx). Thus, by plotting log I, vs. η, we get what is known as the Tafel plot. As demonstrated in Figure 6, the slope of the linear part represents Tafel slope. While the intercept of the linear part on the x-axis represents (j_0), which is the exchange current density at 1.23 and 0 for OER and HER, respectively. Usually, lower Tafel

slopes indicate faster reaction kinetics. However, it is important to notice that Tafel relationship works for totally irreversible kinetics, and it requires the absence of mass transfer effect on the recorded current. Thus, when the kinetics of the reaction are slow and large activation overpotential is needed, Tafel slope can be representative of the reaction kinetics.[42]

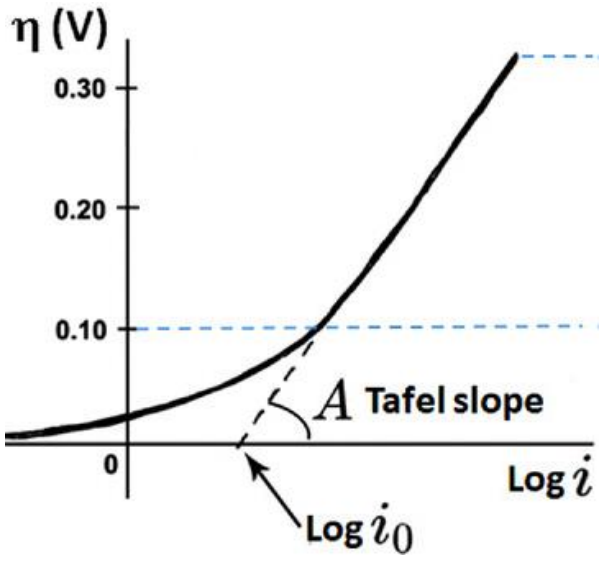

Figure 6 Tafel plot.[43]

2.5.3 Mass and specific activities

The catalytic activity of the electrodes is strongly affected by the loading of the catalyst. Thus, it is very important to find the relationship between the observed current densities and the loadings of the catalyst to calculate the mass activity. This becomes more essential when the materials are loaded on three-dimensional conducting substrates for example Cu foam and Ni foam, the loadings become very large and its contribution to the resulting current densities unavoidable.[40] Mass activity of a catalyst is usually calculated using this equation:

Mass activity = A/g

where A is the current density at a particular overpotential and g is the corresponding loading of a catalyst. It is also concerned with normalized capacitive double layer current densities, assuming that only the exposed active surface area participates in the electrochemical interaction.

previous studies suggest that the activity of the electrodes increase with increasing the loading of the catalyst to a certain limit, then a subsequent decrease in the catalytic activity after certain loading. Which confirms that the loading of the catalyst has a direct effect on electrocatalytically active sites and subsequently the overall catalytic activity of the electrode.[44]

Mass normalized activity became one of the most important parameters used for quantitative analysis of the efficiency of the used catalyst, and it is usually calculated by dividing the recorded current by the mass of the loaded catalyst. Mass activity is considered more representative than current density, especially for catalysts with rough surface, as it is not very accurate to use the geometrical area in this case.[23] Instead, for rough surfaces it is more accurate to use real surface area normalized activity, also known as specific activity. As the real surface area represents the actual surface area of the catalyst (nanostructure) that acts as an active site and contribute to the reaction.

2.5.4 Turnover frequency (TOF)

TOF is another activity parameter that is used as an indicator for the reaction kinetics. It is defined as "The molecules of hydrogen or oxygen produced at a single catalytically active site per unit time".[44] TOF is calculated using equation (45).

$$\mathbf{TOF = j \times N_A / n \times F \times \Gamma} \qquad \mathbf{(45)}$$

where j is the current density (A cm^{-2}), N_A is the Avogadro number, n is the number of electrons needed to produce a molecule of the product (2 for H_2 and 4 for O_2), F is the Faraday constant, and Γ is the number of active sites on the surface that contribute to the reaction.

2.5.5 Faradaic efficiency (FE)

Faradaic efficiency helps in determining the selectivity of the catalyst towards one or both reactions (HER and OER), The two well-known methods used to calculate the faradaic efficiency compare the amount of gas evolved experimentally to the quantity expected from theoretical calculations. If the two values are close, this means that the faradaic efficiency is 100%, indicating

high selectivity towards this specific gas. Moreover, it shows that the energy supplied to the system is in producing the targeted species and that there are almost no side reactions, hence optimum energy utilization is achieved.

2.5.6 Stability and durability of the electrocatalyst in water electrolysis

The stability of the catalyst used is very crucial, especially for determining whether it is suitable for large scale application or not. An efficient electrocatalyst should be stable and robust to be suitable for long term utilization in electrocatalytic water splitting. Usually, three approaches are used to study stability of the catalyst, two them lie under potentiostatic analyses, these two techniques are chronoamperometry, in which the potential is fixed, and the current is observed as a function of time. The other technique that lies under potentiostatic analysis is chronopotentiometry, which involves fixing the current and monitoring the potential as a function of time. The third technique that can be used lies under potentiodynamic analysis. It is known as the accelerated degradation, where successive cyclic voltammetry (CV) cycles are applied. such as cyclic voltammetry at high scan rates (from 1000 to 5000 cycles).[23]

If the difference in the activities before and after the stability tests are negligible, this ensures that the catalyst is stable. In potentiodynamic conditions, the change in the overpotential at defined current densities is a measure of the robustness of the catalyst. Usually, the most challenging is the stability of the catalyst for OER in acidic conditions, as the anodic overpotential and the corrosive nature of both corrodes the electrode surface severely. The catalyst that sustains relatively a constant current or potential for more than 10 hours is considered stable and a promising candidate for large scale production. Remarkably, high stability is obtained when the materials are grown via hydrothermal and electrodeposition on 3D-substrates like Ni foam and Cu foam. This is attributed to the strong attachment of the catalyst material to the pores of the substrates. However, developing bi-functional catalysts is still that can be used as an alternative for noble metals and provides the same activity and stability features.

2.6 Theoretical background of electrode Fabrication

2.6.1 limitations of binder-based methodology

Various techniques are adopted to fabricate nanostructures of transition metal catalysts.[45-47] However, since the fabricated nanostructures are usually in the form of powder, there are some limitations regarding the preparation of an electrode that can be used to measure the activity of these nanostructures in the targeted application. For instance, using a polymeric binder to cast the catalyst on the selected substrate result in increasing the resistance, shielding the active sites, and limited mass transport, as illustrated in Figure 7.[48] This leads to using nanocarbon additives to increase the electrical conductivity,[49] However, these additives usually gets oxidized and suffers from etching under OER at high potentials, resulting in performance decline.[50] Moreover, due to the weak adhesive force between the catalyst and the substrate, the catalyst load is usually less than 1 $mgcm^{-2}$, limiting the number of the available active sites. Besides, at large current measurements and long-term stability tests, the catalyst layer might peel off from the substrate.[51] All these disadvantages taking place when the binder-based methodology is applied motivated the researchers to investigate new approaches that overcome these limitations that allow faster charge transfer and more accurate indication of the catalytic performance of the nanostructure under study.

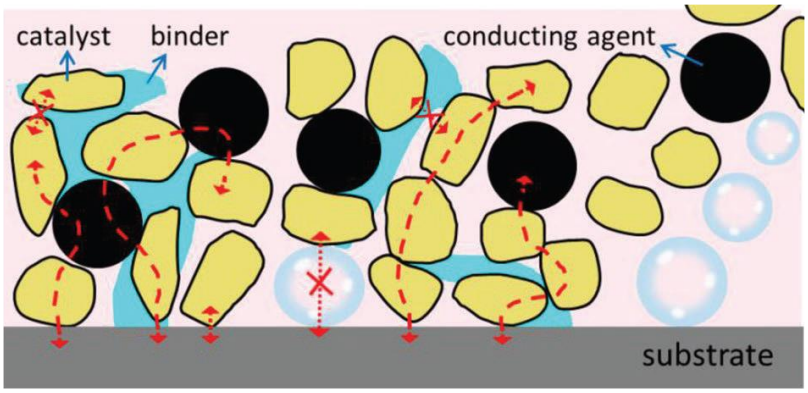

Figure 7 Schematic illustration of a powder catalyst deposited on the conducting substrate using polymer binder.[52]

2.6.2 Self supported electrodes

Self-supported electrodes are usually prepared via an in-situ nanostructure growth over

the selected conductive substrate, as illustrated in Figure 8, this method solves many of the problems encountered when using a binder. This technique enables a one-step method, where there is no need for a binder, carbon additives, and no post coating steps is required. Making the fabrication method easier and cheaper.[53] Besides, The direct connection between the catalyst layer and the substrate facilitates fast charge transfer, at the same time it ensures that the catalyst layer would not dissolve or peel off from the substrate.[53] Lastly, this method enables directing the morphology of the fabricated nanostructures along with the surface of the catalyst being more hydrophilic or hydrophobic, hydrophilic electrodes enable faster bubble detachment, thus keeping the active sites available for successive reactions and high rate of ion transfer.[54,55]

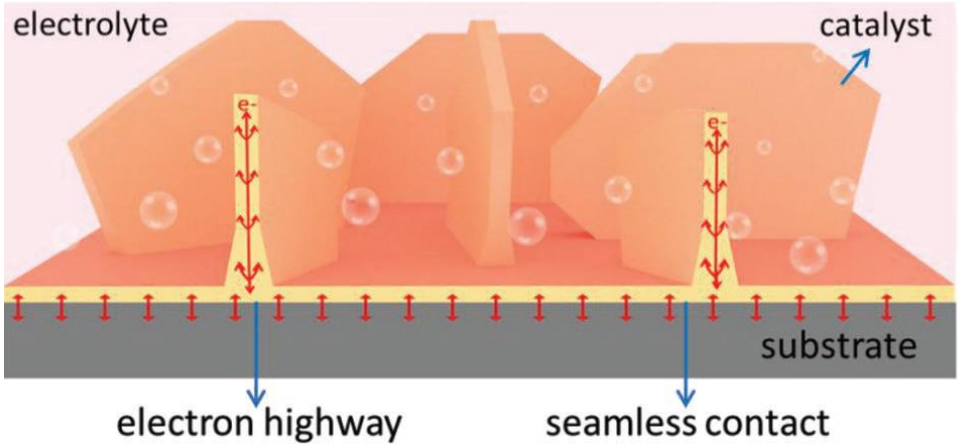

Figure 8 Schematic illustration of self-supported electrode prepared via an in situ growth on the conducting substrate.[52]

2.6.3 Different approaches used to prepare Self-Supported Electrode

As illustrated in Figure 9, Various routes can be used to in situ grow the targeted nanostructure over different substrates. Including vacuum filtration, freeze drying, vacuum filtration, electrodeposition, and hydro/solvothermal technique. The choice of any method depends on both the substrate and the targeted nanostructure. Regarding the material of the catalyst, transition metals are heavily used to synthesis self-supported electrodes employing this approach. Furthermore, different conductive substrates can be used, such as carbon cloth, carbon fiber, graphite plate, Ti and Cu mesh, Ni and Cu foam, metal foil (Ti/Pt/Cu foil).

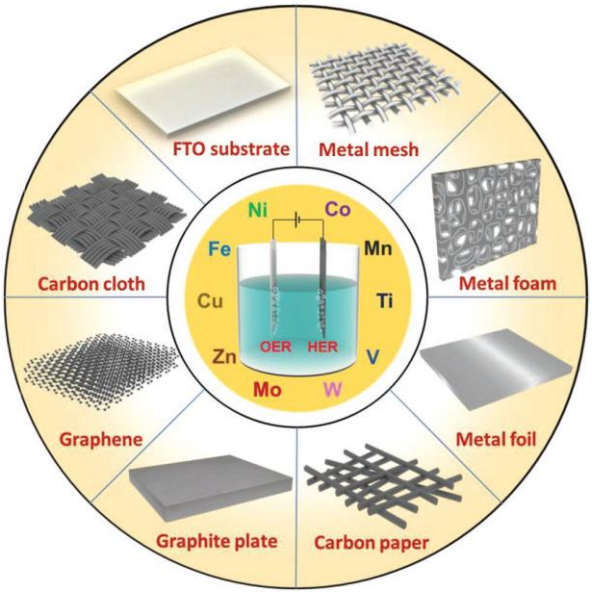

Figure 9 Different substrates and different transition metals used to fabricate self-supported electrodes.[52]

2.6.3.1 The hydro/solvothermal method

This methodology involves applying moderate temperature under high pressure. The defects and the oxyl groups on the surface of the substrate act as active sites for nucleation and crystal growth, as the growth continues, nanostructures are formed, As demonstrated in **Error! R eference source not found.**. Usually, this approach is used to fabricate metal oxides, hydroxides and oxyhydroxides.[56–58] These structure can then be treated into phosphides, carbides, selenides, sulfides.[56,57,59]

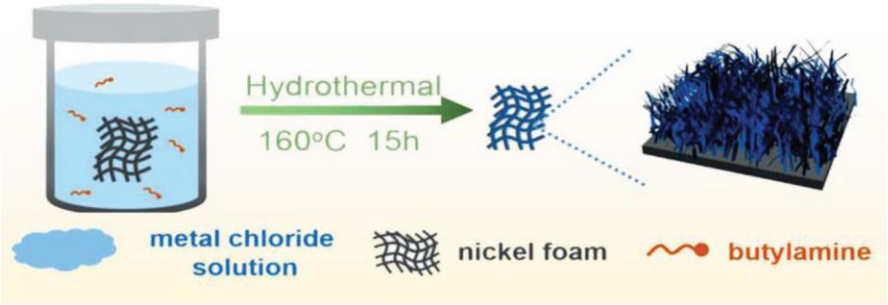

Figure 10 Schematic diagram of the hydrothermal technique used to grow oxyhydroxide on Ni foam, making a self-supported electrode.[56]

2.6.3.2 Electrodeposition technique

In this technique, a three-electrode electrochemical cell is used, which consists of a

working electrode, counter electrode, and a reference electrode. The working electrode is the conductive substrate on which the targeted nanostructures will be deposited under the effect of an applied potential.[60] The electrodeposition technique mainly depends on conversion of the electrical energy into chemical energy, where the rate of the nucleation and crystal growth of the formed nanostructure is directly correlated to the applied electric field, as expressed by the Kelvin equation (46).

$$\tau = \frac{2\delta V}{ze_0|\eta|} \qquad (46)$$

Where, τ is the nucleus radius, δ is the surface energy, V is the atomic volume, η is the overpotential.

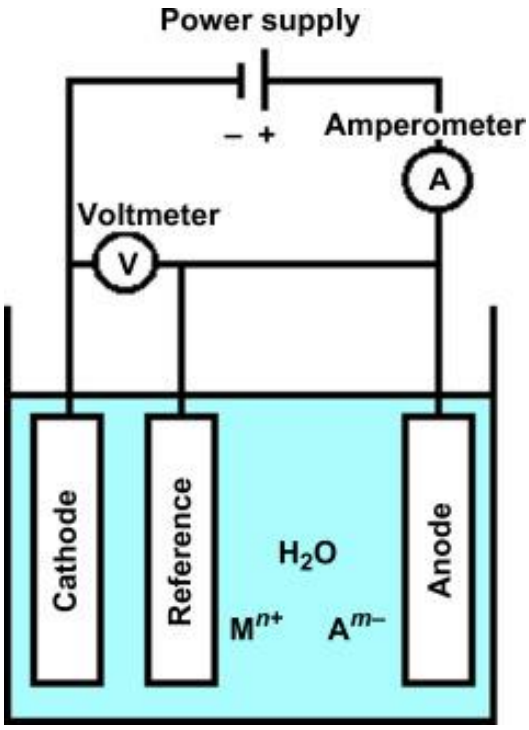

Figure 11 schematic representation of the setup used in electrodeposition technique.[61]

2.6.4 The electrospinning technique

The electrospinning technique is typically used to fabricate nanofibers of different materials using a polymeric material. As shown in Figure 12, a typical electrospinning setup

consists of three major parts: a power supply (high voltage source), a metallic capillary tip, and a collector as shown in Figure 12. The syringe contains a polymer solution, the solution is usually fed through the spinneret at a constant and adjustable rate using a syringe pump, and a high voltage usually 10 to 50 kV is applied between the collector and the syringe tip.[62,63] When the solution is subjected to high voltage, it becomes highly charged, thus, the solution droplet at the tip suffers from two opposite forces, surface tension and the electrostatic repulsion force. these electrostatic interactions result in the formation of a conical fluid at the tip of the syringe, this structure is called the Taylor Cone.[63–65] At a specific voltage, the electrostatic repulsion force formed on the charged polymer overcomes the surface tension of the solution, and a charged jet is ejected from the tip of the formed Taylor Cone, moving toward the counter electrode, and the solvent starts to evaporate. At the end solid fibers are collected on the counter electrode, with diameters ranging from nanometers to micrometers.[66]

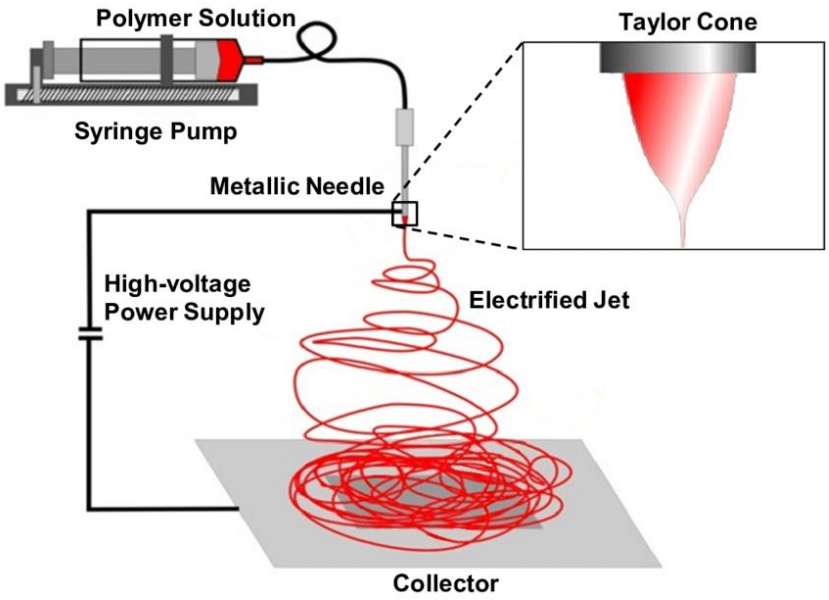

Figure 12 Schematic illustration of the electrospinning technique.[67]

Chapter 3

Literature review

3.1 The significance of choosing the material of the counter electrode

During the past few decades, hydrogen has been introduced as a promising alternative to traditional fossil fuels. In this regard, electrolysis is the commonly used process to produce hydrogen in large quantities. In this system, Pt is the most widely used electrocatalyst for the water reduction half reaction, due to its efficient electrical conductivity, high mechanical strength, and superior catalytic activity.[68] However, its use in large scale production has been greatly restricted due to its high cost and scarcity. Therefore, there is a growing need to develop earth-abundant electrocatalysts that possess comparable catalytic activity to that of Pt while being inexpensive.

For instance, previous studies introduced molybdenum carbide combined with rGO, revealing almost the same activity towards hydrogen evolution reaction (HER) of Pt/C.[69] Also, Ni−C-based catalysts showed comparable performance to that of Pt in HER.[70] Nevertheless, almost half of the published studies related to HER used Pt as the counter electrode with no ion-exchange membrane used.[71,72] Neglecting the fact that Pt is not stable and undergoes chemical/electrochemical dissolution during potential cycling,[71,73,74] the dissolved Pt ions redeposit on the surface of the working electrode, resulting in deceptive enhancement in the measured overpotential.[71,73,74] Furthermore, even when an ion exchange membrane (Nafion) is used, Pt dissolution and deposition on the working electrode still takes place.[75] These concerns necessitated the search for alternative counter electrodes. Consequently, carbon-based materials such as glassy carbon or graphite rod have been used instead. However, the question is still there; are those electrodes stable? and if not, is there a way out? The answer to these questions is explored and discussed in chapter 5.

3.2 Two dimensional materials - boron carbon nitride nanosheets

The increasing adverse effects of greenhouse gases and the shortage of fossil fuels have become a serious concern through the past few decades. These issues increased the need for alternative clean and sustainable energy resources.[76] One of the most promising solutions is the electrocatalytic water splitting, which depends on the use of electricity to generate hydrogen and oxygen gases. The resulting hydrogen gas can be used as a clean fuel for fuel cell applications.[15,77]

The most crucial point in this technology is finding an efficient catalyst that is earth abundant, low-cost, environmentally friendly, and easy to synthesize. Nanomaterials with low 0D, 1D, and 2D structures have recently attracted the attention of the scientific community due to their promising potentials in nanocatalysis.[78,79] Researchers have been trying to customize the catalytic activity of 2D materials by modifying their interfacial properties.[79]

Among those 2D materials, there is a growing interest in carbon-based materials due to their unique physical and chemical properties, including their exceptional electronic and mechanical properties, large surface area, and their reasonable price, making them competent with noble metal-based catalysts.[79] Moreover, noble metal catalysts have many drawbacks as they are not durable, highly susceptible to CO poisoning, low selectivity, and high cost.[80] Thus, there is a growing interest in fabricating 2D carbon-based materials that are economical, durable, stable, and possess high catalytic activity towards HER. To this end, boron-doped carbon nitride (BCN) nanosheets are one of the most booming materials as it comprises the unique physicochemical properties of both graphene and 2D hexagonal boron nitride, such as electrical conductivity, mechanical, and chemical stability. Besides, the heteropolar bonding between N and B can improve its electroactivity.[81–83]

Upon screening the literature, hexagonal boron nitride-based composites have shown promising results in many applications, including water splitting.[32,77,84,85], carbon dioxide reduction,[86] ammonia synthesis,[87] and microelectronic devices.[88] So far, BCN nanostructures showed very promising results in HER. However, the electrocatalytic performance of nonmetal 2D nanomaterials and BCN nanosheets still needs improvement as their electronic, chemical, and

physical properties are confined.[89] Besides, determining the number of catalytic sites and their intrinsic behavior are not fully understood, which limit the use of such materials in large scale electrocatalysis.[89] Consequently, modifying the interface of these 2D nanostructures with other low dimensional structures is expected to improve their activity in electrocatalytic systems. Moreover, if the two low dimensional materials are connected very closely, the interfacial interactions between them can create many high-speed electron pathways, thus accelerating charge transfer at the interface as well as adjusting the energy adsorption states needed for the intermediate catalytic species.[80,90]

3.2.1 Different fabrication techniques of BCN nanosheets.

Different synthesis techniques have been explored to fabricate hexagonal-boron carbon nitride (h-BCN) films, such as ion-beam sputtering deposition,[91] pulsed-laser deposition,[92,93] chemical vapor deposition (CVD), as shown in,[94–99] molecular beam epitaxy,[100] solid source diffusion or surface segregation,[99,101–104] and reactive magnetron sputtering.[105] Nevertheless, CVD is the most commonly used technique.[82] Different materials have been used to prepare BCN, such as dimethylamine borane,[106] trimethylamine borane,[107] bis-BN cyclohexane,[108] methylamine borane.[109] As illustrated in Figure 13 and Figure 14. However, agglomeration of h-BN and graphene-like domains was frequently detected, which should adversely affect the activity of the material.[110]

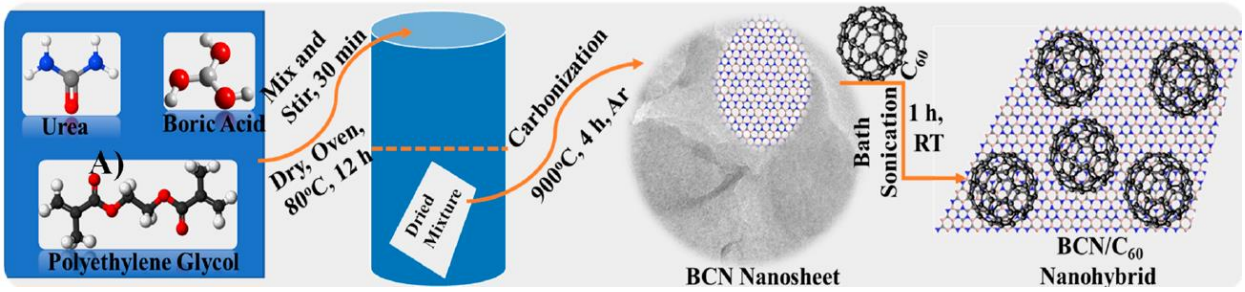

Figure 13 Schematic representation of the synthesis of Fullerene/BCN nanohybrids.[79]

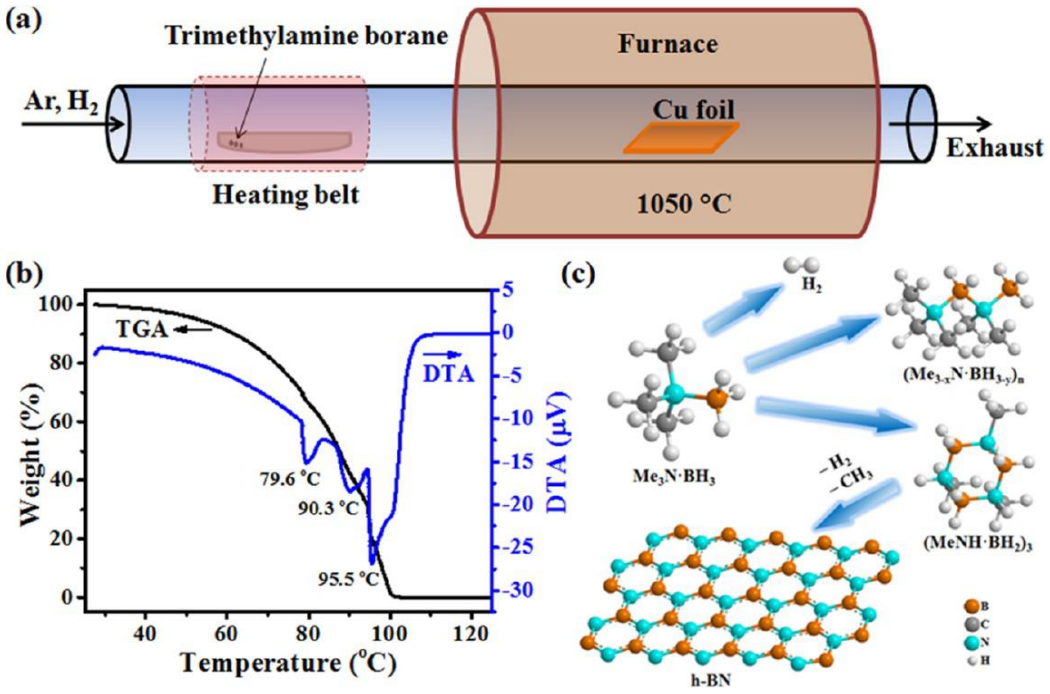

Figure 14 Schematic layout of the CVD setup for h-BN/h-BCN film growth.[82]

3.3 Importance of Cu in water electrolysis

Copper is an earth-abundant metal with many desirable electronic properties needed for the electrocatalytic water splitting. Cu possesses high electrical and thermal conductivity with strong resistance to arc erosion. Copper shows promising activity and stability in OER due to its susceptibility to intercalate with the hydroxyl group and oxygen cleavage. Thus, the different nanostructures and oxidation states (0, +1, and +2) of copper have been extensively investigated, which showed outstanding activities in both HER and OER under various pH conditions.[31] Furthermore, different copper compounds, such as hydroxides, oxides, phosphides, sulfides, and selenides, have been tested with good electrocatalytic activity.

Unfortunately, stability is always an issue. Therefore, there are many possibilities and modifications that should be investigated to further enhance the electrocatalytic activity and stability, such as in-situ growth on 3D metal foams, doping, and increasing the surface-active sites through structural modifications. These modifications are expected to get us closer to the ultimate goal, which is finding an alternative to the noble elements that provides the same activity and durability towards hydrogen production via electrocatalytic water splitting.[31]

In this regard, the catalytic activity of boron carbon nitride nanosheets with different loads of copper nanoparticles is examined and the results are demonstrated in chapter 6.

3.4 0D – Fullerene C_{76}

Low-dimensional nanomaterials have been explored as alternative to noble metals-based electrocatalysts,[111–113] As the interfacial interactions can be used to optimize the electronic structure and activity of those nanostructures.[114,115] Although nickel is a promising electrocatalyst compared to other transition metals, especially Ni foam due to its large surface area, the overpotential needed to drive the HER using Ni foam as an electrocatalyst is still relatively high compared to the benchmark catalysts.[24,116,117]

Moreover, interface engineering with low dimensional nanostructures seems to be very promising in introducing new electrocatalytic systems with comparable activity to the noble metals. This can be attributed to the possibility to promote high speed electron transfer channels at the interface, while tuning the energy of the adsorption states of the targeted species.[90,118]

Recently, the electrocatalytic activity of graphene/C_{60} hybrid was explored for HER, showing excellent activity due to the intrahybrid charge-transfer and the high affinity of C_{60} to accept electrons.[119] Also, the catalytic activity of C_{60}-adsorbed single-walled carbon nanotubes was explored with C_{60} acting as an electron acceptor, enabling the use of the material over a wide pH range for hydrogen evolution reaction (HER), oxygen evolution reaction (OER), and oxygen reduction reaction (ORR).[115] Moreover, C_{60} decorated with bimetallic Ni-Co phosphide was examined for HER, which showed relatively low overpotential of 97 mV at a current density of -10 mA/cm^2.[120] Furthermore, C_{60} and C_{70} functionalized with diazonium salts was found to provide ultra-active charge polarization centers on the fullerene cages, facilitating efficient HER.[121] Likewise, the interfacial interactions of van der Waals 1T-MoS_2/C_{60} demonstrated superb activity towards HER with low ΔG_H^* and small onset potential.[122]

Though, almost all reported studies were limited to C_{60} and its composites with very little work on higher fullerenes. Except for the study by Li and Wudl in 1992, which demonstrated that C_{76} is a better electron donor and acceptor than C_{60}[123], no study was performed to investigate the

potential use of C_{76} as a catalyst for water electrolysis. The potential of C_{76} as an electrocatalysts may originate from the fact that C_{76} is a 0D structure composed of hexagon and pentagon rings with high tendency to accept electrons.[90,124] In this regard, the activity of C_{76}/Nickel foam, and the effect of the facial interactions on the catalytic activity towards HER was studied as will be discussed in chapter 7.

3.5 Transition metals

Transition metals (TM) oxides[125]/hydroxides[126], sulfides[127], phosphides[128,129], carbides[130], and nitrides[130] proved their applicability to be used as electrocatalysts for water electrolysis. Moreover, among the transition metals, Co, Mn, Ni, and Fe showed high catalytic activity whether as a monometallic, bimetallic, trimetallic or tetra-metallic composite systems due to their high activity, long durability, and rich redox chemistry as they have multiple valent state possibility in their oxide forms.[131,132]

3.5.1 Co-based electrocatalysts

Co-based catalysts are widely used in water splitting due to their high activity. Co oxides/hydroxides with different morphologies were found to be an efficient OER catalyst such as mesoporous Co_3O_4,[133,134] urchin-like Co_3O_4,[135] Co_3O_4 nanosheets,[136] Co_3O_4 nanoparticle,[137] and Co_3O_4 nanowires.[134] Despite the high activity of Co based oxides and hydroxides towards OER, their weak conductivity restricts their use as an electrocatalyst.[138] To overcome this issue, two approaches are being investigated in the literature, the first one is using a substrate with higher conductivity, and the second approach involves forming a composite with another transition metal, thus tuning the band gap and enhance the conductivity.[138]

3.5.2 Mn-based electrocatalysts

Mn based catalysts are efficient for water oxidation in the photosynthesis process as can be seen in plant's leaves.[139,140] However, their catalytic activity toward OER is far below the outstanding activity of IrO_2, RuO_2 or Ni-Fe oxide anodes. Thus, Mn based catalysts needs further optimization to form an efficient electrocatalyst.[141–143]

3.5.3 Ni& Fe-based electrocatalysts

Ni & Fe are considered one of the most promising transition metals as a catalyst for both OER and HER. Liu et al. prepared NiO anchored on nitrogen doped reduced graphene oxide to be tested for OER & HER. The results showed higher activity towards OER that surpass Co based catalyst, and its activity was comparable to Pt in HER.[144] Louie et al. found that the incorporation of Fe into Ni oxide enhanced their electrocatalytic activity in water splitting reaction, as well as their high durability in alkaline media over a long period of time.[145,146]

Mixed transition metal oxides exhibited higher activity than their single counter parts as a result of their synergetic effect contributing to enhancing the activity of the system of mixed TM. Therefore, extensive studies were performed to study NiFe hydroxides,[147] layered double hydroxides,[148] alloys with other metals,[149,150] and nitrides.[151] Bates et al. reported the enhancement of the ternary Ni-Co-Fe towards OER due to the charge transfer from Co to Ni sites resulting in the oxidation of the Ni sites and activating Fe sites.[152] Another study by Vergas et al. reported the enhancement of electrochemical OER by ternary NiCoFe layered hydroxide.[153]

3.5.4 Transition metals phosphides

Lately, many studies on transition metal phosphides (TMPs) showed outstanding activity towards HER in wide range of pHs.[128,138] Among them, Fe, Ni, Co based phosphides have been extensively studied with different morphologies, and was found to be of high activity and high durability.[128,154–157] This is suggested to be due to the effect of the P atom orbitals in binding with hydrogen atom while weakening the bond between the metal and the hydrogen atom which has a direct effect on facilitating H_2 molecule desorption.[158] Another important concern is the effect of different substrates that are being used in electrocatalysis systems.

3.5.5 The crucial role of the substrate

The selected substrate plays an important role in the distribution of the loaded electrocatalyst to reduce the amount of the utilized catalyst. The substrate material should possess certain properties, such as good electrical conductivity, high surface area, stability in different pHs

and low cost.[159] In addition to that, it should possess sufficient catalyst-support interaction to improve the dispersion of the catalyst and facilitates the transfer of the generated charges.[160] Carbon-based materials and Ni foam are widely used as substrates in water electrolysis.

Recently, many studies started to emphasis the electrocatalytic activity of Ni foam towards OER and HER. Ni foam was found to tend to form a passive oxide layer on the surface once immersed in the electrolyte, this oxide layer might lead to interference with the recorded electrochemical activity of the catalyst under study.[161] On the other hand, Ti mesh as a low cost material ($.23/inch) was been proven to be a suitable substrate due to its large surface area, high stability in different pHs, as well as having higher corrosion resistance.[162] More importantly, it shows very low activity towards water electrolysis, Thus making its contribution to the recorded electroactivity negligible.[25]

Accordingly, as will be discussed in chapter 8, different combinations of Ni, Co, Mn, and Fe nanosheets were deposited on Ti mesh and tested as and electrocatalyst for HER and OER. Besides, the composite with the highest catalytic activity was subjected to electro-phosphidation to further reduce the overpotential needed to drive the reaction.

Chapter 4

Methodology and Experimental work

4.1 Experimental work of studying the different counter electrodes

For the working electrode, a very thin layer of boron carbon nitride-copper composite was deposited over graphite sheet. $Hg/HgSO_4$ was used as the reference electrode and. Pt foil, gold coil, glassy carbon rod and titanium mesh were used as the counter electrode (CE). All the voltage values were converted into the reversible hydrogen electrode (RHE), where $E_{RHE} = E_{Hg/HgSO4} + 0.64\ V + 0.059\ pH$.

4.2 Characterization of the different counter electrodes

The morphology of the fabricated nanofibers was characterized with Zeiss SEM Ultra 60 field emission scanning electron microscope (FESEM). Energy Dispersive X-ray (EDX; Oxford ISIS 310, England) spectroscopy attached to the FESEM microscope was used for the elemental analysis and mapping of the fabricated electrodes, and the crystal structure using X-ray photoelectron spectroscopy (XPS, Thermo-Scientific) measurements were conducted in UHV chamber equipped with hemispherical energy analyzer (SPHERA U7) with Al Kα monochromator X-ray source (1486.6 eV), operated at Constant Analyzer Energy (CAE 50) mode.

4.3 Novel methodology for BCN-Cu nanosheets Fabrication

In this dissertation, I am introducing a new technique that have not been used for this application before, which is electrospinning, which was explained in detail in chapter 3.

Chemicals and materials:

Boron oxide (B_2O_3), polyvinylpyrrolidone (PVP, Mw = 1 300 000), hexamethylenetetramine [$(CH_2)_6\ N_4$], copper (II) acetate monohydrate ($C4\text{-}H_6CuO_4.H_2O$), and

ethanol absolute. All chemicals were purchased from Alfa Aesar. All chemicals were used directly without further purification.

4.4 The self-supported electrospun electrode

The electrospinning technique was used to fabricate BCN nanofibers and BCN–Cu composite nanofibers. For BCN nanofibers, two solutions were prepared. The first solution was prepared by dissolving 0.1 g of B_2O_3 in 20 ml of ethanol, then 2 g of PVP were added to the solution with continuous stirring. In the second solution, 0.2 g of $[(CH_2)_6N_4]$ were dissolved in 6 ml of ethanol, then 0.8 g of PVP was added to the solution with continuous stirring. Finally, the two solutions were mixed and stirred for hours before electrospinning.

For the BCN-Cu composite nanofibers, different loadings of copper acetate monohydrate (0.075, 0.1, 0.125, and 0.15) g were dissolved in 4.5 ml of absolute ethanol with stirring and heating at 40 ^{0}C until the polymer is completely dissolved, then 0.6 g of PVP was added to the solution with continuous stirring. Then, this mixture was added to the solution of BCN and stirred for 4 hours until homogeneous solution is obtained. In the rest of this study these composites are named 0.075 Cu-BCN, 0.1 Cu-BCN, 0.125 Cu-BCN, and 0.15 Cu-BCN. Finally, each of the two solutions was passed through a 16 G stainless steel nozzle. Appling a voltage of 21 kV, the distance between the grounded aluminum foil collector and the syringe tip was fixed at 15 cm, and the feed rate was 2 ml/h, at humidity of 28% to 42%.

4.5 The binder-based electrode

For the binder-based working electrodes, the collected nanofibers were annealed at 600 ºC in argon atmosphere in a Lindberg/Blue M tube furnace. The resulting powder was grinded and an ink was prepared by mixing 90 wt% of the fabricated composite with 10 wt% polyvinylidene fluoride (PVDF), and dimethylfromamide (DMF) as a solvent. The mixture was stirred until a homogeneous suspension was formed. The prepared ink was then sprayed using a manually operated powder coating spray gun onto graphite sheet, which was fixed on heating plate adjusted at 50 °C to evaporate the solvent. For the binder-free working electrodes, the electrospun nanofibers were collected directly on the graphite sheet after spreading a thin layer of the

polymeric solution on the surface of the graphite sheet, then annealed in a Lindberg/Blue M tube furnace in argon atmosphere at 600 ^{0}C (2 ^{0}C/min) for 6 hours.

4.6 BCN-Cu Electrochemical measurements

The electrochemical measurements were done in 0.5 M H_2SO_4 as an electrolyte, using a three-electrode system. For the working electrode, a graphite sheet was used as the substrate for the fabricated composites, while titanium mesh roll, and $Hg/HgSO_4$ were used as the counter and reference electrodes, respectively. All voltages were converted into the reversible hydrogen electrode (RHE) using Equation (47) (pH=0.3).[163]

$$\mathbf{E_{RHE} = E_{Hg/HgSO4} + 0.64\ V + 0.059pH} \qquad \mathbf{(47)}$$

The surface activation/cleaning was realized by applying 700 cycles in the potential range (0.06 V to − 0.2 V vs RHE) at a scan rate of 5 mVs^{-1} in 0.5 M H_2SO_4, after which the overpotential was measured. Chronopotentiometry (CP) measurements were performed at a current density of -100 mA/cm^2 for 10 h.

4.7 Characterization of BCN-Cu nanosheets

Zeiss SEM Ultra 60 field emission scanning electron microscope (FESEM) was used to study the morphology of the fabricated nanofibers. X-ray photoelectron spectroscopy (XPS, Thermo-Scientific) measurements were conducted in UHV chamber equipped with hemispherical energy analyzer (SPHERA U7) with Al Kα monochromator X-ray source (1486.6 eV), operated at Constant Analyzer Energy (CAE 50) mode, and was further confirmed using Raman microscope (Pro Raman-L Analyzer) with an excitation laser beam wavelength of 532 nm. Fourier transform infrared spectroscopy (FTIR, Perkin Elmer spectrometer using KBr pellets) measurements were shown to distinguish the surface functional groups of the fabricated composites. Energy Dispersive X-ray (EDX; Oxford ISIS 310, England) spectroscopy attached to the FESEM microscope was used for the elemental analysis and mapping of the fabricated electrodes.

4.8 BCN-Cu DFT Calculations

Density functional theory (DFT) calculations were performed with CASTEP code with spin polarization to perform the calculations of energies, geometry optimizations, and electronic structure. The Perdew–Burke–Ernzehof (PBE) within the general gradient approximation (GGA) was utilized to describe the electronic exchange-correlation energies. The ions-electrons interactions were described by the Ultrasoft pseudopotential. The performed minimization algorithm was the Broyden-Fletcher-Goldfarb-Shanno (BFGS) scheme. The used cut-off energy for all calculations was 440 eV. Regarding the Monkhorst–Pack mesh, the k- points were sampled with a separation of 0.04. The boron carbon nitride sheet was used as support for the copper cluster with a supercell of 3 Å × 4 Å. To test the accuracy of the calculations, the same parameters of calculations were first optimized and used to simulate the graphene sheet and the calculated bond length was 1.423 Å in good agreement with the previous theoretical and experimental results. Also, Hubbard correction (U) was applied to overcome the GGA underestimation of the band gap, Ud = 8 for Cu metal, and Up = 6 for oxygen atom. These values were selected as they showed results that are very close to the experimental data.

The model of BCN sheet composed of 45 carbon atoms, 1 boron atom, 2 nitrogen atoms, while the model of the copper oxide cluster includes 4 copper atoms and 5 oxygen atoms, which is relatively close to our experimental data and maintaining the computational cost. The copper oxide cluster was designed in square lattice, which is the most stable form[164], while the pure copper metal is not stable in this form and prefers the pyramidal form. The BCN sheet was separated by a 20 Å vacuum slab to eliminate the interactions between the two periodic units. Atoms' relaxations were meeting the convergence criteria of 5 × 10−6 eV for the energy, 0.02 GPa for the stress, 0.01 eV/Å for the force, and 5 × 10−4 Å for the displacement, see Figure 15.

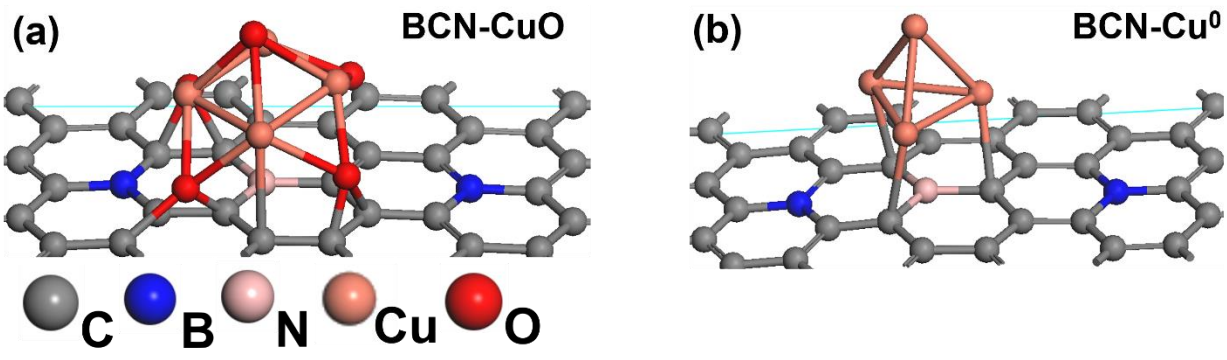

Figure 15 (a,b) Optimized geometries of BCN-CuO and BCN-Cu nanosheets, respectively.

4.7 C_{76}/Ni foam electrode fabrication

Materials. The tested fullerene (C_{76}) was purchased from Sigma-Aldrich and used as received. The electrolytes were prepared from high purity H_2SO_4 (Alfa Aesar). To prepare the catalyst ink used for the working electrode, 5 mg of C_{76} and 0.05 mL of Nafion solution were dispersed in a mixture of 0.23 mL of isopropanol and 0.23 ml of water. The slurry was then stirred for 24 hours to prepare a homogeneous ink. Afterward, different loads of the catalyst ink were deposited on the working electrode and dried in oven at 60 ^oC for 24 h to remove the solvents and to enhance the adhesion between C_{76} and the substrate. First, graphite sheet was used as a substrate to investigate the catalytic activity of C_{76} alone, then C_{76} was deposited on 0.25 cm^2 Ni foam and tested for HER.

4.8 Structural Characterization of C_{76}/Ni foam

The structure of C_{76} was characterized via Fourier transform infrared spectroscopy (FT-IR) using Perkin Elmer Spectrometer. Raman spectra were recorded using a dispersive micro-Raman spectrometer (Sentra-Bruker) with an excitation wavelength of 532 nm. The hybridization in C_{76} structure was studied using x-ray photoelectron spectrometer (XPS ESCALAB 250XI, Thermo Scientific). The nitrogen adsorption/desorption isotherms were used to elucidate the porosity and the surface area of the C_{76} at 77°C. The data were analyzed using the BET method and the NLDFT (Cylindrical pore) model using NOVATouch LX2 instrument and software.

4.9 C_{76}/Ni foam Electrochemical Measurements

The electrochemical measurements were conducted using a three-electrode system on a BioLogic SP-300 workstation, with $Hg/HgSO_4$ and Ti mesh roll as the reference and counter electrodes, respectively, in 0.5 M H_2SO_4 aqueous electrolyte. Linear sweep voltammetry (LSV) measurements were performed at a scan rate of 5 mV s^{-1} in an electrolyte solution. The exchange current density (J_0), the charge transfer coefficient (α), and the mass activity (MA) were calculated to investigate the kinetics of the reaction. All the recorded measurements were converted to the reversible hydrogen electrode (RHE) using the equation $E_{RHE} = E_{Hg/HgSO4} + 0.64\ V + 0.0598pH$, (pH=0.3).[163] $J_0$and α were calculated by plotting the overpotential vs ln |J|, where the intercept gives ln J_0. From Tafel equation, $\alpha = RT/(slope \times nF)$.[112]

4.10 C_{76}/Ni foam DFT Calculations

Gaussian 16 software with B3LYP method and the 6–31G (d,p) basis set was used to investigate the electronic structure of different fullerenes.[165] The bandgap energies of the investigated fullerenes (C_{60}, C_{70}, C_{76}, $C_{84,}$ and C_{100}) were calculated by subtracting the highest occupied molecular orbital (HOMO) and the lowest unoccupied molecular orbital (LUMO). Nanotube modeler, GaussView 6, and GaussSum software were used to visualize and analyze the data. The CASTEP code as implemented in Material studio 2017 software was used to investigate the C_{76}/Ni interface.

First, Ni foam was simulated as a cubic Ni of space group Fm3m. A 5 ×5×5 supercell was created, forming six-layers thickness, with the Ni (111) surface. Then, C_{76} was added on the top of the nickel first layer. To avoid the interaction between images, a vacuum slab of 30Å was set. To study the electron–electron interaction, the exchange-correlation functional with the generalized gradient approximation (GGA) was applied with pseudopotentials ultrasoft and Perdew–Burke–Ernzerhof functional (PBE). After convergence, a cutoff energy of 330 eV, a force tolerance of 0.01 eV $Å^{-1}$, an energy tolerance of 5.0×10^{-7} eV per atom, a maximum displacement of 5.0×10^{-4} Å, and a k point sampling of 2 × 2 × 1 were used. The upper three nickel layers and fullerene were relaxed during optimization while the bottom layers were fixed.

4.11 Fabrication of NiCoMnFe-P nanosheets

Electrodeposition of the Catalysts. Different combinations of the four metals (Ni, Co, Mn, and Fe) were electrodeposited on commercial titanium mesh substrates. Different electrolytes were prepared by dissolving fixed molarities of the salts containing the desired ions with Ni:Co:Mn:Fe ratio of 1:1:1:0.5.

Thus, 5 mM of $Ni(NO_3)_2 \cdot 6H_2O$, 5 mM of $MnCl_2.4H_2O$, 5 mM of $Co(NO_3)_2.6H_2O$, and 2.5 mM of $FeCl_3$ were dissolved in 30 ml distilled water and 10 mM KCl was added as a supporting electrolyte, then this solution was stirred for 2 hours.

For the phosphide-based composites, to prepare NiCoMnFe-P1 and NiCoMnFe-P2, the same solution above was prepared, then 0.3 M sodium trypolyphosphate ($Na_5P_3O_{10}$) and sodium phosphate dibasic dihydrate ($Na_2HPO_4 \cdot 2H_2O$) were added to the solution and stirred for 2 hours. These solutions were then used as electrolytes during the electrodeposition process. The electrodeposition was performed using a three-electrode system, where Ti mesh, Pt foil, and saturated calomel electrode were used as working, counter, and reference electrode, respectively. Three sweeps of cyclic voltammetry were conducted from 0.2 to -1.2 V vs. SCE at a scan rate of 5 mV s^{-1} and applying 85% IR correction. For the P-based composites, after applying these three CV cycles, an additional step was done using galvanostatic electrodeposition accompanied with hydrogen evolution, where a constant current of -200 mA was applied for 10 min to form the phosphide structure.

4.12 Characterization of NiCoMnFe-P nanosheets

The morphology of the fabricated nanosheets was studied using Zeiss SEM Ultra 60 field emission scanning electron microscope (FESEM). The structure of the formed composites was investigated using PANalytical X'pert Pro PW3040 MPD X-ray Diffractometer (XRD) using copper Cu Kα radiation (λ= 0.15406 nm) in the range of 5^o to 80^o at a scan rate (2θ) of 3^o s^{-1}. To explore the electronic structure and the chemical environment, x-ray photoelectron spectroscopy (XPS, Thermo-Scientific) measurements were conducted in UHV chamber equipped with hemispherical energy analyzer (SPHERA U7) with Al Kα monochromator x-ray source (1486.6 eV), operated at Constant Analyzer Energy (CAE 50) mode.

4.13 Electrochemical measurements of NiCoMnFe-P nanosheets

All electrochemical measurements were performed in 1 M KOH as the electrolyte for HER and OER measurements in a three-electrode system, where titanium mesh roll was used as a counter electrode. For the working electrode, the composites under study were deposited on an area of 1 cm^2. Hg/HgO was used as a reference electrode. For the overall waster splitting device measurements, the same setup was used except that the reference electrode was removed. All the electrochemical measurements were performed after applying IR correction of 85%. Linear sweep voltammetry test was performed at a scan rate of 5 mV/sec. The turnover frequency (TOF) was calculated using Eq. 1 assuming that all active centers are included in the reaction.

$$\mathbf{TOF} = \frac{\mathbf{j}*\mathbf{N_A}}{\mathbf{n}*\mathbf{F}*\Gamma} \quad (48)$$

where j is the measured current density (mA/cm^2), N_A is Avogadro's number, n is the number of electrons transferred during the reaction (2 for HER and 4 for OER), F is the Faraday's constant, and Γ is the number of the active surface sites obtained by integrating the area below the redox peak of each composition. Tafel slope values were obtained by plotting log j vs. the overpotential from the corresponding LSV curves.

4.14 Computational Details

CASTEP code was used as implemented in Material Studio software version 2017. For the MnFeCoNi-P catalyst, we started with Ni_2P unit cell, where a supercell of 3×4×1 was created. Geometry optimization was carried out for the bulk system, then (111) surface was cleaved. For the MnFeCoNi catalyst, we began with MnFe unit cell. A supercell of 2×7×1 was created to keep the ratio between elements (Mn:Fe:Co:Ni) 1:0.5:1:1, respectively. All calculations were done with generalized gradient approximation (GGA) of Perdew-Burke and Ernzerhof (PPE), cutoff energy was set to 990 eV. We used norm conserving pseudopotential to depict the ionic cores. k-point was generated with a 2×2×1 grid with a convergence tolerance of 5×10^{-6}, max force was 0.01, BFGS algorithm was chosen, density mixing as electronic minimizer, SCF tolerance was set to 5×10^{-7} eV/atom. All used parameters were chosen based on the convergence test results. The zero-point energy and entropy were calculated by phonon calculations.

The oxygen evolution reaction consists of four one-electron steps. The activity of each step expressed by Gibbs free energy as explained in the following equations:

$$\mathbf{H_2O(l)} + * \rightarrow \mathbf{HO^*} + \mathbf{H^+} + \mathbf{e^-}$$

$$\triangle \mathbf{G_1} = \mathbf{E_{HO}} - \mathbf{E_{slab}} + \mathbf{^1/_2}\,\mathbf{H_2} - \mathbf{H_2O} + \triangle \mathbf{E_{ZPE}} - \mathbf{T} \triangle \mathbf{S}$$

$$\mathbf{HO^*} \rightarrow \mathbf{O^*} + \mathbf{H^+} + \mathbf{e^-}$$

$$\triangle \mathbf{G_2} = \mathbf{E_O} - \mathbf{E_{HO}} + \mathbf{^1/_2}\,\mathbf{E_{H2}} + \triangle \mathbf{E_{ZPE}} - \mathbf{T} \triangle \mathbf{S}$$

$$\mathbf{O^*} + \mathbf{H_2O(l)} \rightarrow \mathbf{HOO^*} + \mathbf{H^+} + \mathbf{e^-}$$

$$\triangle \mathbf{G_3} = \mathbf{E_{HOO}} - \mathbf{E_O} + \mathbf{^1/_2}\,\mathbf{E_{H2}} - \mathbf{E_{H2O}} + \triangle \mathbf{E_{ZPE}} - \mathbf{T} \triangle \mathbf{S}$$

$$\mathbf{HOO^*} \rightarrow \mathbf{O_2(g)} + \mathbf{H^+} + \mathbf{e^-}$$

$$\triangle \mathbf{G_4} = \mathbf{E_{slab}} - \mathbf{E_{HOO}} - \mathbf{^3/_2}\,\mathbf{H_2} + \mathbf{2H_2O} + \mathbf{4.92} + \triangle \mathbf{E_{ZPE}} - \mathbf{T} \triangle \mathbf{S}$$

Where E_{H2}, E_{HO}, E_{slab}, E_{HO}, E_H and E_{HOO} are energies of free H_2, free H_2O, clean surface, adsorbed HO, adsorbed H, adsorbed HOO on surface respectively.

Table 1 Calculated Gibbs free energy for MnFeCoNiP and MnFeCoNi during OER.

Catalyst	ΔG_1	ΔG_2	ΔG_3	ΔG_4
MnFeCoNi	1.37	0.61	2.3	0.73
MnFeCoNiP	1.62	-0.57	3.27	2.43

Chapter 5 Results and discussion

Deceptive enhancement of HER overpotential induced by counter electrode dissolution: Is there a way out?

5.1 Effect of the activation range on CE dissolution

In chapter 3 we demonstrated the significance of choosing a convenient counter electrode, Accordingly, in this chapter I investigated the stability of the most commonly used counter electrodes (Pt, Au, and glassy carbon) during the HER in acidic media. The effect of the relative area of the working electrode to the counter electrode and the potential range used in the activation/cleaning of the surface on the rate of the counter electrode dissolution and its correlation to the recorded overpotentials is fully addressed and discussed. Finally, I demonstrate the potential of commercial titanium mesh as a stable and functional counter electrode for HER in acidic media.

In most of the recently reported studies related to HER, activation or surface cleaning is the first step performed in electrochemical measurements. It is widely accepted that as the current increases, the potential on the counter electrode increases [71]. This encouraged us to investigate the effect of different potential windows during the activation step and its correlation to the counter electrode dissolution rate. Thus, we explored two ranges for the CV cycles; narrow activation range (0.06 V to -0.2 vs RHE) and wide activation range (0.06 V to -0.34 V vs RHE).

Upon expanding the potential window towards more negative potentials, the current starts to increase as the number of cycles increases, Figure 16a,b. This is expected to increase the rate of Pt dissolution. The dissolved Pt would redeposit on the surface of the working electrode, resulting in a deceptive enhancement in the recorded catalytic activity of the working electrode. Figure 16c shows the shift in the linear sweep voltammograms (LSV) recorded before and after

the electrochemical activation at -10 mA/cm^2. When a narrow CV range scan is applied in the non-Faradaic region a shift of 170 mV was recorded after 300 CV cycles, while a shift of 400 mV after 300 CV cycles was observed when 300 cycles of the wide activation range was applied.

The EDX analysis of both samples after electrochemical measurements (inset in Figure 16c) showed much higher intensity of the Pt peak of the sample tested in the wide activation range than that tested in the narrow range. Furthermore, the SEM images of the sample before electrochemical activation (Figure 16d), and after applying narrow (Figure 16e), wide range (Figure 16f) activation were investigated. Note the presence of a few number of small Pt nanoparticles upon applying narrow activation range. However, upon activation over a wide range, the surface was heavily covered with Pt nanoparticles. The corresponding EDX mapping of the surface of the working electrode after applying NRA and WRA are shown in Figure 16g and h respectively. This signifies the importance of choosing the activation range that does not involve any current increase to avoid the dissolution of the CE. Note that electrode polarization usually takes place upon attaining high current or if the electron transport rate is higher than the reaction rate [71].

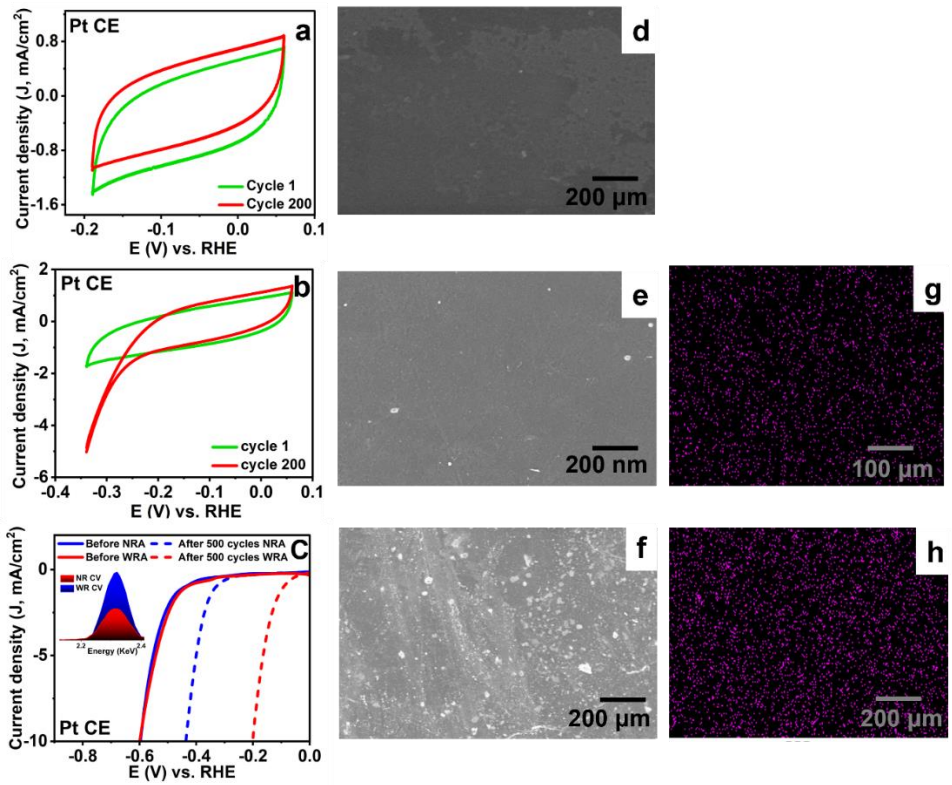

Figure 16. (a,b) CV scans using Pt foil as the CE upon varying the potential range, (c) LSV scans before and after applying the different potential ranges, the inset in (c) depicts the difference in the Pt EDX signal intensity after applying the different potential ranges. FESEM images of the sample (d) before and after applying (e) narrow and (f) wide activation range.

5.2 Effect of the area of the working electrode on CE dissolution rate

Counter electrodes in electrochemical cells are used to keep the rate of the half-reaction taking place on their surfaces faster than the other half-reaction on the WE. Consequently, if the CE's half-reaction is slower than the complementary one on the WE, the recorded current would be misleading as the CE dictates the current response. To overcome such problem, the CE should possess high electrical conductivity and larger surface area (typically ten times) than the WE to ensure fast reaction kinetics on the CE.[166]

To elucidate such an impact, the area of the Pt CE was kept constant while varying the area of the WE (0.25 cm^2 and 1 cm^2). As the area of the WE increases, the overpotential drastically reduced (Figure 17a), which can be ascribed to the higher rate of Pt dissolution and redeposition on the working electrode. This was further confirmed by the EDX analysis, inset in Figure 17a, where the intensity of the Pt peak significantly increases as the area increases. Additionally, SEM images further confirm the correlation between the area of the working electrode and the dissolution rate of the CE, Figure 17b,c. When the area of the WE was 0.25 cm^2, small Pt nanoparticles start to appear on the surface of the WE. On the other hand, when the area of the WE was 1 cm^2, highly dense Pt particles were observed on the WE surface, starting to form Pt clusters. The corresponding EDX mapping of the surface of the working electrode after electrochemical measurements when the area of the working electrode is 0.25 cm^2 and 1 cm^2 are shown in Figure 17d and e respectively.

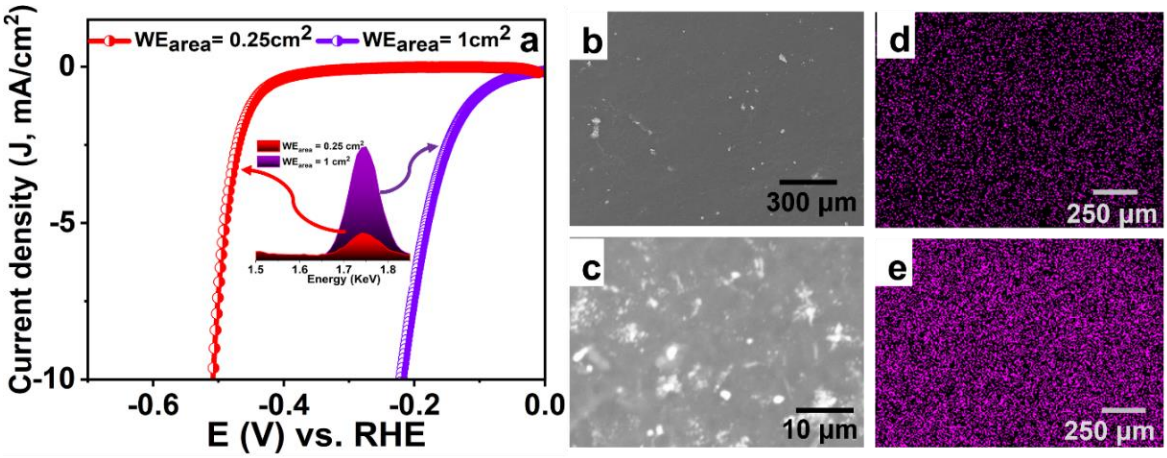

Figure 17. (a) LSV curves using Pt foil as the CE while varying the area of the WE, the inset in (a) shows the difference in EDX signal intensity of Pt deposited on of the two WEs after applying the electrochemical measurements, and (b,c) FESEM images of the WEs with the area of 0.25 cm^2 and 1 cm^2 after applying the electrochemical measurements, respectively.

5.3 Is there a way out?

The above findings showed the dissolution of Pt upon its use as a CE for HER in acidic media. Therefore, more materials have been tested to elucidate their stability with the hope to identify a stable material for use as CE. Particularly, Pt foil, gold coil, glassy carbon rod, and titanium mesh roll were tested as the counter electrodes in HER 3-electrode system. LSV experiments were performed while fixing the area of the working electrode at 0.25 cm^2. The overpotentials were measured for the different counter electrodes before and after applying 700 activation cycles in the narrow activation range (0.06 V to -0.2 V vs RHE) at a scan rate of 5 mVs^{-1} in 0.5 M H_2SO_4.

Figure 18a shows the LSV recordings of the four counter electrodes before activation, and as expected the overpotential is almost the same for the four counter electrodes. Figure 18b shows the LSV recordings of the four counter electrodes after activation, note that there is a substantial shift in the recorded overpotential. The recorded overpotentials are in ascending order as gold coil, Pt foil, titanium mesh, and glassy carbon rod, with the values of -0.35 V, -0.5, -0.69, and -0.84 V, respectively. While the lowest overpotential was recorded upon the use of gold coil as the CE, the use of glassy carbon electrode resulted in the highest overpotential.

Tafel slopes were calculated to investigate the kinetics, as shown in Figure 18b. When gold coil was used as the CE, the lowest Tafel slope was obtained (39.8), while the Tafel slope of the Pt, Ti mesh, and glassy carbon rod CE were 65.9, 121.1, and 258.4, respectively. The enhancement in the overpotential and the Tafel slope values when gold coil and Pt foil were used as the CEs indicates that this is probably due to the dissolution and redeposition of gold and platinum on the working electrode. We expect the enhancement in the reaction kinetics is due to the deposition of gold and Pt species on the surface of the working electrode, resulting in reduced overpotential, in accordance with the LSV measurements discussed before. Besides, that the shift observed after activation suggests that electrochemical dissolution mainly happens during the activation cycles. The EDX analysis (Figure 18d) revealed the presence of gold and platinum on the working electrode, while no Ti was detected.

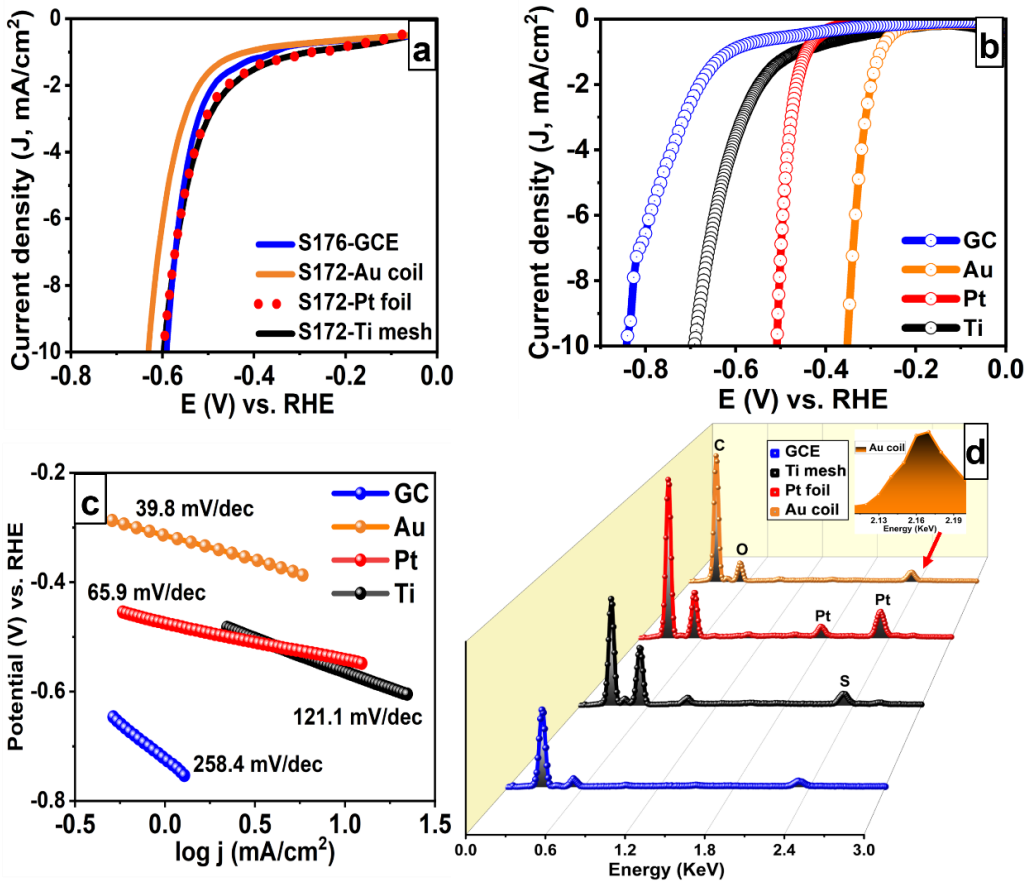

Figure 18. (a,b) LSV and their corresponding Tafel slopes, and (c) EDX of the working electrodes after electrochemical measurements using Pt foil, gold coil, glassy carbon rod, and Ti mesh roll as the counter electrodes.

5.4 XPS analysis

XPS analysis further confirmed the deposition of Pt and Au nanoparticles on the surface of the counter electrodes, as illustrated in Figure 19, upon the use of Pt foil and Au coil as the counter electrodes. The spin-orbit coupling of Au $4f_{7/2}$ and Au $4f_{5/2}$ is 84 eV and 87.5 eV, indicating the presence of elemental Au^0 on the surface of the working electrode.[167,168] Also, Pt $4f_{7/2}$ and Pt $4f_{5/2}$ peaks were observed at 71.6 eV and 74.9 eV respectively.[71,169] On the other, upon using Ti mesh as the CE, no signal related to Ti was found. This indicates that both gold coil and platinum foil are not stable. On the other hand, although Ti mesh and glassy carbon rod are stable, a large shift in the overpotential is evident, which is probably due to the small surface area of the glassy carbon rod relative to the large surface area of the Ti mesh roll. Yi et al. demonstrated that glassy carbon in acidic media undergoes degradation because the acid catalyzes the formation of surface oxides followed by ring opening in the graphitic structure, and finally oxidation in the bulk. Thus, glassy carbon rod does not seem to be efficient in elucidating the catalytic activity of the working electrode and it might result in misleading overpotential.[170]

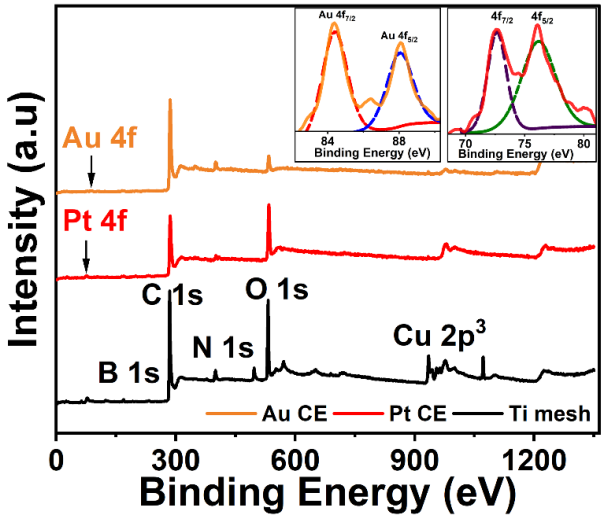

Figure 19. XPS survey of the working electrode after electrochemical measurements using Pt foil, Au coil and Ti mesh as the counter electrode, the inset is for Pt and Au 4f spectrum.

5.5 Conclusion

In conclusion, the effect of the catalytic area of the working electrode relative to the area of counter electrode on the performance of the catalyst for HER in acidic media was demonstrated. Choosing the convenient potential range in the activation/cleaning of the surface is very crucial as it might accelerate the dissolution rate of the counter electrode. To this end, the dissolution behavior of four different counter electrodes was investigated during the electrochemical measurement of HER activity in acidic medium. Gold coil, Pt foil, and glassy carbon counter electrodes were found to be susceptible to dissolution in acidic medium. The dissolved ions were found to be redeposited on the surface of the working electrode, resulting in fictitious enhancement in the recorded overpotential and the electrochemical activity of the working electrode. On the good side, the Ti mesh, when used as the counter electrode, showed exceptional stability was Ti detected on the working electrode surface as confirmed via EDX and SEM analysis.

Chapter 6 Results and discussion

Intermolecular Electron Transfer in Electrochemically Exfoliated BCN-Cu Nanosheet Electrocatalysts for Efficient Hydrogen Evolution

6.1 Morphology

Figure 20a shows typical FESEM images of the as-electrospun nanofibers before annealing. Upon annealing in argon atmosphere, the nanofibers were transformed into BCN nanosheets, which is more favored in the presence of copper, Figure 20b. This can be attributed to the effect of copper nanoparticles that catalyze the transformation into the BCN nanosheets.[82,171] Figure 20c,d shows the exfoliated nanosheets after performing the chronopotentiometry (CP) measurements.

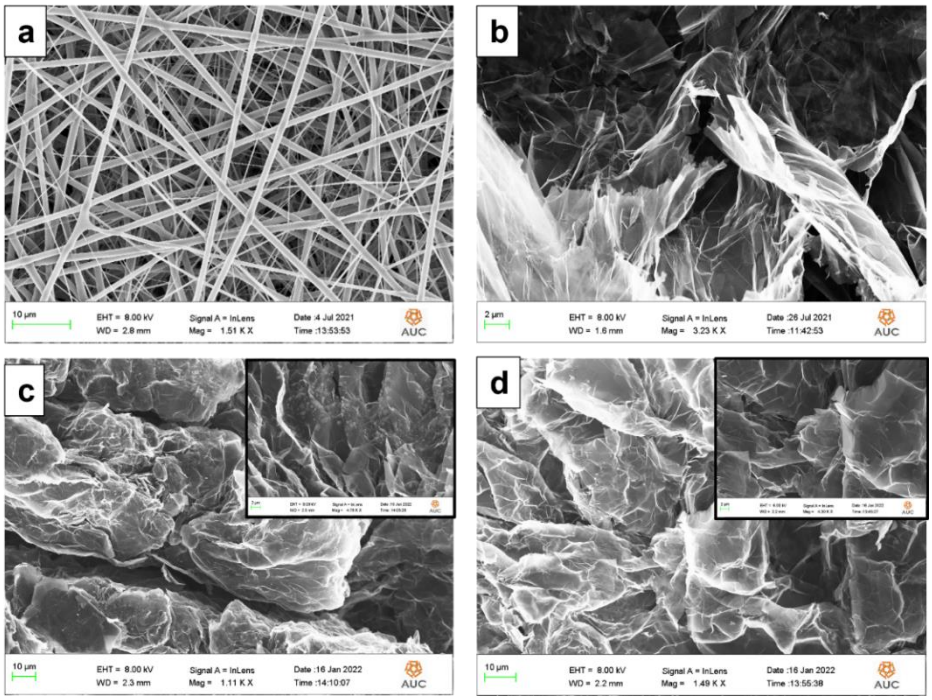

Figure 20 (a) FESEM images of the electrospun nanofibers before annealing, (b) the formed nanosheets after annealing in an argon atmosphere, (c,d) the exfoliated nanosheets after performing the chronopotentiometry (CP) measurements.

6.2 Chemical and crystal structure

6.2.1 FTIR analyses

FTIR analysis was performed to elucidate the chemical bonds formed in the fabricated composites as shown in Figure 21a. The FT-IR spectra of both BCN and BCN-Cu show similar vibration bands that are characteristic of carbonaceous materials. While the high intense band at 3435 cm^{-1} is characteristic of N–H stretching vibration, the bands at 2921.7 cm^{-1} and 2852.9 cm^{-1} are ascribed to C-H stretching. The bands characteristic of the N-H and C-H bending were also recorded at 1628.9 cm^{-1} and 1378.2 cm^{-1}, respectively.[172] The band around 1500 can be assigned to C-O axial deformation.[173] Note that it is shifted to ~1627 cm^{-1}, which may confirm the formation of copper complex, as the positions of C=O and NH_2 may overlap.[174] The band at 1119.7 confirms the formation of C-B bond, while both bands at 1050 and 1250 cm^{-1} are attributed to C-N stretching. [172,175]

6.2.2 RAMAN analyses

To further confirm the formation of BCN nanosheets, Raman measurements were conducted, see Figure 21b. The recorded Raman spectrum demonstrated the distinctive peaks at around 1372 and 1600 cm^{-1} related to the D and G bands, respectively, along with two weak signals at 2686 and 2920 cm^{-1} characteristic of the 2D band, in agreement with the reported Raman spectrum of BCN nanosheets.[176] The shift of the G band from the conventional peak of graphene (1580 cm^{-1}) confirms the distortion of the graphitic carbon due to the formation of N-B and C-N bonds with different bond lengths.[177] Moreover, the presence of a weak 2D band signifies the presence of a few layers of BCN nanosheets.[172,177,178] While the G-band represents the stretching of all sp^2 bonds (C-C, N-C, B-C, B-N), the D-band is related to the sp^3 defects.[179] The I_d/I_g ratio was calculated and found to be 0.95, 0.85, 1, and 0.87 for the as-prepared BCN nanosheets, BCN nanosheets after chronopotentiometry (CP), as-prepared 0.125 Cu-BCN nanosheets, and 0.125 Cu-BCN nanosheets after CP, respectively. In the presence of copper, the I_d/I_g ratio is higher, implying that more defects are evolved due to the more B and N incorporated into the graphitic network.[180] The decreased I_d/I_g ratio after CP measurements indicates the increase in ordering of sp^2 bonded graphitic domains, which is expected to improve charge transfer along BCN nanosheets.

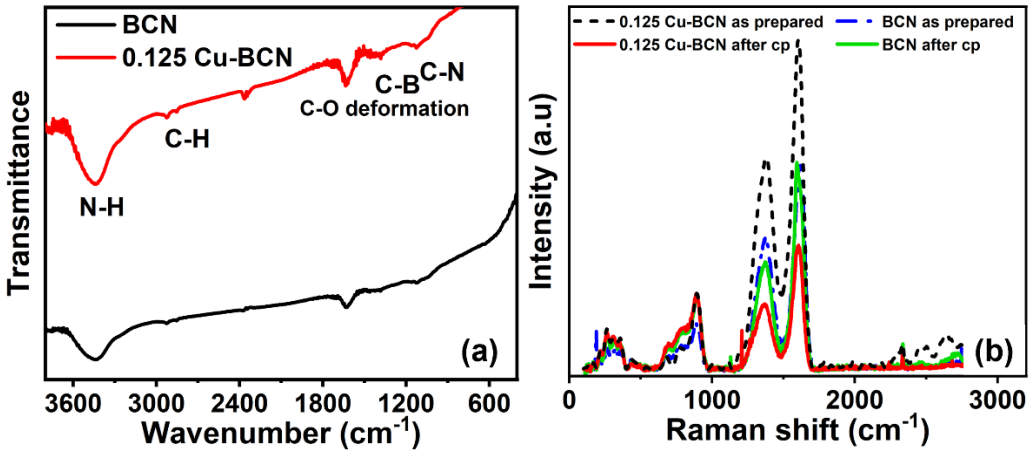

Figure 21 (a) FT-IR spectra of BCN and BCN-Cu nanosheets, (b) Raman shift of BCN and BCN-Cu nanosheets before and after chronopotentiometry (CP) measurements.

6.2.3 XPS analysis

The deconvoluted XPS B 1s spectra (Figure 22a) revealed two peaks at 190 and 192 eV that are characteristic of B-N-C and B-O bonds.[177,181–184] However, in presence of copper, the peak related to B-N-C is much more pronounced. For the C 1s spectrum (Figure 22b), the peak at 284.8 eV is related to the sp^2 C-C and C-O bonds, while the peak at 286.5 eV is related to the C-O bond. Interestingly, for BCN-Cu composite, a new peak was appeared at 288.82 eV, indicating the formation of C-N bond.[177,181,183,185] The N 1s spectrum (Figure 22c) was deconvoluted into two peaks at 398 and 400.1 eV, related to pyrrolic and pyridinic N, respectively.[175,177,183] Remarkably, the intensity of the pyridinic N peak was higher in the presence of Cu. Previous studies have shown that pyridinic-N has a basic lone pair of electrons that do not delocalize into the aromatic rings, hence, they are easily protonated forming pyridinic N-H.[186] The other three N configurations are hardly protonated.[68] Besides, pyridinic-N exhibits the lowest adsorption energy among the four N configurations, suggesting its high affinity towards H^+ adsorption.[186,187] The O 1s spectra (Figure 22d) shows a peak at 531.8 eV attributed to O-B bond. For BCN-Cu composite, the peak is shifted towards lower binding energy (531.7 eV), duo to the presence O-C and copper oxide, which usually appears around 532.5 and 529. 8 eV, respectively.[172,188] The Cu 2p spectrum (Figure 22e) exhibited two peaks at 933 and 952.9 eV corresponding to Cu^0, along with weak signals at 934.8 and 954.8 assigned to Cu^{2+}, which is also confirmed by the satellite peaks at 940 and 944.5 eV.[188,189]

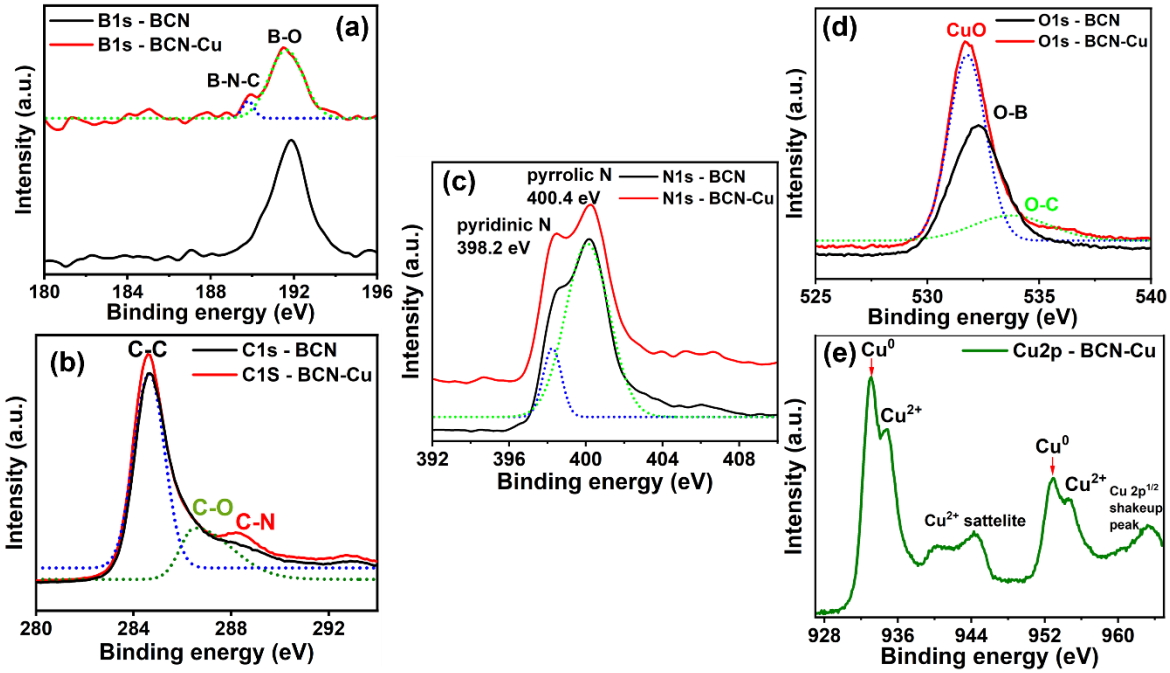

Figure 22 High resolution XPS scans of (a) C 1s, (b) N 1s, (c) Cu 2p, (d) N 1s, and (e) B 1s.

6.3 Electrocatalytic activity

The catalytic activity of the fabricated composites for the hydrogen evolution reaction (HER) was investigated in a three-electrode setup. The LSV polarization curves were recorded in 0.5 M sulfuric acid, Figure 23a. First, the electrodes prepared using binder (PVDF) were tested and compared to the electrodes that are binder-free, revealing that the presence of binder significantly reduces the catalytic activity of the material, as shown in Figure 23a,b. Thus, we decided to focus on the binder-free electrodes as the binder seems to hinder the charge transfer between the active sites of the catalyst and the conductive substrate.

As the copper loading increases, the overpotential is greatly reduced to a certain threshold (0.125 Cu-BCN) after which the activity starts to decline, see Figure 23b. Interestingly, the stability test at -100 mA/cm^2 showed that the overpotential is enhanced (getting closer to zero) over time. This is in contrary to what usually reported in the stability test, where the overpotential increases over time. Thus, we measured the overpotential after the CP test for all the composites fabricated. As shown in Figure 23c, a great saving in the overpotential needed to derive HER after the CP

test (at a current density of -100 mA/cm^2 for 10 hours) is observed, see Figure 24a, illustrating the volcano diagram of the recorded overpotentials before and after CP measurements, with lowest overpotential for the composite (0.125 Cu-BCN). This suggests that the enhancement after the CP test could be attributed to the reduction of Cu^{2+} into Cu^0. In order to investigate this assumption, LSV of pure copper foil was measured under the same conditions and compared to the LSV curves recorded after the CP test, as shown in Figure 23c. Copper foil showed almost the same potential of that of the 0.125 Cu-BCN electrode, confirming that the enhancement in the overpotential after the CP test is attributed to Cu^{2+} being reduced to Cu^0. Figure 23d illustrates the reduction observed in the overpotential before and after CP measurements. Figure 25a shows the reduction in the overpotential along the CP test. It is worth noting that pure Cu foil was completely unstable under the same experimental conditions, see Figure 24b.

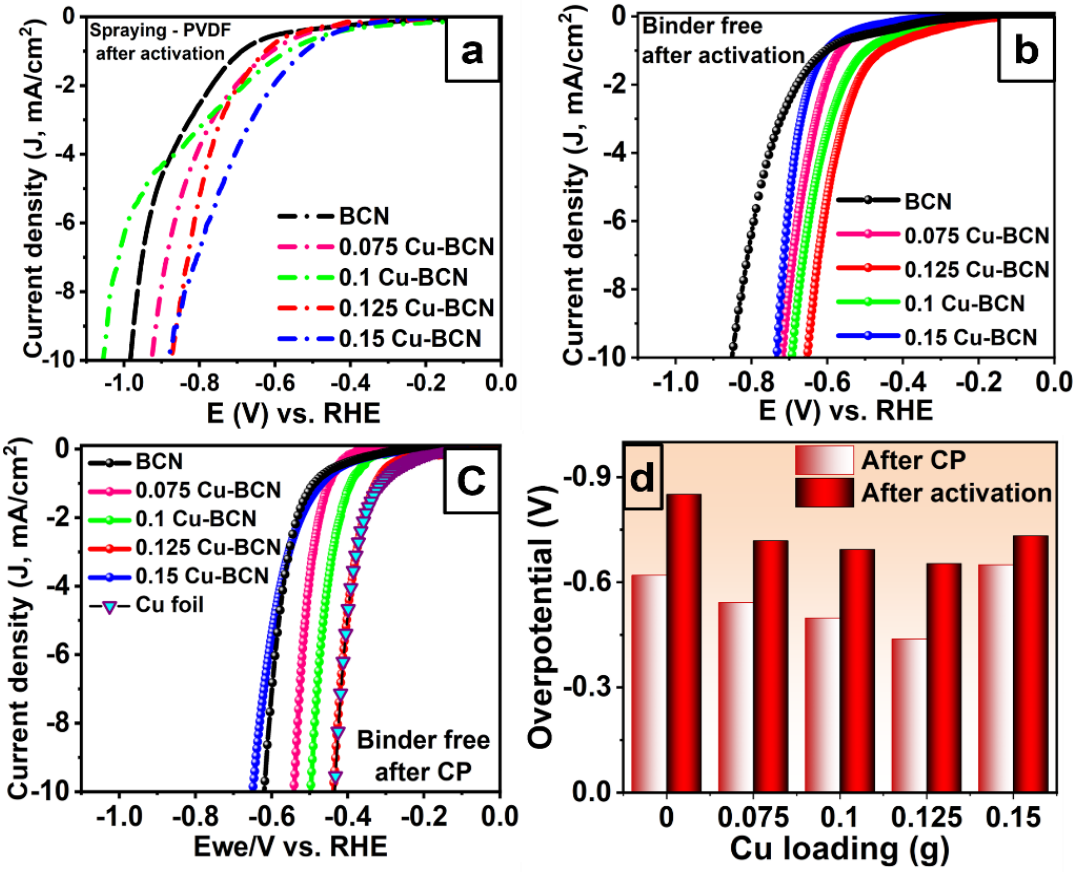

Figure 23 LSV curves of (a) the electrodes prepared using PVDF as a binder after activation and (b,c) for the binder-free electrodes after activation and after chronopotentiometry (CP), respectively, (d) Variation of the overpotential with Cu loading after activation and after CP measurements.

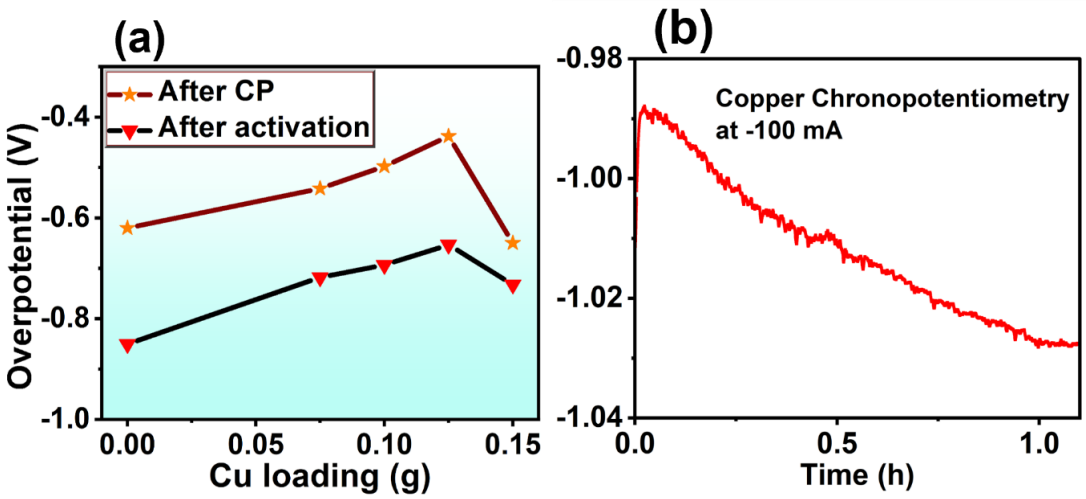

Figure 24 (a) Volcano diagram of the recorded overpotentials. (b) stability test of copper.

Upon identifying the best performing composite with the best catalytic activity (0.125 Cu-BCN), the kinetics of the HER of this composite was elucidated and compared to that of pure BCN. The Tafel slopes were calculated for BCN and 0.125 Cu-BCN after activation and after CA from the Tafel equation [$\eta = a + b \log j$], where j, η, a, and b are the current density, overpotential, transfer coefficient, and Tafel slope, respectively. The 0.125 Cu-BCN electrode showed lower Tafel slopes (151.7 after activation and 114.5 after CP) than that of BCN nanosheets (218.2 after activation and 187.9 after CP), Figure 25b. Note that the Tafel slopes are much lower after CP measurements for both materials. The lower Tafel slopes after activation and after CP measurements for the 0.125 Cu-BCN nanosheets suggest that the presence of reduced copper accelerates the kinetics of the reaction due to its high electron density, resulting in reducing the overpotential, which is in agreement with the LSV data.

The catalytic activity of the fabricated composites was further investigated via the estimation of the electrochemical active surface area (ECAS) from the double-layer capacitance.[79] The cyclic voltammetry measurements were conducted in the potential range from 0.45 to 0.65 V vs RHE at different scan rates (5, 10, 20, 30, 50, 70 and 100 mV/s), see Figure 26. The double layer capacitance C_{dl} was obtained by plotting the differences between the anodic and the cathodic currents of the cyclic voltammograms versus the scan rate. As shown in Figure 25c, the 0.125 Cu-BCN composite showed much higher C_{dl} and ECSA values of 12.7 mF cm^{-2} and 317.7 cm^2, respectively, while pristine BCN has a C_{dl} of 7.52 and ECSA of 187.9 cm^2. This reveals that the

0.125 Cu-BCN composite possesses more active sites available for hydrogen adsorption, which facilitates and enhances the efficiency of the HER.

To further understand the reason behind the significant enhancement upon the incorporation of copper with the BCN, the charge transfer at the electrode/electrolyte interface was propped using electrochemical impedance spectroscopy at an AC voltage of 5 mV in the frequency range of 105 - 1 Hz, as shown in Figure 25d. The Nyquist plots measured after activation shows the 0.125-Cu-BCN composite to exhibit lower charge transfer resistance, R_{CT}, (2.99 Ohm) than that of pristine BCN (4.22 Ohm). However, after CP, the R_{CT} was further reduced to 2.234 Ohm for the 0.125 Cu-BCN nanosheets. The lower R_{CT} implies faster electron transfer rate due to the presence of reduced copper and the exfoliation process taking place during the CP measurement, resulting in accelerated HER kinetics. This explains the observed reduction in the overpotential of the Cu-BCN nanosheets as revealed from the LSV curves and the higher ECSA of the Cu-BCN nanosheets than that of bare BCN. As the ideal HER catalyst should show fast charge transfer, high exchange current densities, low overpotential, and low Tafel slope, our fabricated Cu-BCN nanosheets should have great potential to be efficient HER electrocatalysts.

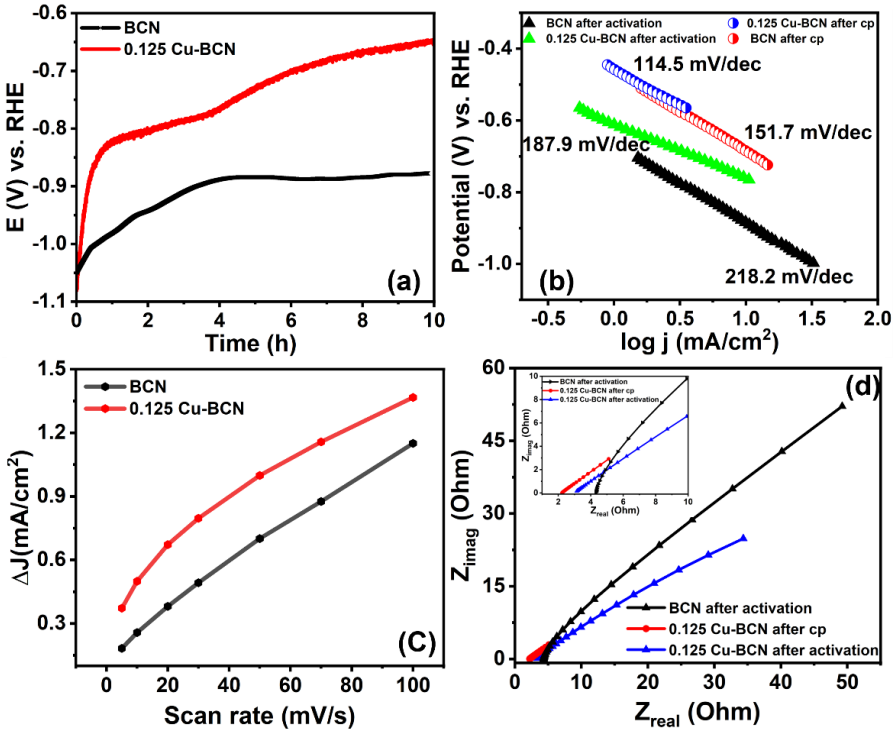

Figure 25 (a) CP measurements of BCN and BCN-Cu nanosheets, (b) Tafel slopes of BCN and

BCN-Cu nanosheets after activation and after CP measurements, (c) ECSA of BCN and BCN-Cu nanosheets after activation, (d) Nyquist plot of BCN-Cu nanosheets after activation and BCN-Cu after CP measurements.

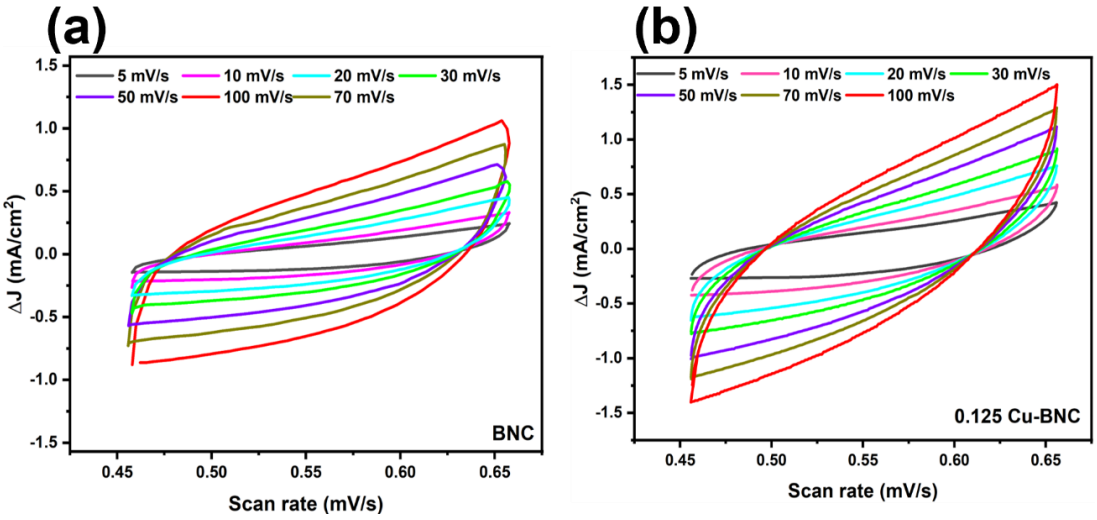

Figure 26 (a,b) cyclic voltammetry measurements were conducted within the potential range from 0.45 to 0.65 V vs RHE with different scan rates (5, 10, 20, 30, 50, 70, and 100 mV/s).

6.4 Electrochemical exfoliation

The FESEM imaging of the material after CP measurements showed a remarkable change in the morphology of the working electrodes, as shown in Figure 20c,d. Note that the density of the sheets drastically increased, suggesting electrochemical exfoliation. This is probably related to the presence of SO_4^{2-} anions in the electrolyte.

Parvez *et al.*[72] suggested that the following exfoliation mechanism once a potential is applied. Oxygen (O•) and hydroxyl radicals (OH•) are formed due to the presence of H_2O, then, these radicals initiate hydroxylation or oxidation at the edge and grain boundaries of the electrode creating defect sites, which enable the intercalation by SO_4^{2-} anions, hence expanding the interlayer distance between the sheets, as illustrated in Figure 27a. This was further validated by the EDX spectra obtained after CP measurements, where a peak related to sulfur was recorded even after soaking the sample in ethanol for 24 hours, as shown in Figure 27b This process makes the surface of the nanosheets more accessible for the hydrogen ions to be adsorbed on the catalytic sites and assisting the reduction reaction.[190]

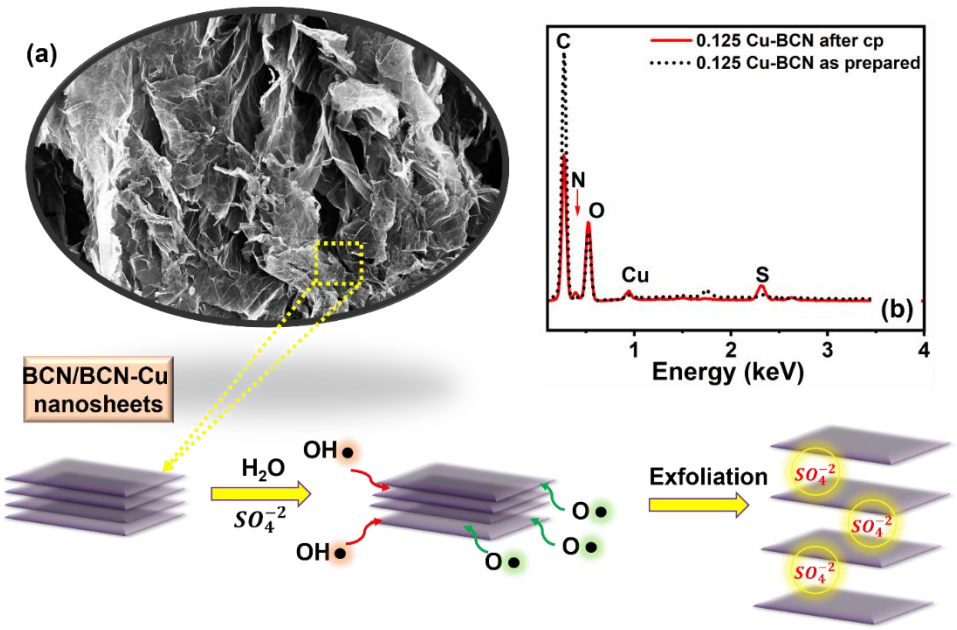

Figure 27 (a) Schematic illustration of the electrochemical exfoliation of BCN nanosheets and (b) EDX of BCN and BCN-Cu nanosheets after CP measurements.

6.4 DFT results

To further elucidate the observed enhanced activity, density functional theory (DFT) calculations were employed to study the influence of combining CuO and Cu^0 with BCN nanosheets on the electronic structure of BCN and hence on the HER activity. ΔG_{H+} gives a clear and solid indication on how the change in the catalyst surface can affect the thermodynamics of the HER. Ideally, the free energy of hydrogen adsorption (ΔG_{H^*}) for the catalyst used should be near zero.[42,] Consequently, Gibbs free energy was calculated using the computational hydrogen electrode (CHE) method as reported in chapter 4. At equilibrium and under standard pressure, the free energy of electron-proton pair ($H^+ + e^-$) is assumed to be half the potential of hydrogen gas (U = 0 versus SHE) and any step that involve electron-proton pair is shifted by −eU at any U versus the SHE. The free energy also includes the entropy correction at 298.15 K along with the zero-point vibrational energy (ZPVE). The optimized geometries for BCN/Cu^0 and BCN/CuO are shown in Figure 15a,b and Figure Figure 28.

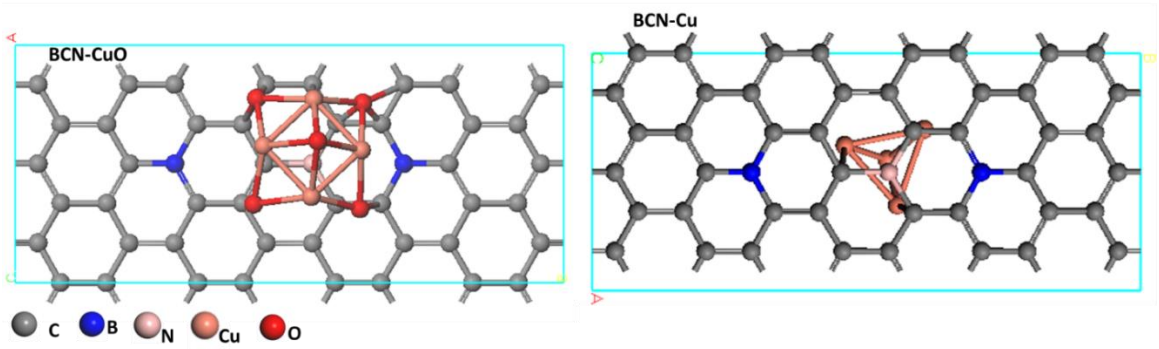

Figure 28 Optimized geometries for top view for BCN-CuO (left) and BCN-Cu (right).

The presence of CuO and Cu^0 clusters on BCN significantly enhances hydrogen adsorption on the surface and reduces the Gibbs free energy from 0.8 eV to -0.51 and -0.14 eV for CuO-BCN and Cu^0-BCN nanosheets, respectively, see Figure 29a. Thus, incorporating copper into BCN nanosheets is expected to enhance the activity of HER as it shifts ΔG_H^* closer to 0 eV, which enables H^+ adsorption, reduction, and desorption. BCN/Cu has smaller negative free energy (-0.14 eV) than the other two composites, which is closer to the thermoneutral versus -0.51 and 0.8 eV for BCN/CuO and BCN, respectively. The positive energy for BCN means that H^+ has weak affinity towards binding to the BCN surface. On the other hand, the large negative energy in case of CuO indicates the strong affinity to H^+, making it very hard to desorb. Thus, we conclude that Cu^0 exhibits the optimum binding energy of H^+, which facilitates both the reduction and desorption and improves the overall HER.

To obtain a deeper theoretical understanding of the water splitting on the BCN anchored with Cu cluster, we compared the electron density around the water molecule upon adsorption on BCN and BCN-Cu surfaces, we found that the presence of copper leads to a hybridization of the antibonding orbitals with the copper 3d orbital that resulted in a strained O-H bonds and H-O-H angle upon adsorption on the surface. The higher bond length of the O-H of the adsorbate, the more interaction between the adsorbent and the adsorbate molecules, which enhances the water splitting activity on the surface. as shown in Figure 29b,c. Once the water molecule is adsorbed on the surface, the charges are effectively transferred as a result of the interaction between the water molecule and the copper 3d orbitals. The hybridization of the 3d copper orbital and the antibonding orbital of the water leads to a gradual filling of the antibonding orbital. Therefore, from the analysis of the charge density distribution difference, we can anticipate the

charge transfer from the population of the electrons along the Cu-H_2O bond with a diminution on the charge density on the water molecule. This confirms the weakening of the O-H orbitals and the orbital overlap with the water antibonding orbital, leading to a stretched O-H bond after adsorption on the copper supported BCN, the O-H bond length along with the H-O-H angle upon adsorption on the surface of BCN and BCN-Cu are presented in Table 2.

Table 2 Bond length and H-O-H angle of water molecule after adsorption on the BCN and BCN-Cu surfaces.

Structure	O-H1(Å)	O-H_2 (Å)	H-O-H°
Water	0.977	0.977	104.528
BCN-H_2O	0.981	0.977	104.808
Cu supported BCN-H_2O	1.01532	0.980	105.577

Additionally, from the Mulliken charge analysis, the negative charge of the oxygen atom was decreased from -1.03 a.u. for BCN to -0.83 a.u. for the copper supported BCN structure, indicating the higher charge transfer between the water molecule and the BCN-Cu structure in comparison to the pristine BCN structure. This was confirmed by two main investigations; the first is an increase of the bond population of the BCN-H_2O bond by 0.25 according to the Mulliken bond population analysis. The second is a decrease of the charge density of the water molecule as illustrated in Figure 29b,c.

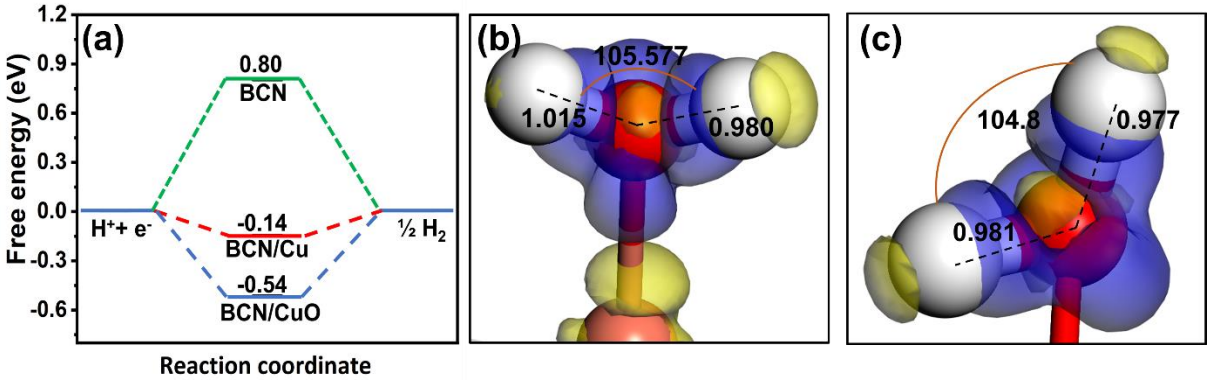

Figure 29 (a) free energy changes (ΔG_{H^*}) of H adsorption on BCN and BCN-Cu nanosheets. (b) and (c) The blue areas show where the electron density has been enriched, while the yellow areas show where the density has been depleted.

The difference in charge transfer in presence of CuO and Cu^0 is another aspect that was studied using DFT trying to understand why there was a reduction in the overpotential needed to drive the HER before and after the CP measurements. The density of states in Figure 30a,b reveal the formation of trapping states in the case of CuO coming from the P orbitals of the oxygen, which increase the charge recombination rate and hinders charge transfer to the conduction band. Thus, although the catalytic activity is enhanced in presence of Cu^0 and CuO as concluded from XPS and electrochemical measurements, the catalytic activity of BCN-CuO nanosheets is still limited as BCN/CuO exhibits a semiconducting nature with a band gap of 1.86 eV. However, after CP measurements, the reduction of CuO to Cu^0 causes enhanced charge transfer as confirmed from the experimental and theoretical calculations, due to the absence of these trapping states in the case of Cu^0 and the overlap between the VB and the CB, as concluded from the DOS, Figure 30c. Therefore, in agreement with the experimental results, BCN/Cu^0 shows metallic nature, which facilitates electron transfer and enhances the HER activity.

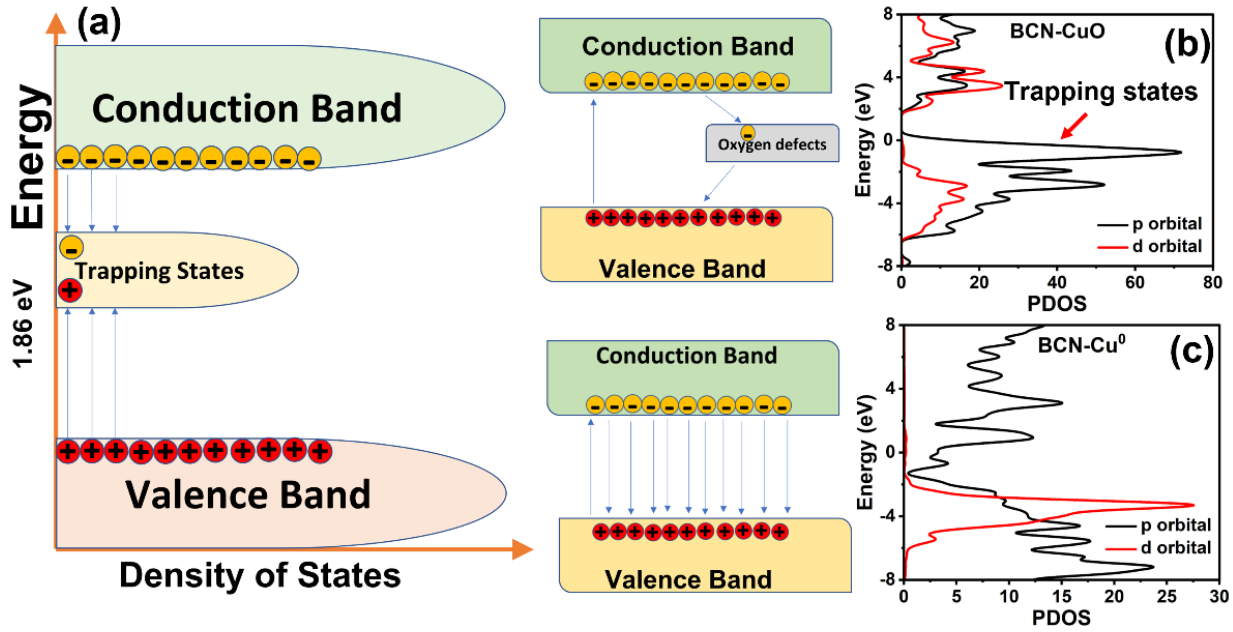

Figure 30 (a) Schematic diagram for the DOS and trapping states for CuO-BCN, and (b,c) the PDOS and the structure of BCN-CuO and BCN-Cu^0 nanosheets, respectively.

6.5 Conclusion

In summary, we report the fabrication of BCN and BCN-Cu nanosheets via a new emerging and facile technique, the fabricated composite showed superior performance as a non-noble metal catalyst for HER. Using a combination of DFT calculations and experimental analysis, according to our measurements, we revealed that there is a substantial reduction in the overpotential after CP measurements due to electrochemical exfoliation and the complete reduction of copper oxide into metallic copper with much higher charge density available to perform HER. As the CuO result in trapping states and rapid recombination. We also demonstrated that the sample 0.125 Cu-BCN has the highest catalytic activity towards HER with a reduction in the overpotential needed to almost 50% of the value recorded for BCN nanosheets, due to the synergistic interconnection between BCN and copper nanoparticles, resulting in better charge separation and faster charge transfer. Moreover, using DFT calculations, we found that incorporating copper as a catalyst on BCN result in drastically reducing G_{H^*} value for the HER near to the ideal value which indicates that it has an excellent catalytic activity in acidic medium. and subsequently accelerates the kinetics of the reaction and the overall catalytic activity of the material, in accordance with the experimental findings. The feasibility and low manufacturing cost of our methodology will pave the way to introduce new metal free electrocatalysts for HER and other related technologies.

Chapter 7 Results and discussion

Unveiling the Interfacial Interactions of C_{76}/Ni Foam Heterostructures for High-Performance Hydrogen Evolution Reaction Electrocatalysis

7.1 DFT exploration of different fullerenes

Density functional theory (DFT) calculations were performed on the commercially available high fullerenes to investigate the promising candidates as HER catalysts. The calculated bandgap energies of C_{60}-Ih, C_{70}-D_{5h}, C_{76}-D2, C_{84}-D_{2d}, and C_{100}-D_{5d} were found to be 2.77, 2.68, 1.98, 2.15, and 2.39 eV, respectively, as shown in Figure 31a. The obtained bandgaps are in agreement with those reported in the literature.[192] Interestingly, C_{76} showed the lowest band gap energy compared to the other investigated fullerenes. Thus, C_{76} is expected to be the most promising fullerene structure in electrocatalysis due to its high conductivity. Note that the calculated density of states of C_{76}-D2 revealed its semiconducting characteristics, Figure 31b.

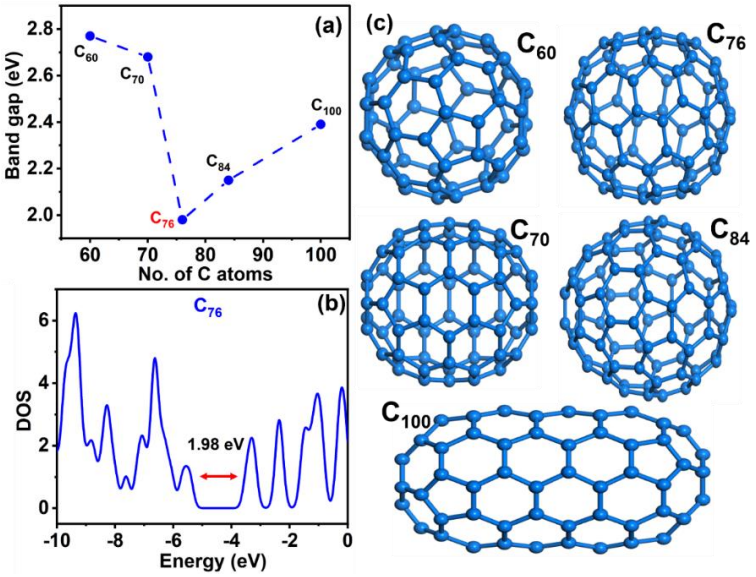

Figure 31. (a) Band gap energies of C_{60}, C_{70}, C_{76}, C_{84}, and C_{100} fullerenes, (b) density of states (DOS) of C_{76}-D2, and (c) the structure of the investigated fullerenes.

As C_{76} is formed of carbon with hexagon and pentagon rings, it has two possible adsorption sites. The calculated adsorption energy of H^+ on both sites (Figure 32) revealed a lower adsorption energy on the hexagon ring (0.61 eV) than on the pentagon counterpart ring (0.92 eV). Therefore, the hexagon site is more favorable for H^+ adsorption.

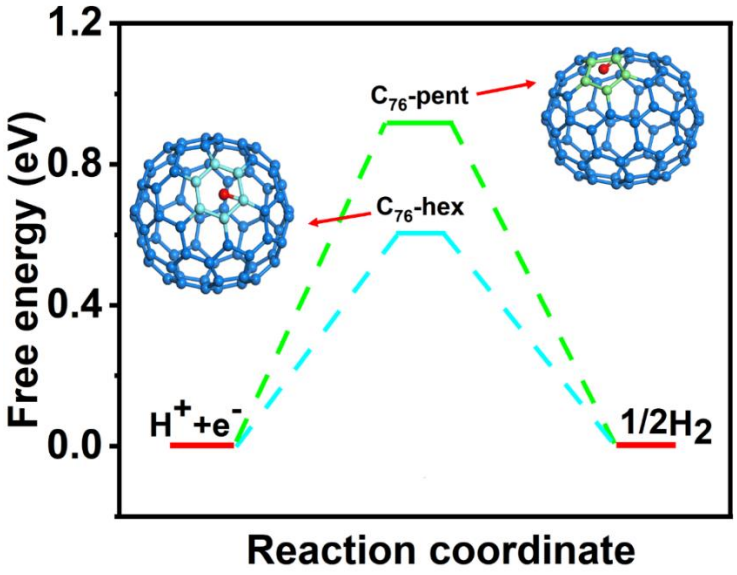

Figure 32 Free energy changes (ΔGH) of H adsorption on fullerene pentagon site and fullerene hexagon site.

7.2 Morphology

The results obtained from the DFT calculations encouraged us to test C_{76} experimentally as a potential catalyst for HER. The morphology of C_{76} was examined using FESEM imaging, as shown in Figure 33a. Due to the small size of C_{76} Buckyball (around 0.9 nm), it tends to agglomerate forming nanoclusters of 26 to 66 nm in size as depicted in Figure 34. This was further confirmed using TEM as shown in Figure 33b. Being of a size smaller than 1 nm,[192–194] C_{76} is very hard to be recognized separately, thus it appears as small spheres.

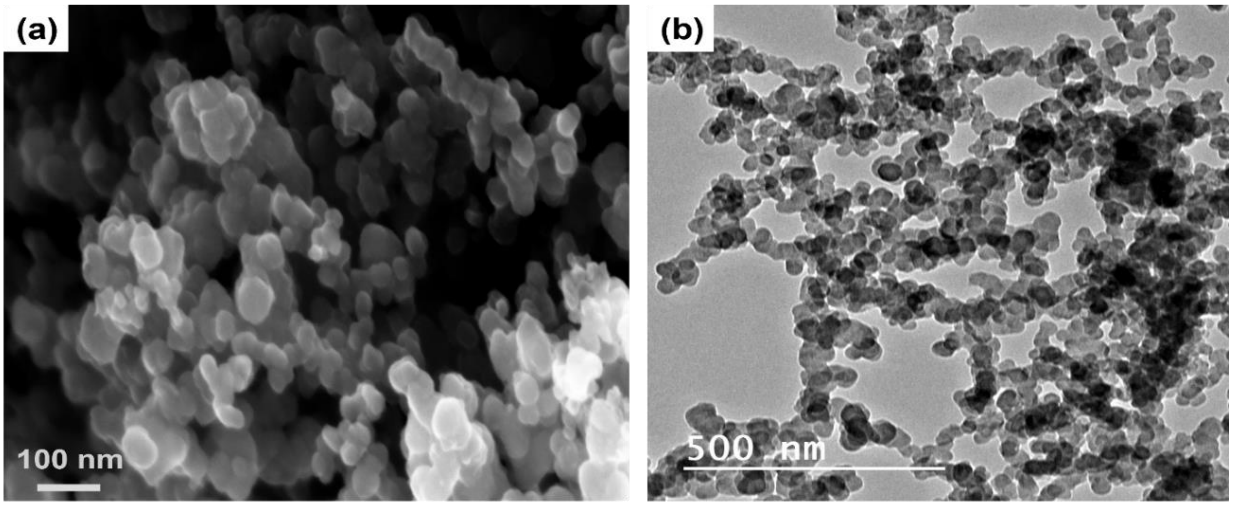

Figure 33. (a) FESEM and (b) TEM images of C_{76}.

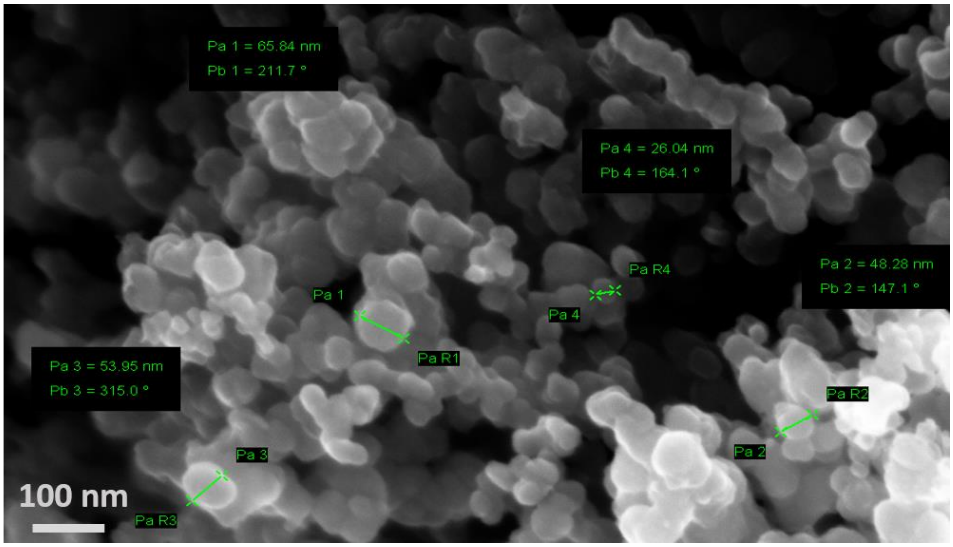

Figure 34 SEM image showing the size of the nanoclusters formed by C_{76}.

7.3 Structural characterization

7.3.1 BET analysis

N_2 gas adsorption/desorption isotherms were recorded at 77 K to estimate the surface area and the porosity of C_{76}, Figure 35a. Based on the IUPAC classification, the adsorption/desorption isotherm is of type IV with H3 hysteresis loop, revealing that C_{76} has micro and mesopores.[195] The non-local density functional theory (NLDFT) and Brunauer-

Emmett-Teller (BET) fitting of the isotherm revealed that C_{76} has a surface area of ~34 m^2/g. According to NLDFT fitting, the surface area is around 26.8 m^2/g. The distribution of the measured pore diameters indicates that most of the pores have a diameter of ~ 2.9 nm, suggesting the microporous structure of C_{76}. According to the literature, the size of water molecule ranges from 0.27 to 0.3 nm.[196] Thus, we believe that the large pore size relative to the water molecule enables the water molecules to get adsorbed on the outer and inner surfaces of C_{76}, hence offering very high surface area and number of active sites.

7.3.2 XPS analysis

The C 1s XPS spectrum of C_{76} showed three peaks at 284.4, 285, and 288.9 eV corresponding to the binding energies of C-C sp^2, C-C sp^3, and C-OH/C-OOH, respectively, Figure 35b.[197] The peak assessment of C 1s revealed that the hybridization in C_{76} is 60.7% sp^2, which is expected as the carbon atom undergoes sp^3 hybridization to form the single bond in the pentagon, while three sp^2 hybridized orbitals representing three σ bonds. Moreover, XPS data analysis implies that C_{76} is oxygen-functionalized, enhancing its hydrophilicity and improving the contact between the electrolyte and the C_{76} surface.[194,198,199] According to previous studies, oxygen functionalization facilitates proton conduction.[200]

7.3.3 FTIR analysis

To further investigate the function groups in the C_{76}, FTIR analysis was conducted, as shown in Figure 35c. The stretching vibrations related to C=C, C=O, and O-H were evident at 1577.8, 1648, and 3410 cm^{-1}, respectively.[201] Furthermore, the signals recorded at 2378 and 1384.8 cm^{-1} are related to the O-H stretching and C-OH bending vibrations of the COOH group, while the band at 1440 cm^{-1} is attributed to the δ(O-H) mode.[202–204] Those function groups are expected to enhance the conductivity and wettability of C_{76}.[194]

7.3.4 RAMAN analysis

Raman spectroscopy was used to further understand the composition and explore the defects present in C_{76}, Figure 35d. The D and G bands were recorded at 1343.6 and 1578 cm^{-1},

respectively. The G-band distinguishes graphitic carbon, coming from the in-plane band stretching of the sp^2 C-C bond in pentagons and double bonded hexagons with E_{2g} symmetry. The D-band is characteristic of the breathing mode of the A_{1g} symmetry, representing the defects in the graphitic hexagons. The calculated I_D/I_G ratio is 0.94, revealing the high order structure of C_{76}. Moreover, the 2D and D+G bands at 2950 cm^{-1} and 2676 cm^{-1} reveal the crystallinity of the material, indicating the high potential electrochemical and catalytic activity of C_{76}.[205,206]

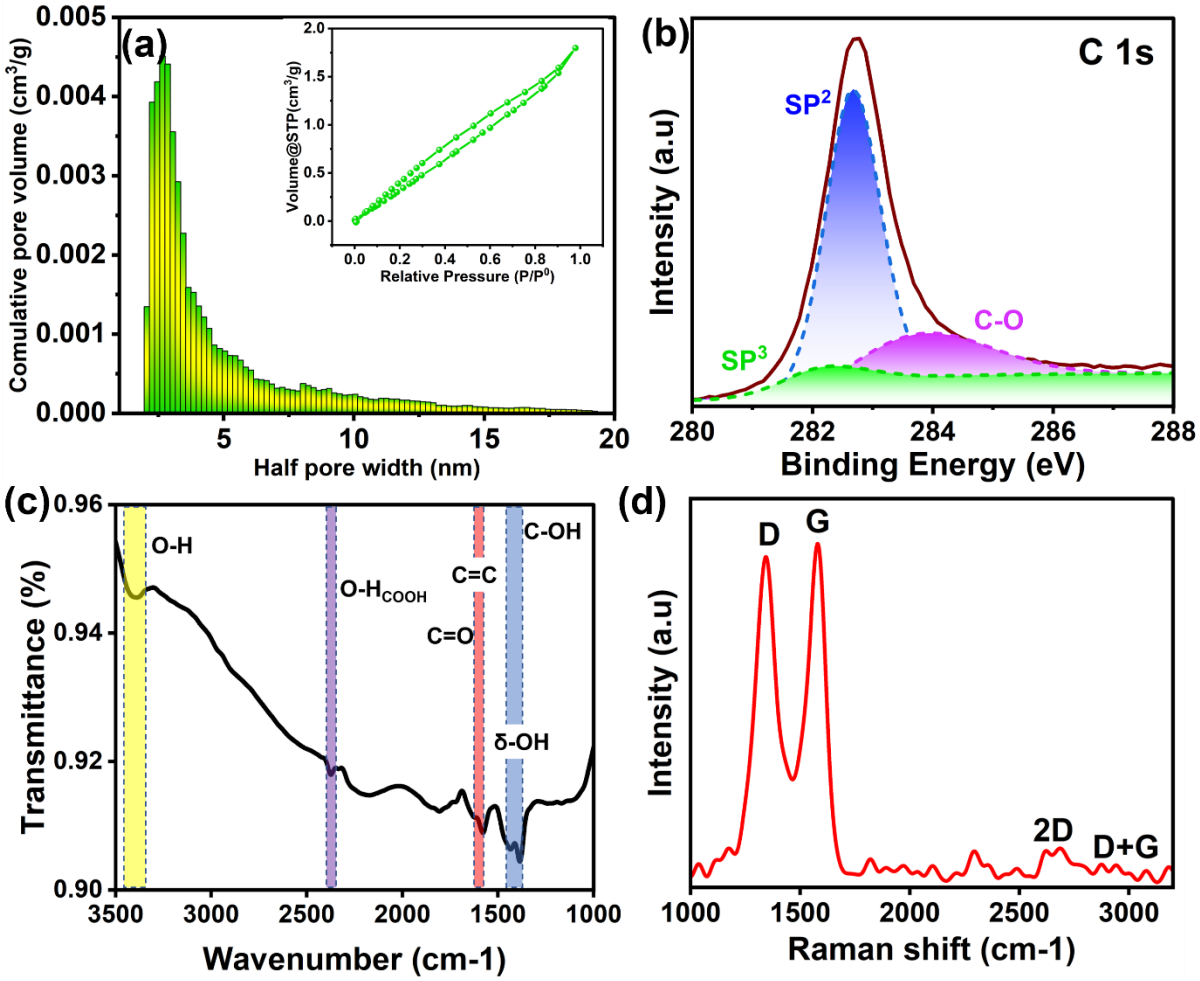

Figure 35. (a) NLDFT pore volume distribution, the inset is for the adsorption/desorption isotherm, (b) FT-IR spectra, (c) Raman spectra, and (d) C 1s XPS spectra of C_{76}.

7.4 Electrochemical measurements

As the DFT calculations, the imaging, and structural characterizations predict the potential of C_{76} as an HER catalyst, the electrocatalytic activity of C_{76} was investigated experimentally. The HER linear sweep voltammetry (LSV) polarization curves were first recorded for bare Ni-foam and C_{76} deposited on graphite sheet to elucidate their catalytic activity separately. As graphite sheet is almost inactive towards HER, the recorded activity would be solely attributed to C_{76}. Finally, the LSV curves of Ni foam loaded with different amounts of C_{76} were recorded to understand the effect of the interfacial interactions between Ni foam and C_{76} on the activity and kinetics of the HER.

As shown in Figure 36a, while C_{76} shows relatively low activity towards HER and Ni foam has an overpotential of 420 mV at -10 mA/cm^2, loading the Ni foam with 0.12 mg, 0.48 mg, and 0.53 mg of C_{76} resulted in a significant reduction in the overpotential needed to derive the HER to 270, 45, and 20 mV, respectively at -10 mA/cm^2. Those overpotentials are almost the same as that reported for the benchmark 20 wt% Pt/C electrocatalyst. Those findings reveal the unique and desirable electronic properties of C_{76}-Ni, which resulted in an outstanding catalytic activity towards HER. This can be ascribed to the superior charge transfer between Ni foam and C_{76} and the increase of the charge density on C_{76} when deposited on Ni foam as will be demonstrated later. Besides, the C_{76}/Ni offers high surface area with an enormous number of catalytic sites.

To elucidate the kinetics of the HER, the exchange current density (j_0), the charge transfer coefficient (α), and the mass activity (MA) were calculated from the corresponding LSV curves. The obtained j_0 values are 0.084, 12.298, and 6.085 A/cm^2 for the 0.12, 0.48, and 0.53 mg C_{76}-containing electrodes, respectively, Figure 36b. Moreover, the calculated α values are 8.316×10^{-5}, 8.316×10^{-5}, and 6.024×10^{-5}, respectively. Note that low α and j_0 values indicate sluggish reaction kinetics, resulting in higher overpotentials, while high α and j_0 values reveal fast reaction kinetics, enhanced catalytic activity, and low overpotential. Surprisingly, although, 0.48 and 0.53 mg C_{76}-containing samples show almost the same overpotential, the 0.48 mg C_{76}-containing sample showed higher j_0. Besides, as depicted in Figure 36c, the mass activity calculations, which are more reliable quantitative descriptors of the electrocatalytic activity, showed that only at low overpotential the 0.53 mg C_{76}-containing sample gives higher mass activity.

Nevertheless, as the potential increases, the 0.48 mg C_{76}-containing electrode exhibits the highest mass activity. This comes in agreement with the calculated kinetic parameters (α and j_0), revealing that the 0.48 mg C_{76}-containing sample shows the fastest reaction kinetics. Finally, the stability of the C_{76}-Ni foam electrodes was elucidated using the chronoamperometry technique at -100 mA/cm^2 for 24 h, as illustrated in Figure 36d. The electrodes are highly stable and after 24 h the overpotential increased only by 14%, indicating the resilience of the electrodes under tough acidic conditions and the very high applied currents.

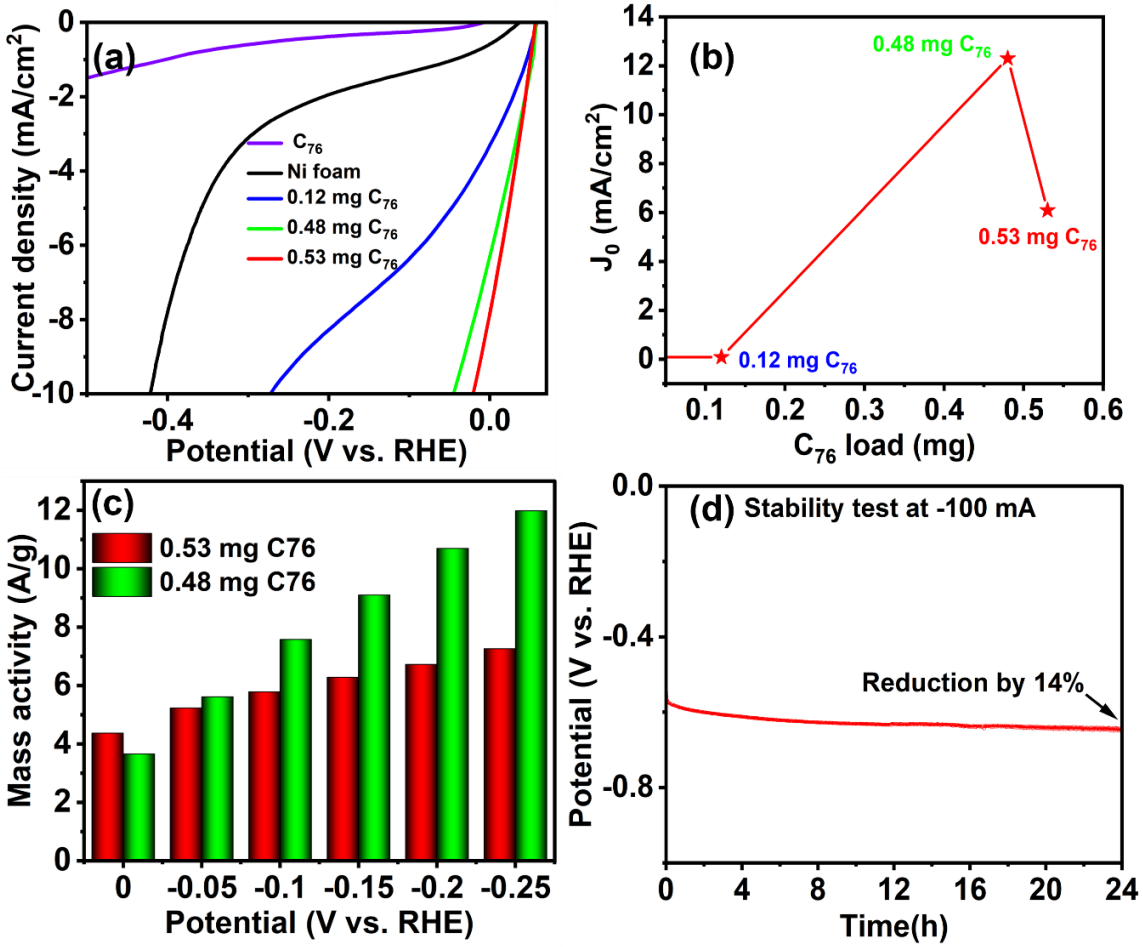

Figure 36. (a) LSV plots of Ni foam and Ni foam loaded with different amounts of C_{76}, (b) the corresponding j_0 values, (c) mass activity of the Ni foam with different C_{76} loads, and (d) stability measurements of the Ni foam-C_{76}.

To elucidate the origin of the developed unique electronic properties upon the deposition of C_{76} on Ni foam, the interaction between C_{76} and Ni-foam was simulated to understand the

interfacial interactions using DFT calculations. In acidic medium, HER involves three steps, starting with $H^+ + e^-$, followed by adsorption of hydrogen on the surface adsorption sites, and ending by the evolution of ½ H_2 as the product.[116] The Gibbs free energy difference $|\Delta G_H^*|$ is a measure of the catalyst activity. It should not be very strong or very weak to allow adsorption and desorption of hydrogen. A largely negative free energy value means strong affinity of hydrogen to adsorption, while a largely positive value means weak affinity of H^+ to adsorption. Therefore, a $|\Delta G_H|$ close to zero is characteristic of excellent HER catalyst.[111] The adsorption energy was calculated using equation (49)

$$\Delta E = E_{surf+H} - E_{surf} - \frac{1}{2} E_{H_2} \quad (49)$$

The Gibbs free energy of hydrogen was calculated using equation (50):

$$\Delta G = \Delta E + \Delta ZPE - T\Delta S \quad (50)$$

where ΔZPE is the difference in zero point energy and ΔS is the difference in entropy between the adsorbed state and the gas phase. Since $\Delta ZPE - T\Delta S \approx 0.28$ eV, $\Delta G = \Delta E + 0.28$ eV.

The electron density difference (EDD) was also calculated to unveil the electron density at the C_{76}/Ni interface. The noted electron accumulation may result in charge redistribution, which can provide more active sites for the HER. The electron density increased in some regions (red color) mainly on fullerene, and decreased on nickel (grey color) as shown in Figure 37a,b. This indicates the synergy between C_{76} and Ni foam in allowing electron transfer from nickel to C_{76} and acting as a superior bifunctional catalyst, which may explain the enhanced HER catalytic activity. The interaction between C_{76} and Ni resulted in the creation of interface dipole layer (IDL). This was further confirmed by the calculated ΔG_H^* for the adsorption on C_{76}/Ni foam (-0.09 eV) versus -0.43 eV for the adsorption on bare Ni foam, as shown in Figure 37c, confirming the synergistic effect at the C_{76}/Ni interface. The resulting increase in the electron density on C_{76} was able to decrease the ΔG_H^* down to -0.09 eV that is the closest to zero.

When the net rate of the forward reaction is much faster than the rate of the reverse reaction, the surface concentration of the reactant and product species changes. The concentration dependence of the exchange current density can be investigated using Butler–Volmer equation, equation (51).

$$\mathbf{j = j_0^0 \left\{ \left[\frac{C_R^*}{C_R^{0*}} e^{\alpha n F \eta/(RT)} \right] - \left[\frac{C_P^*}{C_P^{0*}} e^{-(1-\alpha) n F \eta/(RT)} \right] \right\}} \quad \textbf{(51)}$$

where η is the voltage loss (or activation overvoltage), n is the number of electrons transferred in the electrochemical reaction, C_R^* and C_P^* are the actual surface concentrations of the rate-limiting species in the reaction, and j_0^0 is measured at the reference reactant and product concentration values C_R^0 and C_P^{0*}. Effectively, j_0^0 represents the exchange current density at a "standard concentration.".[112] To achieve faster reaction kinetics, j_0 needs to be increased, which represents the rate of exchange at equilibrium between reactant and product species. As we are mainly interested in the forward reaction, we can use equation (52) for simplicity to calculate J_0:

$$\mathbf{J_0 = nFC_R^* f_1 e^{-\Delta G_1^{\ddagger}/(RT)}} \quad \textbf{(52)}$$

where J_0 is the exchange current density, n is the number of electrons transferred in the electrochemical reaction, F is Faraday's constant, C_R^* is the actual surface concentrations of the rate-limiting species in the reaction, f_1 is the decay rates to products, e is the electron charge, $\Delta G_1^{\ddagger}$ is the activation barrier (denoted as ΔG_H^*), R is the ideal gas constant, T is the temperature in K.

Equation (52) describes the correlation between the size of the activation barrier ($\Delta G_1^{\ddagger}$) and J_0. From this equation, we conclude that we can increase J_0 and accordingly facilitate the kinetics of the reaction if we are able to decrease $\Delta G_1^{\ddagger}$. As $\Delta G_1^{\ddagger}$ is an exponent in this equation, even small reduction in $\Delta G_1^{\ddagger}$ will significantly increase j_0. Thus, an efficient electrocatalyst should be able to lower the activation barrier of the targeted reaction by changing the free energy of the reaction. This is usually done by manipulating the nature of the bond between the catalyst and H^+. This bond should be of intermediate strength that it is not very strong. Figure 37 illustrates how our catalyst fulfills these requirements, As illustrated in Figure 37c, the DFT calculations show that

Ni foam lowers the activation barrier, with the reduction in the activation barrier is much higher for the combination C_{76}/Ni. Note that the free energy is reduced by 0.34 eV. Moreover, from J_0 calculations, we can see that this reduction in the activation barrier resulted in a massive increase in the exchange current as it increased by almost 6 A, as demonstrated in Figure 37d,e.

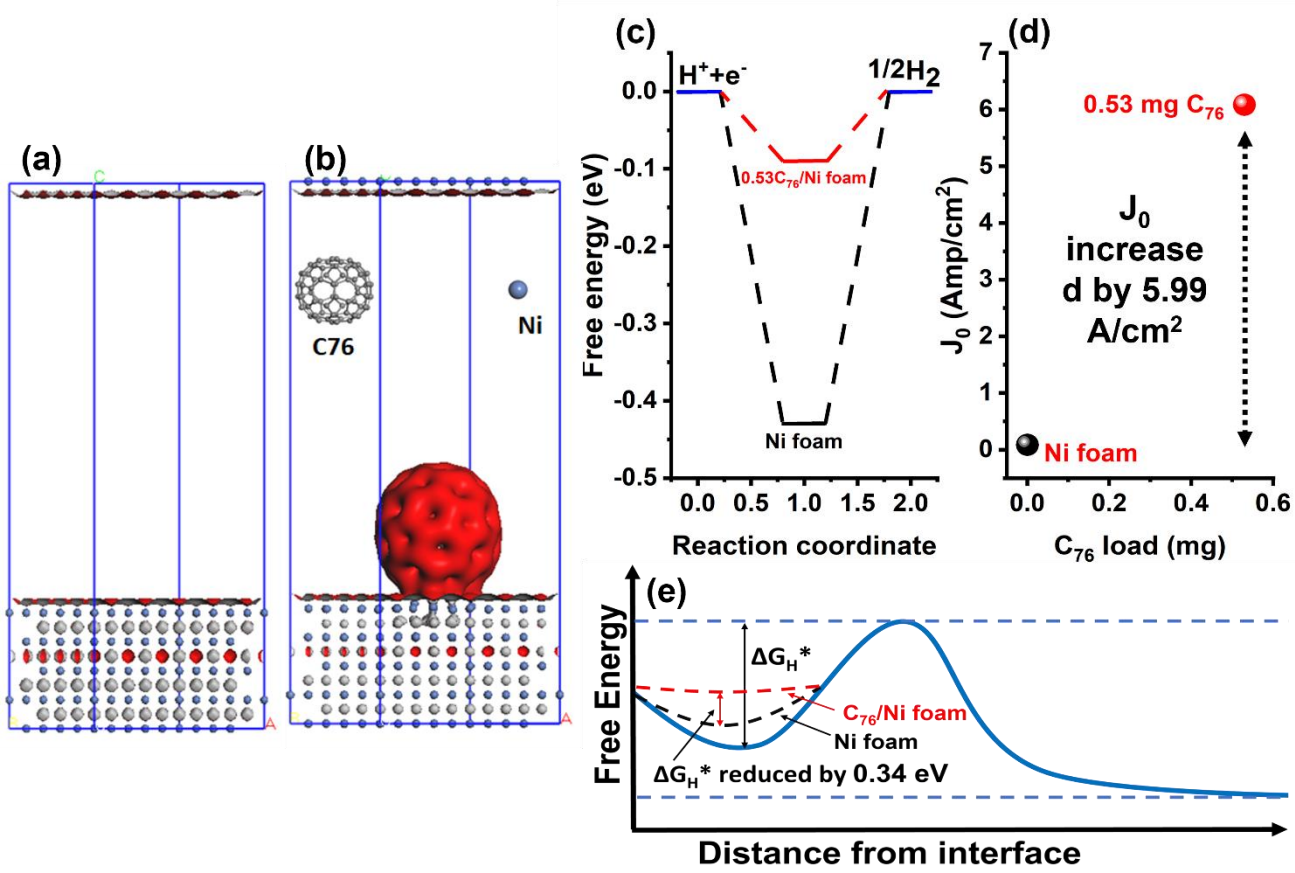

Figure 37. (a) Free energy changes (ΔG_H^*) of H adsorption on Ni foam and C_{76}-coated Ni foam, (b) the corresponding increase in J_0, (c) a schematic diagram illustrating the reduction in the size of the activation barrier upon the use of C_{76}/Ni foam composite, and (d,e) the electron density distribution in the absence and presence of C_{76}.

7.5 Conclusion

The electronic structure of the commercially available fullerenes (C_{60}, C_{70}, C_{76}, C_{84}, C_{100}) was calculated to identify the best candidate for electrocatalysis. The calculations revealed C_{76} as the most electrically conducting candidate with the lowest bandgap energy. Therefore, the synergy between C_{76} and Ni foam substrate was explored both theoretically and experimentally

for the HER. The DFT calculations showed that the combination of C_{76} and Ni resulted in a drastic decrease in the free energy compared to bare C_{76} or bare nickel foam. The electron density difference (EDD) calculations showed charge redistribution at the C76/Ni interface, where the electron density increased on fullerene and decreased on nickel, indicating the synergy between C_{76} and Ni foam in allowing electron transfer from nickel to C_{76} and acting as a superior bifunctional catalyst. The C_{76}/Ni catalyst showed an HER overpotential of 20 mV vs. RHE at -10 mA cm^{-2}, which is almost the same as that of the benchmark Pt/C catalyst. The DFT calculations showed that Ni lowers the activation barrier, with the reduction in the activation barrier was much higher (0.34 eV) for the combination C_{76}/Ni than bare Ni or C_{76}. The electrochemical kinetics results are in agreement with the DFT findings. The electrodes with the lowest activation barrier were the ones that showed the lowest overpotential and the highest α and J_0, indicating fast kinetics. Lastly, the correlation between the activation barrier and $J_0$was explained in detail. Thus, this study unveiled the superior HER catalytic activity of C_{76}/Ni foam.

Chapter 8 Results and discussion

Compositionally Variant Bifunctional Tetrametallic Ni-Co-Mn-Fe Phosphide Electrocatalysts for High-Performance Overall Water Splitting

8.1 Morphology

The electrodeposition of the catalysts takes place directly on the conductive substrate. Figure 38 depicts the morphology of the different electrodeposited composites fabricated using cyclic voltammetry technique solely, while Figure 39 shows the structure formed after applying galvanostatic electrophosphidation accompanied with hydrogen evolution, revealing the formation of nanosheets-like structure in both cases. For the composites prepared via cyclic voltammetry, the growth of the nanosheets was uniform over the entire substrate, which can be attributed to the low current density during the electrodeposition process, as elaborated in Figure 40. Note that the maximum current reached during the CV cycles is 6 mA, which is not sufficient for HER to take place and disturb the morphology of the deposited nanosheets.

Upon phosphidation, the roughness of the formed structures increased, along with the transformation of the nanosheets into 3D porous nanospheres made of compact nanosheets, Figure 39. As the electrodeposition of the P-based nanosheets is performed at -200 mA, the deposition process is competing with the HER, as expected, and noticed by naked eye. Nevertheless, the bubbles formed during the HER play a crucial role in the formation of those 3D porous nanospheres. The bubbles formed on the Ti mesh substrate block some of the active sites of the substrate, allowing less number of available sites for deposition of the dissolved ions. Thus, the growth of the nanosheets can only take place at the interstitial distance between the formed bubbles and enforcing the deposited nanosheets growth into nanospheres. Furthermore, the newly deposited nanosheets present new active sites for bubble formation, resulting in the development of pores within the formed nanospheres.[207–209] This also explains the reduction in the recorded potential over the deposition time for the P-based composites, as demonstrated in Figure 40b. This comes in agreement with the previously reported morphology obtained for MnO_2 nanosheets, where the formed

MnO_2 nanosheets were compacted due to the rapid formation of the nanosheets structure.[210] This change in morphology upon phosphidation is expected to increase the surface area and provide more active sites for the intended reactions to take place. Moreover, the 2D structure of the formed nanosheets should enhance the charge transfer during their use as electrocatalysts.

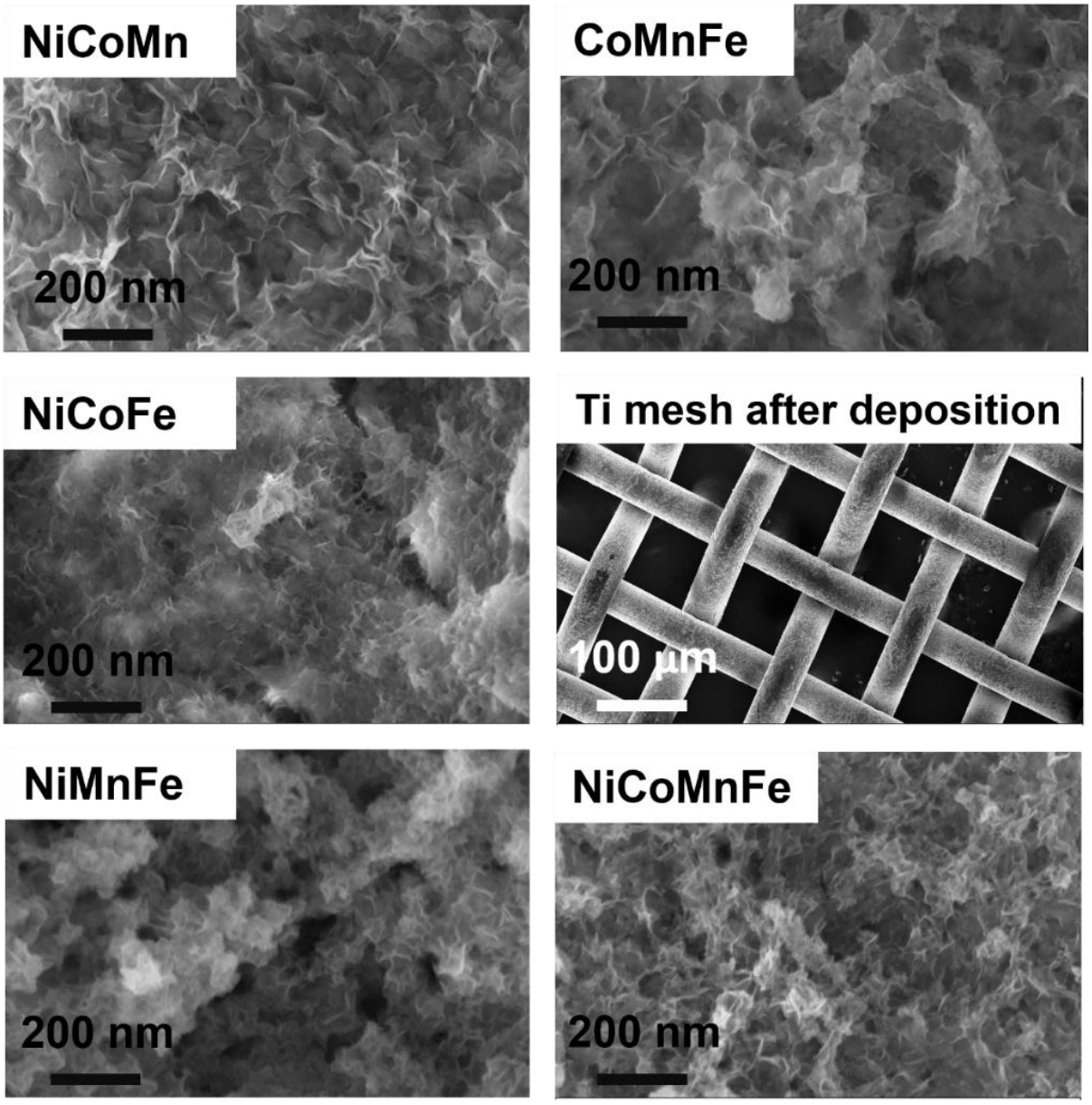

Figure 38. FESEM images of the electrodeposited films with different composites prior to phosphidation.

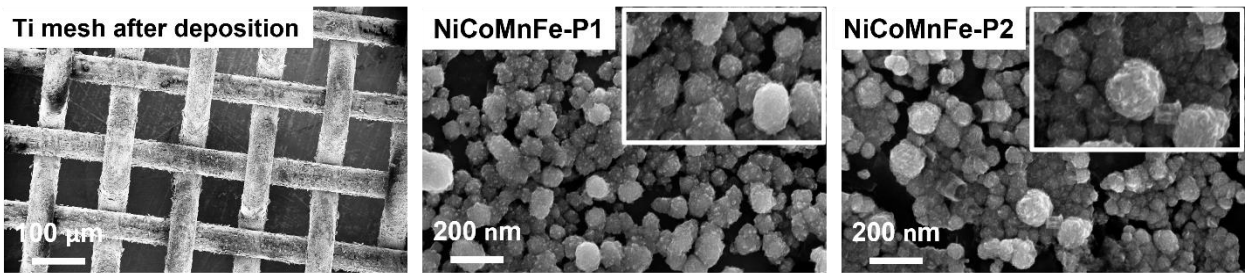

Figure 39. FESEM images of the films after phosphidation.

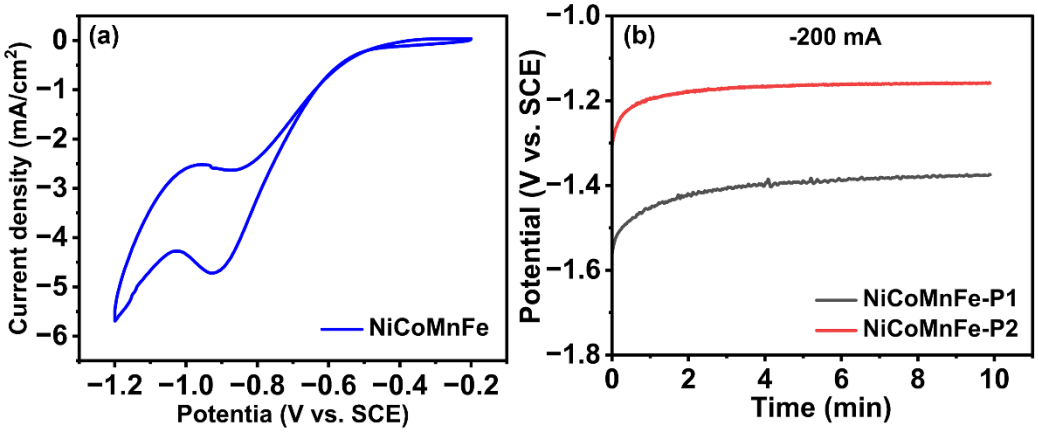

Figure 40. (a) and (b) Potential response and current response during electrodeposition for NiCoMnFe and NiCoMnFe-P based nanosheets.

8.2 Structural characterization

XRD and XPS analysis

To elucidate the crystallinity and the phase of the various fabricated materials, the x-ray diffraction (XRD) spectra of the catalysts supported on Ti mesh were recorded as depicted in Figure 41. The spectra of NiCoFe-O/Ti, NiCoMn/Ti, NiMnFe/Ti, MnCoFe/Ti, NiCoMnFe/Ti films are compared to those of the phosphide-treated NiCoMnFe-P1 and NiCoMnFe-P2 films. The spectra reveal significant diffraction peaks at ~35.0°, 38.4°, 40.1°, 53.0°, 62.9°, 70.6°,76.3°, and 77.3° that can properly be ascribed to the (100), (002), (101), (102), (110), (112), and (201), plans of the Ti substrate, respectively (ICDD: 00-005-0682).

Before phosphidation, the deposited catalysts containing Ni and Co precursors showed characteristic peaks at ~ 38.4°, and 75.3° that can be indexed to the crystalline cubic $NiCo_2O_4$ phase

with the corresponding lattice planes of (311), and (533), respectively (ICDD: 00-020-0781). It should be noted that no characteristic diffraction peaks of manganese oxide and iron oxide species were detected in the XRD profiles, which could be attributed to the amorphous nature of the manganese and iron oxide films.[211] In case of the deposited NiCoMnFe/Ti catalyst, while mixing all metal precursors, the characteristic peaks of the corresponding cubic $NiCo_2O_4$ phase have only appeared prominently, confirming the amorphous nature of the deposited structure. Note that amorphous materials could be more electroactive catalysts owing to the larger density of coordinative unsaturated sites, promoting the adsorption of reactants compared to the crystalline catalysts counterparts.[212] The unnoticeable change of the NiCoMnFe/Ti crystal structure upon the addition of Fe/ Mn might be ascribed to the similar atomic radius of Co, Ni, Mn, and Fe. Thus, Fe and Mn could be easily incorporated into the NiCo-O lattice, replacing parts of Ni and Co and creating substitutional lattice defects.[213,214] To some extent, these lattice defects could promote the OER performance by boosting extra active sites.[213,215]

Upon phosphidation, sharp and highly intense peaks can be distinguished for the NiCOMnFe-P1 and NiCoMnFe-P2 films at approximately 40.9°, which is believed to result from the crystalline pattern of the (111) crystalline plane of hexagonal NiCo-P (ICDD: 01-071-2336). Furthermore, the two observed peaks at ~ 38.4°and 40.8° could be well indexed to the (220) and (112) planes of the cubic Ni2P (JCPDS 74-1385). Due to the partial replacement of Ni ions with Co ions, the pristine crystal structure did not change, thus NiCo-P overlapped and almost showed the same diffraction patterns as Ni2P. Notably, the XRD pattern of the deposited phosphide catalysts showed a slight shift in the peak position relative to the reference standard cards of hexagonal NiCo-P and cubic Ni2P. This might be attributed to the incorporation of Fe and Mn atoms within the lattice structure. Accordingly, these results could reveal the successful formation of the phosphide catalysts intentionally upon phosphorus incorporation.

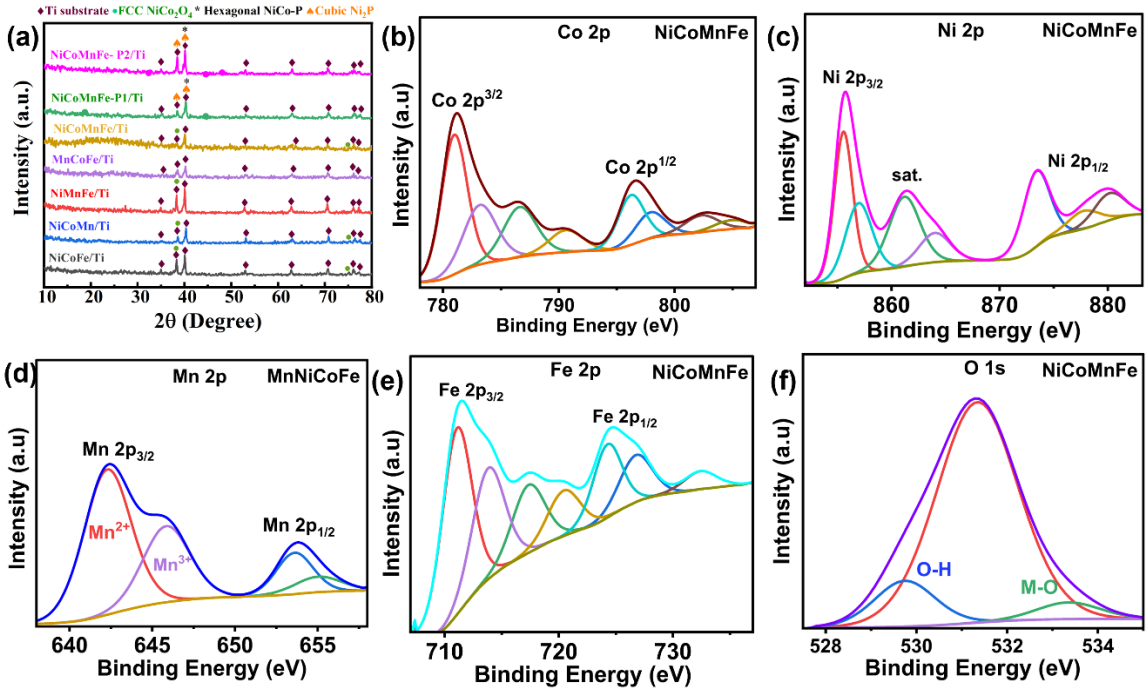

Figure 41. (a) XRD patterns of the different electrodeposited composites on Ti mesh and (b-f) the high resolution XPS Ni 2p, Co 2p, Mn 2P, Fe 2p, and O 1s spectra, respectively for the NiCoMnFe catalyst.

As the reaction takes place at the electrode surface, surface analysis is essential to understand the catalytic activity of the different active sites present on the surface. As the reduction potential of Mn, Co, Ni, and Fe ions are -1.145V, -0.745 V, -0.8 V, -0.616 V vs SCE,[216,217] the applied potential range is expected to be sufficient for all these metal ions to be reduced and deposited on Ti mesh. Figure 46 demonstrates the survey scan of the deposited nanosheets. The spectrum confirms the presence of Ni, Co, Mn, Fe, P, and O.

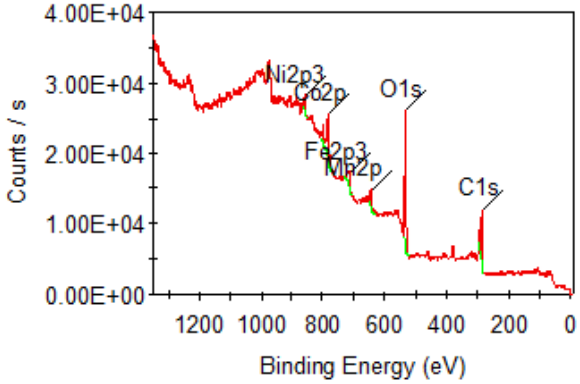

Figure 42. XPS survey scan of NiCoMnFe-P composites

The high-resolution XPS spectra of the NiCoMnFe nanosheets is illustrated in Figure 41 and Figure 43 depicts the XPS spectra of the phosphide-based composites before and after electrochemical measurements.

For the Co 2p spectrum, the peaks recorded at 781.2 eV (Co $2p^{1/2}$) of Co^{2+}, 796.6 eV (Co $2p^{3/2}$) of Co^{3+},[218] and the two shakeup peaks at 783.6 eV and 802 eV belong to Co-P, while the peak at 780.7 eV defines the oxidation of Co and P forming Co-PO_x.[217,219–221] This indicates that the formed cobalt phosphide was partially oxidized during electrodeposition, facilitating the attachment of the formed nanosheets to the substrate.[222] along with the unavoidable oxidation due to exposure to air.[223]

As for the Ni spectrum, the peaks recorded at 856.2 eV and 878 indicate the presence of Ni^{2+} species Ni $2p^{3/2}$ and Ni $2p^{1/2}$, respectively.[224] Besides, the two peaks characteristic of oxidized nickel phosphide (Ni-PO_x) were observed at 873.2 eV ($2p_{1/2}$) and 856.2 eV ($2p_{3/2}$).[225]

The manganese spectrum showed that the dominant phase formed is Mn^{3+} ($2p_{3/2}$), as indicated by the peak with the highest intensity at 642.7eV. [226,227] Note that a small peak related to Mn^{2+} was also observed after deconvolution at 640 eV, along with the characteristic satellite signal of Mn^{2+} at 646.5 eV.[226,227]

The Fe 2p spectrum showed two peaks at 711.9 eV and 722 eV,[228] with the peak at 714 eV attributed to the oxidized Fe-P.[229,229] The O 1s spectrum presented the metal-oxygen bond, and O-H bond, with the signals recorded at 531.6 eV and 532.7 eV. The observed peak broadening is due to the incorporation of P atom into the lattice.

Finally, the P spectrum confirmed the incorporation of P into the deposited composite for both NiCoMnFe-P1 and NiCoMnFe-P2, as determined from the characteristic peak at 133.6 eV, Figure 43.[230] All the aforementioned XPS data along with the SEM images confirm the deposition of all targeted metals on the Ti mesh forming NiCoMnFe and NiCoMnFe-P nanosheets. As the phosphorus species have one free electron, it is negatively charged, thus it should attract the positively charged protons and facilitates the reduction of H^+ ions to H_2.

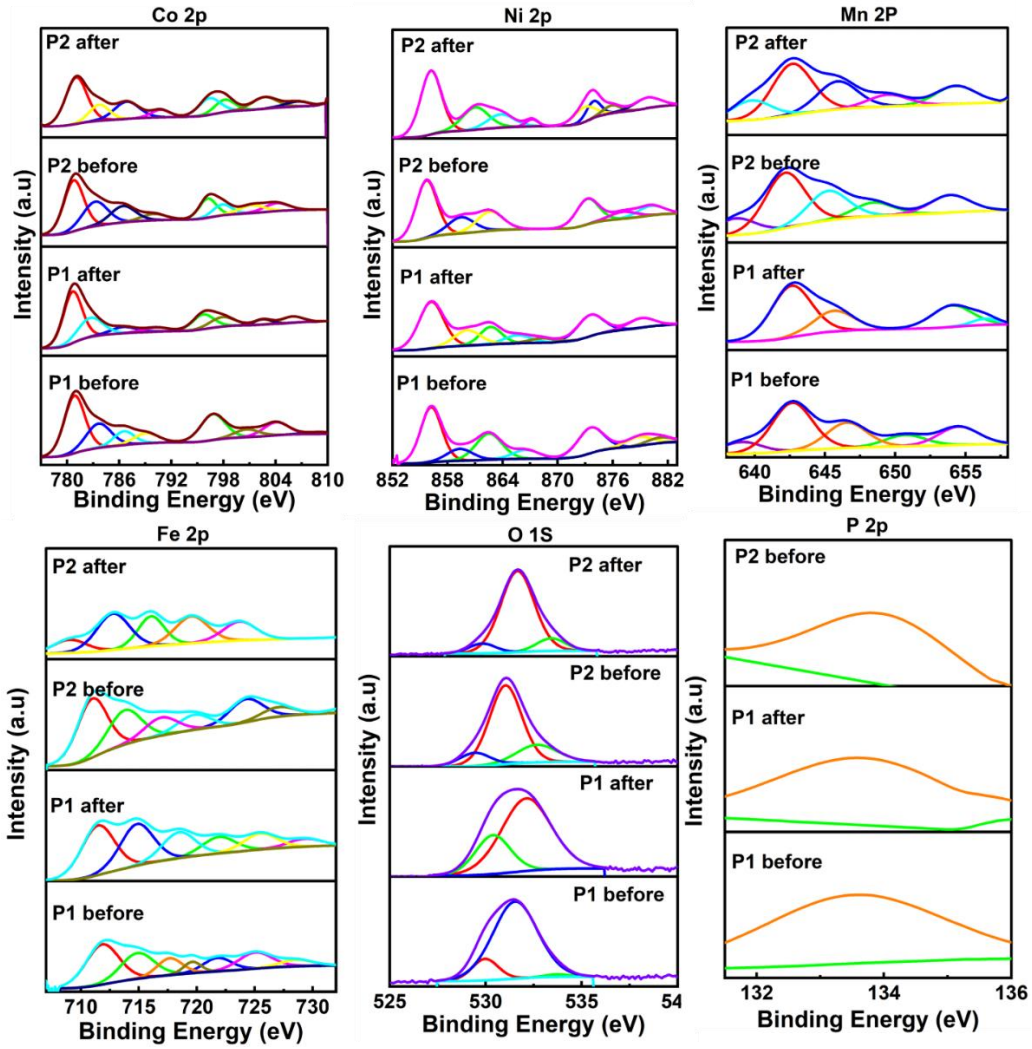

Figure 43. High resolution Ni 2p, Co 2p, Mn 2P, Fe 2p, P 2p, and O 1s XPS spectrum of the NiCoMnFe-P catalysts before and after electrochemical testing

8.3 Electrocatalytic Hydrogen Evolution Reaction (HER)

As the aim of this study is to investigate the catalytic activity of the electrodeposited nanosheets without interference from the chosen substrate, the HER catalytic activity of Ni foam, the most widely used substrate in catalysis, was elucidated and compared to that of commercial Ti mesh. As shown in Figure 44, Ni foam exhibits very low overpotential compared to Ti mesh. Ni foam reduces the overpotential by more than half the value needed for Ti mesh to achieve a current density of -10 mA/cm^2. Accordingly, we decided to use Ti mesh to reduce the interference from the substrate to the recorded measurements and to avoid any misleading merits of the catalyst itself.

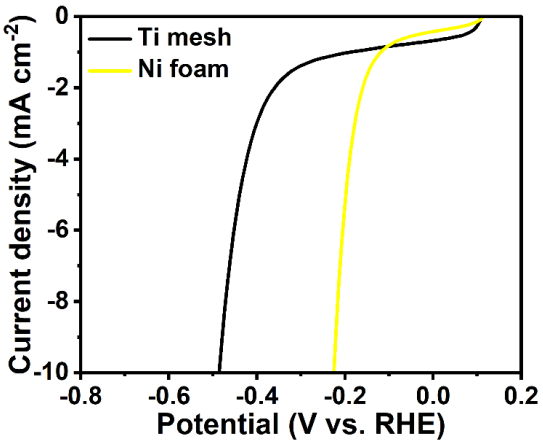

Figure 44. HER polarization curve for Ti mesh and Ni foam substrates.

The catalytic activity of Ti mesh, NiMnFe, MnCoFe, NiCoMn, NiCoFe, and NiCoMnFe were first explored to determine the optimum composite, which exhibits the lowest overpotential. Then, to explore the effect of phosphidation on the electrocatalytic activity, the LSV spectra of NiCoMnFe-P1 and NiCoMnFe-P2 were recorded, Figure 46. While bare Ti mesh exhibits an overpotential of 486.57 mV, the composites NiCoMnFe and NiCoFe showed the lowest overpotentials among the tested materials. However, the NiCoMnFe catalyst reveals the lowest overpotential of 300.5 mV vs. RHE at -10 mA/cm², Figure 46a. Table 3 lists the overpotentials recorded for all catalysts under investigation at a current density of -10 mA/cm². Figure 45 reveals the NiCoMnFe composite to have the lowest overpotential at -10 mA. Thus, this composite was chosen to study the effect of phosphidation on the catalytic activity.

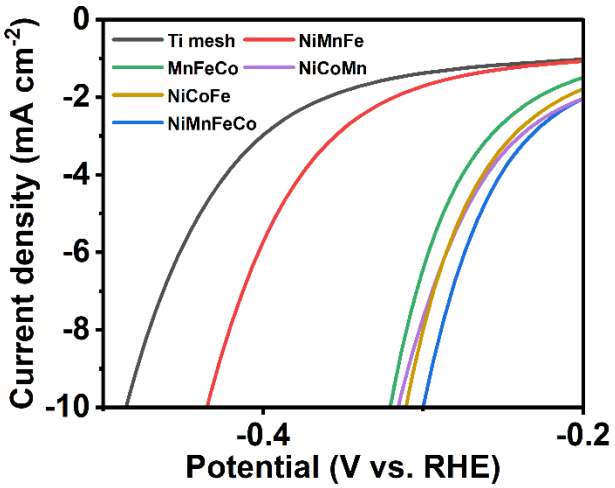

Figure 45. HER polarization curve for the fabricated composites at –10 mA.

Note that the phosphide catalysts showed much lower overpotentials of 239 and 200 mV/cm^2 for the NiCoMnFe-P1 and NiCoMnFe-P2 catalysts, respectively. This means that we were able to reduce the required overpotential needed to drive the HER reaction by more than 42 % upon the use of phosphidized catalysts compared to bare Ti mesh. This extraordinary enhancement of the electrocatalytic activity can be ascribed to the synergistic effect between the four metals (Ni, Co, Mn, Fe) along with the presence of the phosphorous ions that facilitate fast charge transfer and feasibility of intermediate adsorption on the active sites, ensuring faster kinetics.

To further confirm the effect of the unique electronic properties of this catalyst on the kinetics of the HER reaction, Tafel slope was calculated for all the fabricated catalysts, see Figure 46b. The two catalysts containing phosphorous showed the lowest Tafel slopes, indicating faster reaction kinetics. Moreover, the charge transfer resistance (R_{CT}) was estimated from the electrochemical impedance spectroscopy (EIS) analysis conducted at -1.5 V. The equivalent Randle's circuit was used to fit the semicircles and extract the R_{CT} (inset Figure 46c). The EIS Nyquist plot analysis revealed that both phosphorus-based catalysts exhibit the smallest semicircles compared to the other materials. Consequently, they showed the lowest R_{CT} of 0.379 Ω and 0.463 Ω for P1 and P2 catalysts, respectively. This confirms that the presence of P ion enhances the interfacial charge transfer between the deposited composite, the substrate, and the electrolyte. Hence, reducing the resistance and accordingly enhancing the interaction at the electrode/electrolyte interface. This effective charge transfer leads to ultrafast Faradaic reactions and faster reaction kinetics.[231,232]

The turnover frequency (TOF), which represents the amount of H_2 evolved/active site was calculated at different overpotentials to inspect the catalytic activity of the phosphorous-based composites, as shown in Figure 46d. While the TOF of P1 at -0.3 V was 1.18 S^{-1}, it was almost twice 2 S^{-1} for P2.[232,233] Finally, the durability and endurance of the phosphorous-based composites were tested via stability test, where a constant current of -10 mA was applied for 16 hours and the change in overpotential over time was observed. As shown in Figure 46e, both P-composites maintained almost the same overpotential along the 16 hours, with a slight increase in the recorded overpotential (almost 4% after 16 hours) for the composite P2. This prevails the

robustness of the fabricated electrocatalysts and their potential for use in large scale systems.

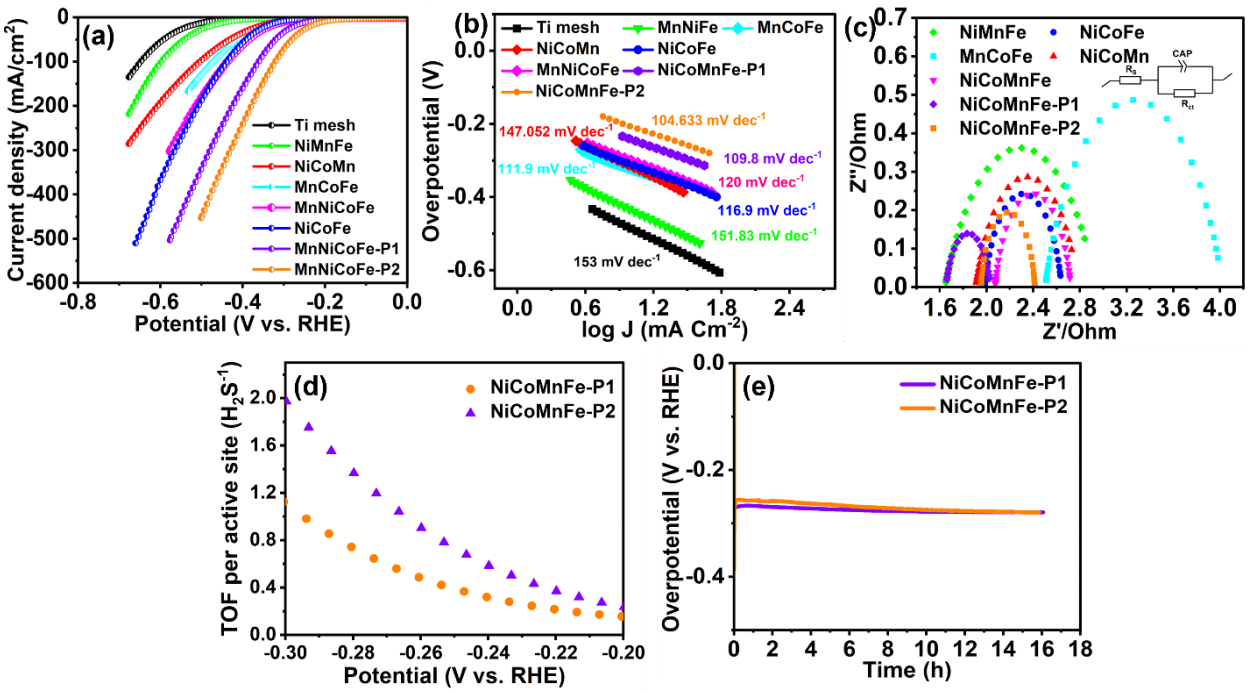

Figure 46. HER performance of the fabricated electrocatalysts measured in 1 M KOH. (a) IR-corrected LSV polarization curves, (b) the corresponding Tafel slopes for the electrocatalysts under study, (c) EIS Nyquist plots, (d) Turnover frequency of the phosphide samples with the highest catalytic activity, and (e) the stability test performed for the phosphide catalysts.

Table 3. The overpotentials and the R_{CT} values recorded for all fabricated catalysts for HER and OER

Catalyst	HER overpotential at -10 mA/ cm² (mV vs RHE)	HER R_{CT} (Ω)	OER overpotential at 10 mA/cm² (mV vs RHE)	OER R_{CT} (Ω)
NiCoFe	310.26	0.66	290.24	0.613
NiCoMn	315.73	0.878	334.69	2.492
MnCoFe	320.35	1.523	343.23	2.037
CoNiMnFe	300.58	0.648	279.823	0.6
NiMnFe	434.97	1.292	306.71	0.65

Ti mesh	486.57	-	534.543	-
NiCoMnFe-P1	239	0.379	-	-
NiCoMnFe-P2	200	0.463	-	-

8.4 Electrocatalytic Oxygen Evolution Reaction (OER)

The catalytic activity of the fabricated composites toward OER was tested using the same setup used for HER with 85% IR correction, Figure 48. At a current density of 10 mA/cm^2, the bare Ti mesh showed an OER overpotential of 534.5 mV, while the catalysts showed lower overpotentials, Figure 6a. The NiCoMnFe catalyst showed the lowest overpotential (279.8 mV), with a 32% reduction in the overpotential compared to that of bare Ti mesh. This reveals the unique properties of the catalyst resulting from the interaction between the four metals that facilitates the OER. The obtained overpotential is superior to those recently reported in the literature for transition metals-based catalysts, as illustrated in Table 4. The anodic shoulder observed around 1.2 to 1.4 V vs. RHE is attributed to the presence of Co and Ni.[234,235] As observed form the LSV polarization curves, this shoulder appears at a lower potential for the best two samples (NiCoMnFe and NiCoFe), suggesting a change in the electronic structure during the electrodeposition of these two catalysts compared to the others. This change in the electronic structure is expected to lower the free energy of the OER,[236] which comes in agreement with the low overpotentials recorded for these two electrocatalysts. We expect that this modification in the electronic structure is attributed to the synergism between the four deposited metals, resulting in facilitating OER kinetics and allowing faster charge transfer kinetics.[235,237] Interestingly, when P was incorporated to the electrocatalyst that showed the best catalytic activity (NiCoMnFe), the potential needed to drive the OER increased, see Figure 47.

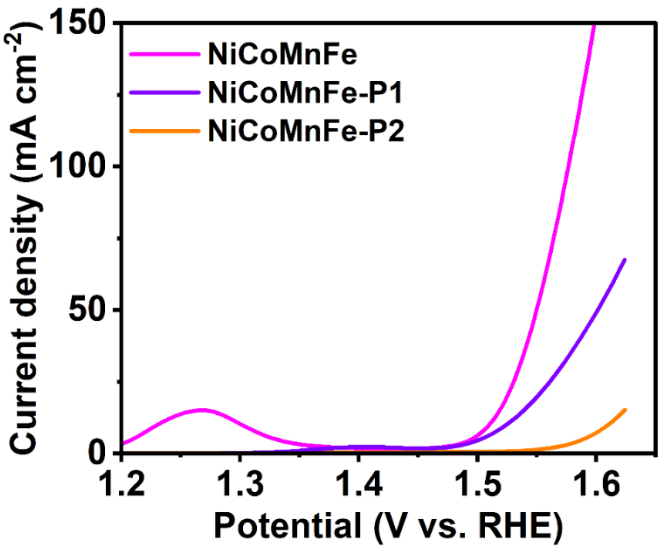

Figure 47. OER polarization curve of NiCoMnFe, NiCoMnFe-P1, and NiCoMnFe-P2.

This was confirmed by the DFT calculations that reveal much higher energy barrier for OER in the presence of P, leading to sluggish kinetics and higher overpotentials, see the DFT section for more details. The kinetics of the reaction was further assessed by calculating the Tafel slopes from the corresponding LSV graphs, see Figure 48b. The composite NiCoMnFe exhibits the lowest Tafel slope (53.1 mV dec^{-1}), confirming faster and higher rate of charge transfer kinetics for this electrocatalyst due to the optimum lattice formed by Ni, Co, Mn, and Fe metals. The active sites provided by these metal cations favors the adsorption of OH^- group, lowering the activation barrier of the oxygen evolution reaction and consequently reducing the overpotential needed to drive the OER. As charge transfer is a crucial indication of the catalytic activity of any catalyst, the EIS measurements were conducted at 0.7 V to study the effect of the composition of the fabricated electrocatalysts on the charge transfer kinetics.

The R_{CT} of each catalyst was extracted after fitting the corresponding Nyquist plot using the equivalent circuit shown as an inset in Figure 48c. The smallest semicircle and the lowest R_{CT} were recorded for the NiCoMnFe electrocatalyst (0.6Ω), reflecting fast reaction kinetics at the electrode/electrolyte interface and confirming the effect of the unique electronic properties of this composite. Upon identifying the composite that demonstrated the highest OER catalytic activity with the lowest overpotential, the turnover frequency of this electrocatalyst was calculated at different overpotentials to get a quantitative perception of the amount of oxygen evolved per active site of this catalyst. The NiCoMnFe electrocatalyst showed a TOF of 0.32 S^{-1} at 350 mV,

reflecting high rate of oxygen evolution, where the generated charge is mostly consumed in the OER eliminating other side reactions, Figure 6d. Lastly, the stability of this outstanding catalyst (NiCoMnFe) in OER was examined by applying a constant current density of 10 mA/cm^2 and monitoring the change in the recorded overpotential for 17 hours, Figure 48e. The catalyst showed exceptional stability, maintaining the same overpotential. This indicates that the fabricated electrocatalyst exhibits high tolerance over long periods of time, making it a very suitable candidate for industrial scale OER.

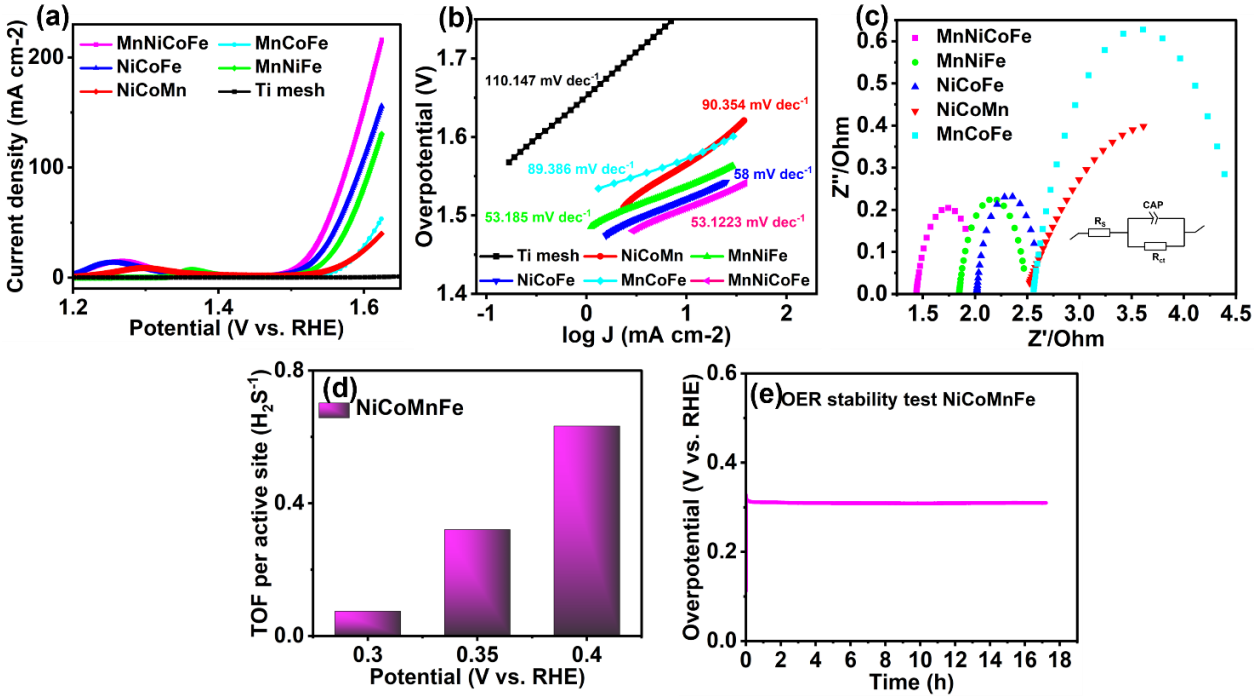

Figure 48. OER activity of the fabricated catalysts measured in 1 M KOH. (a) IR-corrected LSV polarization curves, (b) the corresponding Tafel slopes of the electrocatalysts under investigation, (c) EIS Nyquist plots, (d) Turnover frequency of the NiCoMnFe nanosheets, and (e) the stability test performed using chronopotentiometry technique for the NiCoMnFe nanosheets.

Table 4. Comparison of the estimated OER overpotential with those reported in the literature.

Catalyst	OER overpotential (mV/cm^2)	Tafel slope (mV dec^{-1})	Ref.
This work	279 @10	53.1	
Co–Mn carbonate hydroxide	294@30	-	81
Co–P film	345@10	47	82

Ni_2P	290@10	47	83
Ni–P film	344@10	49	84
Fe–Co composite films	283@10	34	85
P–Co_3O_4	280@10	51.6	86

8.5 Electrocatalytic Overall Water Splitting

Upon identifying the best catalysts for HER and OER among the tested electrocatalysts, an overall water splitting electrolyzer was constructed, where NiCoMnFe composite was used at one side, while NiCoMnFe-P1 or NiCoMnFe-P2 was used as other electrode immersed in 1 M KOH aqueous electrolyte in a two-electrode cell. Figure 49 demonstrates the difference in the recorded polarization curves of the potential of the overall device upon changing the source of the phosphorous used in the electrodeposition step. As reflected from the obtained data, at a current density of 10 mA/cm^2, when the composite NiCoMnFe-P1 was used, the obtained cell voltage was 1.88 V. On the other hand, upon the use of NiCoMnFe-P2, the cell voltage was significantly reduced to 1.71 V. This value is very close to the benchmark electrolyzer composed of Pt/C || RuO_2, which needs a cell voltage of 1.56 V to generate a current density of 10 mA/cm^2.[238]

As shown in Figure 49b, we performed a long-term stability test to examine the tolerance of the assembled electrolyzers under rigorous conditions. The chronoamperometric test was performed for 20 hours at 1.88 and 1.71 V for NiCoMnFe-P1 and NiCoMnFe-P2 electrodes, respectively. Interestingly, although NiCoMnFe-P2 exhibits lower overpotential, NiCoMnFe-P1 shows higher stability over the operating time. This might be attributed to the higher rate of P dissolution in NiCoMnF-P2 [67] compared to the higher ability of NiCoMnF-P1 to preserve the P species. The XPS spectra of the catalysts after measurements were collected and analyzed, Figure 4. The P species were still present after electrochemical measurements for the composite NiCoMnFe-P1, while no signal of P species was found for NiCoMnFe-P2, which explains the faster decay rate of NiCoMnFe-P2 relative to NiCoMnFe-P1 in the stability test.

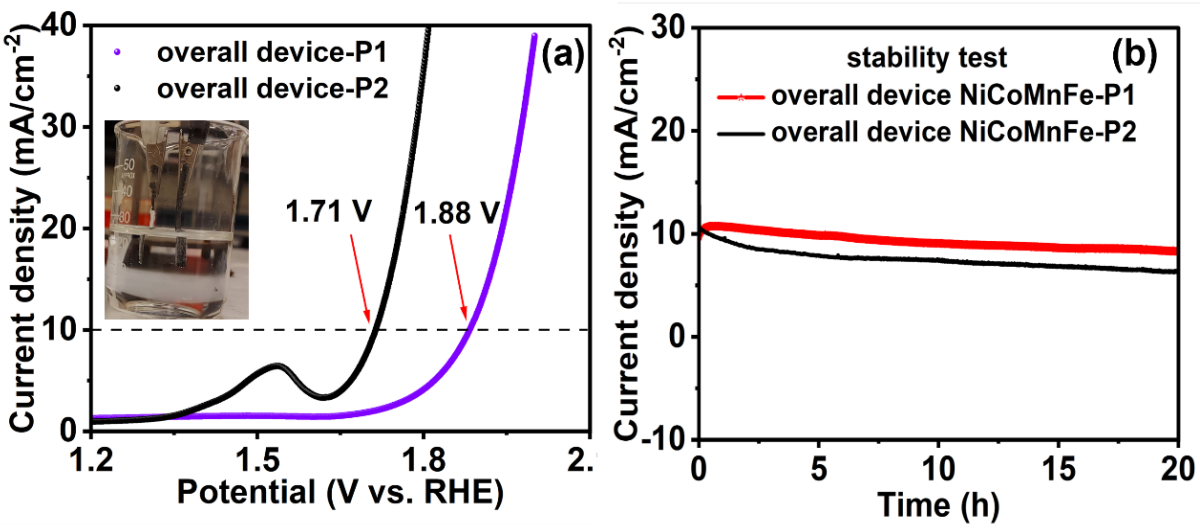

Figure 49. The overall water splitting electrolyzer used to demonstrate the electrochemical performances of NiCoMnFe and NiCoMnFE-P1/P2 in 1 M KOH. The inset is a photograph of the setup used during HER and OER overall reaction using a two-electrode setup. (a) IR-corrected LSV polarization curves, (b) durability test of the overall water splitting electrolyzer, performed using steady-state chronopotentiometry for 20 hours.

8.6 DFT results and discussion

Density function theory (DFT) calculations were performed to unveil the influence of combining the four metals (Mn, Fe, Co, and Ni) with and without phosphide on the overall water splitting activity, as depicted in Figure 50.

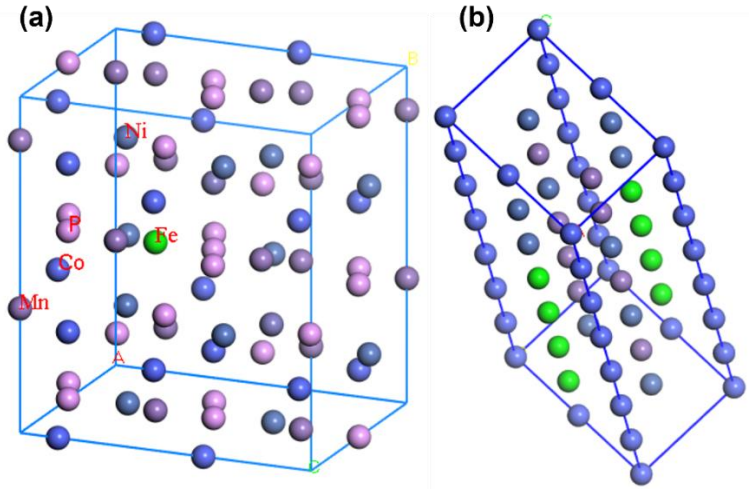

Figure 50. Geometry optimized figures of (a) MnFeNiCo-P (b) MnFeCoNi

Both HER and OER were investigated via studying the surface adsorption energy for the different possible sites. The HER route is represented by three steps starting with adsorption of water molecule, then cleavage of H-O bond (Volmer step), followed by combination with another water molecule, then desorption of hydrogen molecule via Heyrovsky or Tafel mechanism. For alkaline medium, there are two important descriptors for HER activity, namely ΔG_H and ΔG_{H2O}. The excellent HER activity for MnFeCoNi-P arose from the availability of different active sites. As shown in Figure 51a, the ΔG_H for the top site on P, Ni, Fe, Mn, and Co were found to be -0.31, -0.48, -0.67, -1.79, and -2.00, respectively. The top of the P site is the best site for HER as it has the closest value to the ideal value $\Delta G_H = 0$, in agreement with the literature.[158] Also, ΔG_{H2O} on top P site is -0.298 eV, which facilitates the H-OH bond cleavage, yielding H* intermediate. The values of the two descriptors ΔG_H and ΔG_{H2O} explain the efficient electrocatalytic activity of MnFeCoNi-P towards HER.

For further insights into the overall performance, the activity of OER was investigated. The OER consists of four one-electron steps as explained in chapter 4, with each step expressed by Gibbs free energy. As demonstrated in Figure 51b, the rate determining step for OER on MnFeCoNi (311) is the HOO^* formation, denoted as $\Delta G3$. Based on the obtained values of the free energies listed in Table 5, the energy barrier of the rate determining step was calculated according to the values of $\Delta G2$ and $\Delta G3$ of each composite, accordingly, we found that the energy barrier was higher for MnFeCoNi-P (3.84 eV), compared to NiCoMnFe (1.69 eV). Hence, this difference in free energy resulted in increasing the energy barrier of the rate limiting step in presence of P species, this may interpret the reason why MnFeCoNi exhibits higher catalytic activity for OER than MnFeCoNi-P, in agreement with the results obtained from the electrochemical measurements.

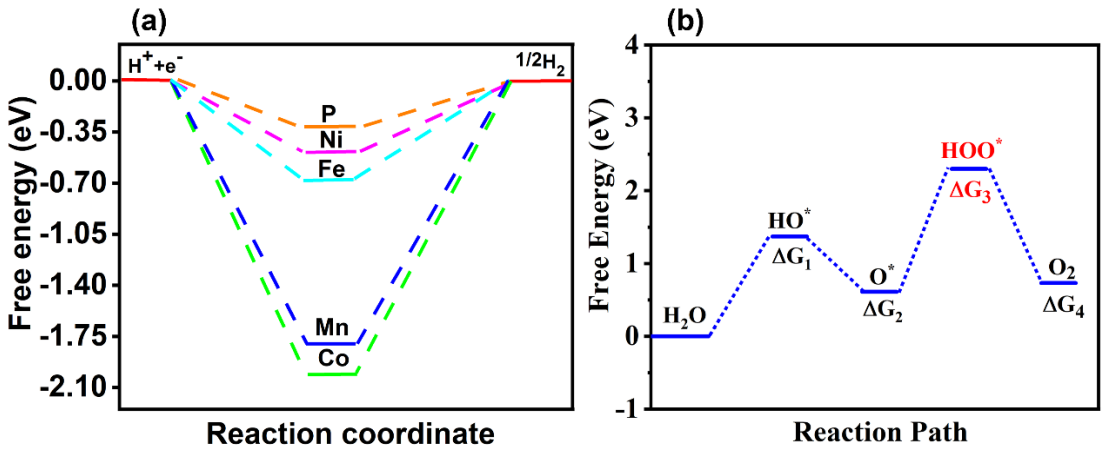

Figure 51. (a) The free energy diagram for HER on P-top site of MnFeCoNi-P (111) and (b) The corresponding free energy diagram for OER on Ni-top site of MnFeCoNi (311).

Table 5 Calculated Gibbs free energy for MnFeCoNiP and MnFeCoNi during OER.

	ΔG1	ΔG2	ΔG3	ΔG4
MnFeCoNi	1.37	0.61	2.3	0.73
MnFeCoNiP	1.62	-0.57	3.27	2.43

8.7 Conclusion:

This study unveiled the optimal interfacial synergy of electrochemically deposited tetrametallic Mn-Fe-Co-Ni phosphide electrocatalysts for overall water splitting. The effect of the different phosphide precursors on the morphological, composition, and electrochemical activity of the prepared catalysts was elucidated in detail. The fabricated transition metals-based nanosheets showed excellent catalytic activity as bifunctional electrocatalysts for both HER and OER. Both DFT calculations and experimental results proved the superior HER activity of the tetrametallic MnFeCoNiP catalyst and excellent OER activity of the MnFeCoNi catalyst in alkaline solution. The catalysts showed high tolerance and durability, suggesting their potential for overall water electrolysis on industrial scale.

Chapter 9

Conclusion and Future Work

9.1 Conclusions

As discussed in previous chapters of this dissertation, water electrolysis is intensively studied as a promising and facile technique for hydrogen gas production. Hydrogen gas is as an alternative clean, renewable, and sustainable source of energy. In the first part of the dissertation, the stability of various counter electrodes was explored, after proving that the dissolution of the counter electrode and the redeposition of the dissolved ions on the working electrode can lead to deceptive enhancement in the catalytic activity under investigation. In this regard, Ti mesh was introduced as a low dissolution material that can be used as a counter electrode that does not interfere with the recorded measurements.

For the rest of the dissertation, different nanostructured materials were fabricated and examined as electrocatalysts for water splitting. First, boron carbon nitride-copper nanosheets, a 2D-carbon based nanostructure, were synthesized via a novel methodology and their catalytic activity for HER in acidic medium was investigated. The optimum load of copper nanoparticles was found to significantly reduce the needed overpotential. Then, C_{76}, a 0D-carbon based nanostructure loaded over nickel foam, was examined as an electrocatalyst for HER in acidic medium. Upon studying the kinetics of the reaction, we found that the interfacial interactions between C_{76} and Ni foam results in a remarkable reduction in the recorded overpotential and the highest α and J_0, indicating fast kinetics. Thus, the synergy between C_{76} and nickel foam substrate was found to significantly enhance the catalytic activity towards HER. Finally, different combinations of the transition metals Ni, Co, Mn, and Fe were synthesized in the form of nanosheets via the electrodeposition technique. The activity of the fabricated composites was investigated for both HER and OER in alkaline medium. Upon identifying the optimum electrode for each reaction,

the catalyst with the lowest overpotential was modified via electro-phosphidation, and the effect of phosphorous incorporation on the catalytic activity of HER was thoroughly studied. According to the obtained results, the introduced transition metals-based nanosheets showed excellent catalytic activity as bifunctional electrocatalysts for HER and OER, with high tolerance and durability, making them promising candidates for overall water electrolysis on industrial scale.

9.2 Future work

Hopefully, the work presented in this dissertation opens the door for possible future research. Below are some suggestions research points to extend the work done in this dissertation.

- Creating a protocol that allows careful investigation of the dissolution of any of the components used in the electrolysis setup.
- Applying the proposed electrospinning-based technique to fabricate other nanostructured 2D-materials.
- Optimize the parameters affecting electrochemical exfoliation.
- Fabricate new fullerene structures with higher number of carbon atoms than the commercially available now and test their catalytic activity.
- Exploring new approaches to fabricate self-assembled nanostructured electrocatalysts.
- Investigating the effect of the different methodologies used in electrodeposition technique on the morphology and the charge transfer across the fabricated electrodes.
- Investigating the catalytic activity of single atom transition metal-based catalyst.

9.3 Published work out of this dissertation

1- Hasan, M. M.; Khedr, G. E.; Allam, N. K. Compositionally Variant Bifunctional Tetrametallic Ni-Co-Mn-Fe Phosphide Electrocatalysts for High-Performance Overall Water Splitting. Under review

2- Hasan, M. M.; Khedr, G. E.; Allam, N. K. Unveiling the Interfacial Interactions of C_{76}/Ni Foam Heterostructures for High-Performance Hydrogen Evolution Reaction

Electrocatalysis. Under review

3- Hasan, M. M.; Khedr, G. E.; Zakaria, F.; Allam, N. K. Intermolecular Electron Transfer in Electrochemically Exfoliated BCN-Cu Nanosheet Electrocatalysts for Efficient Hydrogen Evolution. ACS Appl Energy Mater 2022. https://doi.org/10.1021/acsaem.2c01349.

4- Hasan, M. M.; Allam, N. K. An Alternative, Low-Dissolution Counter Electrode to Prevent Deceptive Enhancement of HER Overpotential. Sci Rep 2022, 12 (1), 1–6. https://doi.org/10.1038/s41598-022-13385-w.

9.4 Author biography

PhD student in Nanotechnology, The American University in Cairo, Sep 2019- Sep 2022

M.Sc. in Nanotechnology, The American University in Cairo, Jun 2018

Thesis Title: Unbiased Spontaneous Solar Fuel Production Using Stable Composite Nanofiber Photocatalysts

B.Sc. in Chemistry, Alexandria University, May 2015

Senior project: Gas Chromatography and its applications.

WORK EXPERIENCE

Jan 2016-Sep 2022 Research and Teaching Assistant, The American University in Cairo

Performed research in various subjects:

- Electrocatalytic water splitting using nanomaterials.
- Nanostructures synthesis techniques.
- Photocatalytic water splitting using nanomaterials (hydrogen generation using solar energy).
- Reduction of CO_2 to hydrocarbon fuels using nanomaterials.
- Nanostructures Characterization techniques analysis.

Awards:

- Yousef Jameel PhD in Applied Sciences and Engineering Fellowship.
- Fadel Assabghy Award for Scholarly Excellence, January 2019.
- Al Ghurair STEM Scholarship.

References

(1) Abas, N.; Kalair, A.; Khan, N. Review of Fossil Fuels and Future Energy Technologies. *Futures* **2015**, *69*, 31–49. https://doi.org/10.1016/j.futures.2015.03.003.

(2) McGlade, C.; Ekins, P. The Geographical Distribution of Fossil Fuels Unused When Limiting Global Warming to 2 °C. *Nature* **2015**, *517* (7533), 187–190. https://doi.org/10.1038/nature14016.

(3) Jakob, M.; Hilaire, J. Unburnable Fossil-Fuel Reserves. *Nature* **2015**, *517* (7533), 150–151. https://doi.org/10.1038/517150a.

(4) Staffell, I.; Scamman, D.; Velazquez Abad, A.; Balcombe, P.; Dodds, P. E.; Ekins, P.; Shah, N.; Ward, K. R. The Role of Hydrogen and Fuel Cells in the Global Energy System. *Energy Environ. Sci.* **2019**, *12* (2), 463–491. https://doi.org/10.1039/c8ee01157e.

(5) Kirubakaran, A.; Jain, S.; Nema, R. K. A Review on Fuel Cell Technologies and Power Electronic Interface. *Renew. Sustain. Energy Rev.* **2009**, *13* (9), 2430–2440. https://doi.org/10.1016/j.rser.2009.04.004.

(6) *World energy consumption by fuel (2015)*. https://www.altenergymag.com/article/2019/07/what-is-the-future-of-non-renewable-resources/31346 (accessed 2022-08-06).

(7) Hasan, M. M.; Tolba, S. A.; Allam, N. K. In Situ Formation of Graphene Stabilizes Zero-Valent Copper Nanoparticles Enhances the Efficiency of Photocatalytic Water Splitting. **2018**. https://doi.org/10.1021/acssuschemeng.8b04219.

(8) Hasan, M. M.; Allam, N. K. Unbiased Spontaneous Solar Hydrogen Production Using Stable TiO_2-CuO Composite Nanofiber Photocatalysts. *RSC Adv.* **2018**, *8* (65), 37219–37228. https://doi.org/10.1039/c8ra06763e.

(9) Liguras, D. K.; Kondarides, D. I.; Verykios, X. E. Production of Hydrogen for Fuel Cells by Steam Reforming of Ethanol over Supported Noble Metal Catalysts. *Appl. Catal. B Environ.* **2003**, *43* (4), 345–354. https://doi.org/10.1016/S0926-3373(02)00327-2.

(10) BARELLI, L.; BIDINI, G.; GALLORINI, F.; SERVILI, S. Hydrogen Production through Sorption-Enhanced Steam Methane Reforming and Membrane Technology: A Review. *Energy* **2008**, *33* (4), 554–570. https://doi.org/10.1016/j.energy.2007.10.018.

(11) SIMPSON, A.; LUTZ, A. Exergy Analysis of Hydrogen Production via Steam Methane Reforming. *Int. J. Hydrogen Energy* **2007**, *32* (18), 4811–4820.

https://doi.org/10.1016/j.ijhydene.2007.08.025.

(12) Boran, A.; Erkan, S.; Ozkar, S.; Eroglu, I. Kinetics of Hydrogen Generation from Hydrolysis of Sodium Borohydride on Pt/C Catalyst in a Flow Reactor. *Int. J. Energy Res.* **2013**, *37* (5), 443–448. https://doi.org/10.1002/er.3007.

(13) Hasan, M. M.; Khedr, G. E.; Zakaria, F.; Allam, N. K. Intermolecular Electron Transfer in Electrochemically Exfoliated BCN-Cu Nanosheet Electrocatalysts for Efficient Hydrogen Evolution. *ACS Appl. Energy Mater.* **2022**. https://doi.org/10.1021/acsaem.2c01349.

(14) Fountaine, K. T.; Lewerenz, H. J.; Atwater, H. A. Efficiency Limits for Photoelectrochemical Water-Splitting. *Nat. Commun.* **2016**, *7* (1), 13706. https://doi.org/10.1038/ncomms13706.

(15) Hisatomi, T.; Kubota, J.; Domen, K. Recent Advances in Semiconductors for Photocatalytic and Photoelectrochemical Water Splitting. *Chem. Soc. Rev.* **2014**, *43* (22), 7520–7535. https://doi.org/10.1039/C3CS60378D.

(16) Anantharaj, S.; Ede, S. R.; Sakthikumar, K.; Karthick, K.; Mishra, S.; Kundu, S. Recent Trends and Perspectives in Electrochemical Water Splitting with an Emphasis on Sulfide, Selenide, and Phosphide Catalysts of Fe, Co, and Ni: A Review. *ACS Catal.* **2016**, *6* (12), 8069–8097. https://doi.org/10.1021/acscatal.6b02479.

(17) Shi, Y.; Zhang, B. Recent Advances in Transition Metal Phosphide Nanomaterials: Synthesis and Applications in Hydrogen Evolution Reaction. *Chem. Soc. Rev.* **2016**, *45* (6), 1529–1541. https://doi.org/10.1039/C5CS00434A.

(18) Rakap, M.; Kalu, E. E.; Özkar, S. Cobalt–nickel–phosphorus Supported on Pd-Activated TiO_2 (Co–Ni–P/Pd-TiO_2) as Cost-Effective and Reusable Catalyst for Hydrogen Generation from Hydrolysis of Alkaline Sodium Borohydride Solution. *J. Alloys Compd.* **2011**, *509* (25), 7016–7021. https://doi.org/10.1016/j.jallcom.2011.04.023.

(19) Satyapal, S.; Petrovic, J.; Read, C.; Thomas, G.; Ordaz, G. The U.S. Department of Energy's National Hydrogen Storage Project: Progress towards Meeting Hydrogen-Powered Vehicle Requirements. *Catal. Today* **2007**, *120* (3–4), 246–256. https://doi.org/10.1016/j.cattod.2006.09.022.

(20) Chao, C. H.; Shieh, J. J. Control and Management for Hydrogen Energy Systems. *Recent Res. Energy, Environ. Entrep. Innov. - Int. Conf. Energy, Environ. Entrep. Innov. ICEEEI'11* **2011**, No. January, 27–31.

(21) Naimi, Y.; Antar, A. Hydrogen Generation by Water Electrolysis. In *Advances In Hydrogen*

Generation Technologies; InTech, 2018. https://doi.org/10.5772/intechopen.76814.

(22) Zhang, J.; Zhang, Q.; Feng, X. Support and Interface Effects in Water-Splitting Electrocatalysts. *Adv. Mater.* **2019**, *31* (31), 1808167. https://doi.org/10.1002/adma.201808167.

(23) Anantharaj, S.; Ede, S. R.; Karthick, K.; Sam Sankar, S.; Sangeetha, K.; Karthik, P. E.; Kundu, S. Precision and Correctness in the Evaluation of Electrocatalytic Water Splitting: Revisiting Activity Parameters with a Critical Assessment. *Energy Environ. Sci.* **2018**, *11* (4), 744–771. https://doi.org/10.1039/C7EE03457A.

(24) Salem, K. E.; Saleh, A. A.; Khedr, G. E.; Shaheen, B. S.; Allam, N. K. Unveiling the Optimal Interfacial Synergy of Plasma-Modulated Trimetallic Mn-Ni-Co Phosphides: Tailoring Deposition Ratio for Complementary Water Splitting. *Energy Environ. Mater.* **2022**, 1–13. https://doi.org/10.1002/eem2.12324.

(25) Hasan, M. M.; Allam, N. K. An Alternative, Low-Dissolution Counter Electrode to Prevent Deceptive Enhancement of HER Overpotential. *Sci. Rep.* **2022**, *12* (1), 1–6. https://doi.org/10.1038/s41598-022-13385-w.

(26) Xiao, P.; Chen, W.; Wang, X. A Review of Phosphide-Based Materials for Electrocatalytic Hydrogen Evolution. *Adv. Energy Mater.* **2015**, *5* (24), 1500985. https://doi.org/10.1002/aenm.201500985.

(27) Marshall, A. T.; Haverkamp, R. G. Electrocatalytic Activity of IrO_2–RuO_2 Supported on Sb-Doped SnO_2 Nanoparticles. *Electrochim. Acta* **2010**, *55* (6), 1978–1984. https://doi.org/10.1016/j.electacta.2009.11.018.

(28) Di Blasi, A.; D'Urso, C.; Baglio, V.; Antonucci, V.; Arico', A. S.; Ornelas, R.; Matteucci, F.; Orozco, G.; Beltran, D.; Meas, Y.; Arriaga, L. G. Preparation and Evaluation of RuO_2–IrO_2, IrO_2–Pt and IrO_2–Ta_2O_5 Catalysts for the Oxygen Evolution Reaction in an SPE Electrolyzer. *J. Appl. Electrochem.* **2009**, *39* (2), 191–196. https://doi.org/10.1007/s10800-008-9651-y.

(29) Lee, Y.; Suntivich, J.; May, K. J.; Perry, E. E.; Shao-Horn, Y. Synthesis and Activities of Rutile IrO 2 and RuO 2 Nanoparticles for Oxygen Evolution in Acid and Alkaline Solutions. *J. Phys. Chem. Lett.* **2012**, *3* (3), 399–404. https://doi.org/10.1021/jz2016507.

(30) Zeng, K.; Zhang, D. Recent Progress in Alkaline Water Electrolysis for Hydrogen Production and Applications. *Prog. Energy Combust. Sci.* **2010**, *36* (3), 307–326.

https://doi.org/10.1016/j.pecs.2009.11.002.

(31) Kannimuthu, K.; Sangeetha, K.; Sankar, S. INORGANIC CHEMISTRY FRONTIERS Investigation on Nanostructured Cu-Based Electrocatalysts for Improvising Water Splitting : A Review. **2021**, 234–272. https://doi.org/10.1039/d0qi01060j.

(32) Sun, X.; Zhu, Q.; Kang, X.; Liu, H.; Qian, Q.; Ma, J.; Zhang, Z.; Yang, G.; Han, B. Design of a Cu (I)/ C-Doped Boron Nitride Electrocatalyst for e Ffi Cient Conversion Of. **2017**, 2086–2091. https://doi.org/10.1039/c7gc00503b.

(33) Bockris, J. O.; Otagawa, T. Mechanism of Oxygen Evolution on Perovskites. *J. Phys. Chem.* **1983**, *87* (15), 2960–2971. https://doi.org/10.1021/j100238a048.

(34) Lyons, M. E. G.; Floquet, S. Mechanism of Oxygen Reactions at Porous Oxide Electrodes. Part 2—Oxygen Evolution at RuO_2, IrO_2 and IrxRu1−xO_2 Electrodes in Aqueous Acid and Alkaline Solution. *Phys. Chem. Chem. Phys.* **2011**, *13* (12), 5314. https://doi.org/10.1039/c0cp02875d.

(35) Lyons, M. E. G.; Burke, L. D. Mechanism of Oxygen Reactions at Porous Oxide Electrodes. Part 1.—Oxygen Evolution at RuO2 and RuxSn1–xO2 Electrodes in Alkaline Solution under Vigorous Electrolysis Conditions. *J. Chem. Soc. Faraday Trans. 1 Phys. Chem. Condens. Phases* **1987**, *83* (2), 299. https://doi.org/10.1039/f19878300299.

(36) Bockris, J. O. Kinetics of Activation Controlled Consecutive Electrochemical Reactions: Anodic Evolution of Oxygen. *J. Chem. Phys.* **1956**, *24* (4), 817–827. https://doi.org/10.1063/1.1742616.

(37) Fabbri, E.; Habereder, A.; Waltar, K.; Kötz, R.; Schmidt, T. J. Developments and Perspectives of Oxide-Based Catalysts for the Oxygen Evolution Reaction. *Catal. Sci. Technol.* **2014**, *4* (11), 3800–3821. https://doi.org/10.1039/C4CY00669K.

(38) Wade, W. H.; Hackerman, N. Anodic Phenomena at an Iron Electrode. *Trans. Faraday Soc.* **1957**, *53*, 1636. https://doi.org/10.1039/tf9575301636.

(39) Visintin, A.; Chialvo, A. C.; Triaca, W. E.; Arvia, A. J. The Electroformation of Thick Hydrous Nickel Hydroxide Films through the Application of Periodic Potential Signals. *J. Electroanal. Chem. Interfacial Electrochem.* **1987**, *225* (1–2), 227–239. https://doi.org/10.1016/0022-0728(87)80016-5.

(40) Dau, H.; Limberg, C.; Reier, T.; Risch, M.; Roggan, S.; Strasser, P. The Mechanism of Water Oxidation: From Electrolysis via Homogeneous to Biological Catalysis. *ChemCatChem* **2010**,

2 (7), 724–761. https://doi.org/10.1002/cctc.201000126.

(41) Shinagawa, T.; Garcia-Esparza, A. T.; Takanabe, K. Insight on Tafel Slopes from a Microkinetic Analysis of Aqueous Electrocatalysis for Energy Conversion. *Sci. Rep.* **2015**, *5* (1), 13801. https://doi.org/10.1038/srep13801.

(42) Allen J. Bard, L. R. F. *Electrochemical Methods: Fundamentals and Applications*; 2000.

(43) Katz, E. Electrochemical Contributions: Julius Tafel (1862–1918). *Electrochem. Sci. Adv.* **2022**. https://doi.org/10.1002/elsa.202260002.

(44) Anantharaj, S.; Kundu, S. Do the Evaluation Parameters Reflect Intrinsic Activity of Electrocatalysts in Electrochemical Water Splitting? *ACS Energy Lett.* **2019**, *4* (6), 1260–1264. https://doi.org/10.1021/acsenergylett.9b00686.

(45) Wang, Y.; Zhang, Y.; Liu, Z.; Xie, C.; Feng, S.; Liu, D.; Shao, M.; Wang, S. Layered Double Hydroxide Nanosheets with Multiple Vacancies Obtained by Dry Exfoliation as Highly Efficient Oxygen Evolution Electrocatalysts. *Angew. Chemie Int. Ed.* **2017**, *56* (21), 5867–5871. https://doi.org/10.1002/anie.201701477.

(46) Popczun, E. J.; McKone, J. R.; Read, C. G.; Biacchi, A. J.; Wiltrout, A. M.; Lewis, N. S.; Schaak, R. E. Nanostructured Nickel Phosphide as an Electrocatalyst for the Hydrogen Evolution Reaction. *J. Am. Chem. Soc.* **2013**, *135* (25), 9267–9270. https://doi.org/10.1021/ja403440e.

(47) Morales-Guio, C. G.; Stern, L.-A.; Hu, X. Nanostructured Hydrotreating Catalysts for Electrochemical Hydrogen Evolution. *Chem. Soc. Rev.* **2014**, *43* (18), 6555. https://doi.org/10.1039/C3CS60468C.

(48) Xia, C.; Jiang, Q.; Zhao, C.; Hedhili, M. N.; Alshareef, H. N. Selenide-Based Electrocatalysts and Scaffolds for Water Oxidation Applications. *Adv. Mater.* **2016**, *28* (1), 77–85. https://doi.org/10.1002/adma.201503906.

(49) Ye, R.; del Angel-Vicente, P.; Liu, Y.; Arellano-Jimenez, M. J.; Peng, Z.; Wang, T.; Li, Y.; Yakobson, B. I.; Wei, S.-H.; Yacaman, M. J.; Tour, J. M. High-Performance Hydrogen Evolution from MoS_2(1- x)Px Solid Solution. *Adv. Mater.* **2016**, *28* (7), 1427–1432. https://doi.org/10.1002/adma.201504866.

(50) Katsounaros, I.; Cherevko, S.; Zeradjanin, A. R.; Mayrhofer, K. J. J. Oxygen Electrochemistry as a Cornerstone for Sustainable Energy Conversion. *Angew. Chemie Int. Ed.* **2014**, *53* (1), 102–121. https://doi.org/10.1002/anie.201306588.

(51) Sun, H.; Xu, X.; Yan, Z.; Chen, X.; Jiao, L.; Cheng, F.; Chen, J. Superhydrophilic Amorphous Co–B–P Nanosheet Electrocatalysts with Pt-like Activity and Durability for the Hydrogen Evolution Reaction. *J. Mater. Chem. A* **2018**, *6* (44), 22062–22069. https://doi.org/10.1039/C8TA02999G.

(52) Sun, H.; Yan, Z.; Liu, F.; Xu, W.; Cheng, F.; Chen, J. Self-Supported Transition-Metal-Based Electrocatalysts for Hydrogen and Oxygen Evolution. *Adv. Mater.* **2020**, *32* (3), 1806326. https://doi.org/10.1002/adma.201806326.

(53) Lei, M.; Wang, N.; Zhu, L.; Zhou, Q.; Nie, G.; Tang, H. Photocatalytic Reductive Degradation of Polybrominated Diphenyl Ethers on CuO/TiO_2 nanocomposites: A Mechanism Based on the Switching of Photocatalytic Reduction Potential Being Controlled by the Valence State of Copper. *Appl. Catal. B Environ.* **2016**, *182*, 414–423. https://doi.org/10.1016/j.apcatb.2015.09.031.

(54) Lu, Z.; Zhu, W.; Yu, X.; Zhang, H.; Li, Y.; Sun, X.; Wang, X.; Wang, H.; Wang, J.; Luo, J.; Lei, X.; Jiang, L. Ultrahigh Hydrogen Evolution Performance of Under-Water "Superaerophobic" MoS_2 Nanostructured Electrodes. *Adv. Mater.* **2014**, *26* (17), 2683–2687. https://doi.org/10.1002/adma.201304759.

(55) Li, H.; Chen, S.; Zhang, Y.; Zhang, Q.; Jia, X.; Zhang, Q.; Gu, L.; Sun, X.; Song, L.; Wang, X. Systematic Design of Superaerophobic Nanotube-Array Electrode Comprised of Transition-Metal Sulfides for Overall Water Splitting. *Nat. Commun.* **2018**, *9* (1), 2452. https://doi.org/10.1038/s41467-018-04888-0.

(56) Pi, Y.; Shao, Q.; Wang, P.; Lv, F.; Guo, S.; Guo, J.; Huang, X. Trimetallic Oxyhydroxide Coralloids for Efficient Oxygen Evolution Electrocatalysis. *Angew. Chemie Int. Ed.* **2017**, *56* (16), 4502–4506. https://doi.org/10.1002/anie.201701533.

(57) Liu, B.; Zhao, Y.-F.; Peng, H.-Q.; Zhang, Z.-Y.; Sit, C.-K.; Yuen, M.-F.; Zhang, T.-R.; Lee, C.-S.; Zhang, W.-J. Nickel-Cobalt Diselenide 3D Mesoporous Nanosheet Networks Supported on Ni Foam: An All-PH Highly Efficient Integrated Electrocatalyst for Hydrogen Evolution. *Adv. Mater.* **2017**, *29* (19), 1606521. https://doi.org/10.1002/adma.201606521.

(58) Jiang, P.; Liu, Q.; Liang, Y.; Tian, J.; Asiri, A. M.; Sun, X. A Cost-Effective 3D Hydrogen Evolution Cathode with High Catalytic Activity: FeP Nanowire Array as the Active Phase. *Angew. Chemie Int. Ed.* **2014**, *53* (47), 12855–12859. https://doi.org/10.1002/anie.201406848.

(59) Zhang, N.; Gan, S.; Wu, T.; Ma, W.; Han, D.; Niu, L. Growth Control of MoS_2 Nanosheets

on Carbon Cloth for Maximum Active Edges Exposed: An Excellent Hydrogen Evolution 3D Cathode. *ACS Appl. Mater. Interfaces* **2015**, *7* (22), 12193–12202. https://doi.org/10.1021/acsami.5b02586.

(60) Zhu, Y.-P.; Liu, Y.-P.; Ren, T.-Z.; Yuan, Z.-Y. Self-Supported Cobalt Phosphide Mesoporous Nanorod Arrays: A Flexible and Bifunctional Electrode for Highly Active Electrocatalytic Water Reduction and Oxidation. *Adv. Funct. Mater.* **2015**, *25* (47), 7337–7347. https://doi.org/10.1002/adfm.201503666.

(61) Hanawa, T. Electrodeposition of Calcium Phosphates, Oxides, and Molecules to Achieve Biocompatibility of Metals. In *Encyclopedia of Interfacial Chemistry*; Elsevier, 2018; pp 129–140. https://doi.org/10.1016/B978-0-12-409547-2.11159-X.

(62) Electrospinning Process. In *An Introduction to Electrospinning and Nanofibers*; WORLD SCIENTIFIC, 2005; pp 90–154. https://doi.org/10.1142/9789812567611_0003.

(63) Greiner, A.; Wendorff, J. H. Electrospinning: A Fascinating Method for the Preparation of Ultrathin Fibers. *Angew. Chemie Int. Ed.* **2007**, *46* (30), 5670–5703. https://doi.org/10.1002/anie.200604646.

(64) Yang, L.; Raza, A.; Si, Y.; Mao, X.; Shang, Y.; Ding, B.; Yu, J.; Al-Deyab, S. S. Synthesis of Superhydrophobic Silica Nanofibrous Membranes with Robust Thermal Stability and Flexibility via in Situ Polymerization. *Nanoscale* **2012**, *4* (20), 6581. https://doi.org/10.1039/c2nr32095a.

(65) Li, D.; Xia, Y. Electrospinning of Nanofibers: Reinventing the Wheel? *Adv. Mater.* **2004**, *16* (14), 1151–1170. https://doi.org/10.1002/adma.200400719.

(66) Lockwood, D. J.; Bin Ding, J. yu. *Electrospun Nanofi Bers for Energy and Environmental Applications*; 2015. https://doi.org/10.1007/978-3-642-54160-5.

(67) Nalbandian, M. Development and Optimization of Chemically-Active Electrospun Nanofibers for Treatment of Impaired Water Sources, 2014.

(68) Abbas, M. A.; Bang, J. H. Rising Again: Opportunities and Challenges for Platinum-Free Electrocatalysts. *Chem. Mater.* **2015**, *27* (21), 7218–7235. https://doi.org/10.1021/acs.chemmater.5b03331.

(69) Li, J.-S.; Wang, Y.; Liu, C.-H.; Li, S.-L.; Wang, Y.-G.; Dong, L.-Z.; Dai, Z.-H.; Li, Y.-F.; Lan, Y.-Q. Coupled Molybdenum Carbide and Reduced Graphene Oxide Electrocatalysts for Efficient Hydrogen Evolution. *Nat. Commun.* **2016**, *7* (1), 11204.

https://doi.org/10.1038/ncomms11204.

(70) Fan, L.; Liu, P. F.; Yan, X.; Gu, L.; Yang, Z. Z.; Yang, H. G.; Qiu, S.; Yao, X. Atomically Isolated Nickel Species Anchored on Graphitized Carbon for Efficient Hydrogen Evolution Electrocatalysis. *Nat. Commun.* **2016**, *7* (1), 10667. https://doi.org/10.1038/ncomms10667.

(71) Chen, R.; Yang, C.; Cai, W.; Wang, H. Y.; Miao, J.; Zhang, L.; Chen, S.; Liu, B. Use of Platinum as the Counter Electrode to Study the Activity of Nonprecious Metal Catalysts for the Hydrogen Evolution Reaction. *ACS Energy Letters*. 2017, pp 1070–1075. https://doi.org/10.1021/acsenergylett.7b00219.

(72) Dong, G.; Fang, M.; Wang, H.; Yip, S.; Cheung, H.-Y.; Wang, F.; Wong, C.-Y.; Chu, S. T.; Ho, J. C. Insight into the Electrochemical Activation of Carbon-Based Cathodes for Hydrogen Evolution Reaction. *J. Mater. Chem. A* **2015**, *3* (24), 13080–13086. https://doi.org/10.1039/C5TA02551F.

(73) Tian, M.; Cousins, C.; Beauchemin, D.; Furuya, Y.; Ohma, A.; Jerkiewicz, G. Influence of the Working and Counter Electrode Surface Area Ratios on the Dissolution of Platinum under Electrochemical Conditions. *ACS Catal.* **2016**, *6* (8), 5108–5116. https://doi.org/10.1021/acscatal.6b00200.

(74) Ota, K.-I.; Nishigori, S.; Kamiya, N. Dissolution of Platinum Anodes in Sulfuric Acid Solution. *J. Electroanal. Chem. Interfacial Electrochem.* **1988**, *257* (1–2), 205–215. https://doi.org/10.1016/0022-0728(88)87042-6.

(75) Bird, M. A.; Goodwin, S. E.; Walsh, D. A. Best Practice for Evaluating Electrocatalysts for Hydrogen Economy. *ACS Appl. Mater. Interfaces* **2020**, *12* (18), 20500–20506. https://doi.org/10.1021/acsami.0c03307.

(76) Wang, X.; Maeda, K.; Chen, X.; Takanabe, K.; Domen, K.; Hou, Y.; Fu, X.; Antonietti, M. Polymer Semiconductors for Artificial Photosynthesis: Hydrogen Evolution by Mesoporous Graphitic Carbon Nitride with Visible Light. *J. Am. Chem. Soc.* **2009**, *131* (5), 1680–1681. https://doi.org/10.1021/ja809307s.

(77) Abe, R. Recent Progress on Photocatalytic and Photoelectrochemical Water Splitting under Visible Light Irradiation. *J. Photochem. Photobiol. C Photochem. Rev.* **2010**, *11* (4), 179–209. https://doi.org/10.1016/j.jphotochemrev.2011.02.003.

(78) Khedr, G. E.; Abdallah, T.; Morsi, R. E.; Talaat, H. Enhanced Photovoltaic Parameters of Titania/Graphene Nanocomposites Based Dye Sensitized Solar Cells. *J. Phys. Conf. Ser.*

2019, *1253* (1). https://doi.org/10.1088/1742-6596/1253/1/012030.

(79) Ahsan, M. A.; He, T.; Eid, K.; Abdullah, A. M.; Curry, M. L.; Du, A.; Puente Santiago, A. R.; Echegoyen, L.; Noveron, J. C. Tuning the Intermolecular Electron Transfer of Low-Dimensional and Metal-Free BCN/C60Electrocatalysts via Interfacial Defects for Efficient Hydrogen and Oxygen Electrochemistry. *J. Am. Chem. Soc.* **2021**, *143* (2), 1203–1215. https://doi.org/10.1021/jacs.0c12386.

(80) Guiding Principles for Designing Highly Efficient Metal-Free Carbon Catalysts, 2019.Pdf.

(81) Wang, S.; Ma, F.; Jiang, H.; Shao, Y.; Wu, Y.; Hao, X. Band Gap-Tunable Porous Borocarbonitride Nanosheets for High Energy-Density Supercapacitors. *ACS Appl. Mater. Interfaces* **2018**, *10* (23), 19588–19597. https://doi.org/10.1021/acsami.8b02317.

(82) Tay, R. Y.; Li, H.; Tsang, S. H.; Zhu, M.; Loeblein, M.; Jing, L.; Leong, F. N.; Teo, E. H. T. Trimethylamine Borane: A New Single-Source Precursor for Monolayer h-BN Single Crystals and h-BCN Thin Films. *Chem. Mater.* **2016**, *28* (7), 2180–2190. https://doi.org/10.1021/acs.chemmater.6b00114.

(83) Hao, Y.; Wang, S.; Shao, Y.; Wu, Y.; Miao, S. High-Energy Density Li-Ion Capacitor with Layered SnS 2 /Reduced Graphene Oxide Anode and BCN Nanosheet Cathode. *Adv. Energy Mater.* **2020**, *10* (6), 1902836. https://doi.org/10.1002/aenm.201902836.

(84) Ahsan, M. A.; He, T.; Eid, K.; Abdullah, A. M.; Curry, M. L.; Du, A.; Puente Santiago, A. R.; Echegoyen, L.; Noveron, J. C. Tuning the Intermolecular Electron Transfer of Low-Dimensional and Metal-Free BCN/C_{60} Electrocatalysts via Interfacial Defects for Efficient Hydrogen and Oxygen Electrochemistry . *J. Am. Chem. Soc.* **2021**. https://doi.org/10.1021/jacs.0c12386.

(85) Thaweesak, S.; Wang, S.; Lyu, M.; Xiao, M.; Peerakiatkhajohn, P.; Wang, L. Boron-Doped Graphitic Carbon Nitride Nanosheets for Enhanced Visible Light Photocatalytic Water Splitting. *Dalt. Trans.* **2017**, *46* (32), 10714–10720. https://doi.org/10.1039/c7dt00933j.

(86) Karapinar, D.; Huan, N. T.; Sahraie, N. R.; Li, J.; Wakerley, D.; Touati, N.; Zanna, S.; Taverna, D.; Henrique, L.; Zitolo, A.; Fr, Ø.; Jaouen, Ø.; Mougel, V.; Fontecave, M. Electroreduction of CO_2 on Single-Site Copper-Nitrogen-Doped Carbon Material : Selective Formation of Ethanol and Reversible Restructuration of the Metal Sites Research Articles Angewandte. **2019**, 15098–15103. https://doi.org/10.1002/anie.201907994.

(87) Zhang, Y.; Du, H.; Ma, Y.; Ji, L.; Guo, H.; Tian, Z.; Chen, H.; Huang, H.; Cui, G.; Asiri, A.

M.; Qu, F.; Chen, L.; Sun, X. Hexagonal Boron Nitride Nanosheet for Effective Ambient N2 Fixation to NH3. *Nano Res.* **2019**, *12* (4), 919–924. https://doi.org/10.1007/s12274-019-2323-x.

(88) Zhang, M.; Gao, G.; Kutana, A.; Wang, Y.; Zou, X.; Tse, J. S.; Yakobson, B. I.; Li, H.; Liu, H.; Ma, Y. Two-Dimensional Boron-Nitrogen-Carbon Monolayers with Tunable Direct Band Gaps. *Nanoscale* **2015**, *7* (28), 12023–12029. https://doi.org/10.1039/c5nr03344f.

(89) Chen, M.; Guan, R.; Yang, S. Hybrids of Fullerenes and 2D Nanomaterials. *Adv. Sci.* **2019**, *6* (1), 1800941. https://doi.org/10.1002/advs.201800941.

(90) Puente Santiago, A. R.; Fernandez-Delgado, O.; Gomez, A.; Ahsan, M. A.; Echegoyen, L. Fullerenes as Key Components for Low-Dimensional (Photo)Electrocatalytic Nanohybrid Materials. *Angew. Chemie Int. Ed.* **2021**, *60* (1), 122–141. https://doi.org/10.1002/anie.202009449.

(91) Wang, H.; Zhang, X.; Meng, J.; Yin, Z.; Liu, X.; Zhao, Y.; Zhang, L. Controlled Growth of Few-Layer Hexagonal Boron Nitride on Copper Foils Using Ion Beam Sputtering Deposition. *Small* **2015**, *11* (13), 1542–1547. https://doi.org/10.1002/smll.201402468.

(92) Feng, P. X.; Sajjad, M. Few-Atomic-Layer Boron Nitride Sheets Syntheses and Applications for Semiconductor Diodes. *Mater. Lett.* **2012**, *89*, 206–208. https://doi.org/10.1016/j.matlet.2012.08.053.

(93) Velázquez, D.; Seibert, R.; Man, H.; Spentzouris, L.; Terry, J. Pulsed Laser Deposition of Single Layer, Hexagonal Boron Nitride (White Graphene, h-BN) on Fiber-Oriented Ag(111)/SrTiO 3 (001). *J. Appl. Phys.* **2016**, *119* (9), 095306. https://doi.org/10.1063/1.4943174.

(94) Song, L.; Ci, L.; Lu, H.; Sorokin, P. B.; Jin, C.; Ni, J.; Kvashnin, A. G.; Kvashnin, D. G.; Lou, J.; Yakobson, B. I.; Ajayan, P. M. Large Scale Growth and Characterization of Atomic Hexagonal Boron Nitride Layers. *Nano Lett.* **2010**, *10* (8), 3209–3215. https://doi.org/10.1021/nl1022139.

(95) Shi, Y.; Hamsen, C.; Jia, X.; Kim, K. K.; Reina, A.; Hofmann, M.; Hsu, A. L.; Zhang, K.; Li, H.; Juang, Z.-Y.; Dresselhaus, M. S.; Li, L.-J.; Kong, J. Synthesis of Few-Layer Hexagonal Boron Nitride Thin Film by Chemical Vapor Deposition. *Nano Lett.* **2010**, *10* (10), 4134–4139. https://doi.org/10.1021/nl1023707.

(96) Kim, K. K.; Hsu, A.; Jia, X.; Kim, S. M.; Shi, Y.; Hofmann, M.; Nezich, D.; Rodriguez-Nieva,

J. F.; Dresselhaus, M.; Palacios, T.; Kong, J. Synthesis of Monolayer Hexagonal Boron Nitride on Cu Foil Using Chemical Vapor Deposition. *Nano Lett.* **2012**, *12* (1), 161–166. https://doi.org/10.1021/nl203249a.

(97) Tay, R. Y.; Griep, M. H.; Mallick, G.; Tsang, S. H.; Singh, R. S.; Tumlin, T.; Teo, E. H. T.; Karna, S. P. Growth of Large Single-Crystalline Two-Dimensional Boron Nitride Hexagons on Electropolished Copper. *Nano Lett.* **2014**, *14* (2), 839–846. https://doi.org/10.1021/nl404207f.

(98) Tay, R. Y.; Wang, X.; Tsang, S. H.; Loh, G. C.; Singh, R. S.; Li, H.; Mallick, G.; Tong Teo, E. H. A Systematic Study of the Atmospheric Pressure Growth of Large-Area Hexagonal Crystalline Boron Nitride Film. *J. Mater. Chem. C* **2014**, *2* (9), 1650. https://doi.org/10.1039/c3tc32011a.

(99) Tay, R. Y.; Tsang, S. H.; Loeblein, M.; Chow, W. L.; Loh, G. C.; Toh, J. W.; Ang, S. L.; Teo, E. H. T. Direct Growth of Nanocrystalline Hexagonal Boron Nitride Films on Dielectric Substrates. *Appl. Phys. Lett.* **2015**, *106* (10), 101901. https://doi.org/10.1063/1.4914474.

(100) Nakhaie, S.; Wofford, J. M.; Schumann, T.; Jahn, U.; Ramsteiner, M.; Hanke, M.; Lopes, J. M. J.; Riechert, H. Synthesis of Atomically Thin Hexagonal Boron Nitride Films on Nickel Foils by Molecular Beam Epitaxy. *Appl. Phys. Lett.* **2015**, *106* (21), 213108. https://doi.org/10.1063/1.4921921.

(101) Zhang, C.; Zhao, S.; Jin, C.; Koh, A. L.; Zhou, Y.; Xu, W.; Li, Q.; Xiong, Q.; Peng, H.; Liu, Z. Direct Growth of Large-Area Graphene and Boron Nitride Heterostructures by a Co-Segregation Method. *Nat. Commun.* **2015**, *6* (1), 6519. https://doi.org/10.1038/ncomms7519.

(102) Zhang, C.; Fu, L.; Zhao, S.; Zhou, Y.; Peng, H.; Liu, Z. Controllable Co-Segregation Synthesis of Wafer-Scale Hexagonal Boron Nitride Thin Films. *Adv. Mater.* **2014**, *26* (11), 1776–1781. https://doi.org/10.1002/adma.201304301.

(103) Suzuki, S.; Pallares, R. M.; Hibino, H. Growth of Atomically Thin Hexagonal Boron Nitride Films by Diffusion through a Metal Film and Precipitation. *J. Phys. D. Appl. Phys.* **2012**, *45* (38), 385304. https://doi.org/10.1088/0022-3727/45/38/385304.

(104) Xu, M.; Fujita, D.; Chen, H.; Hanagata, N. Formation of Monolayer and Few-Layer Hexagonal Boron Nitride Nanosheets via Surface Segregation. *Nanoscale* **2011**, *3* (7), 2854. https://doi.org/10.1039/c1nr10294j.

(105) Sutter, P.; Lahiri, J.; Zahl, P.; Wang, B.; Sutter, E. Scalable Synthesis of Uniform Few-Layer Hexagonal Boron Nitride Dielectric Films. *Nano Lett.* **2013**, *13* (1), 276–281. https://doi.org/10.1021/nl304080y.

(106) Nappini, S.; Píš, I.; Menteş, T. O.; Sala, A.; Cattelan, M.; Agnoli, S.; Bondino, F.; Magnano, E. Formation of a Quasi-Free-Standing Single Layer of Graphene and Hexagonal Boron Nitride on Pt(111) by a Single Molecular Precursor. *Adv. Funct. Mater.* **2016**, *26* (7), 1120–1126. https://doi.org/10.1002/adfm.201503591.

(107) Tay, R. Y.; Li, H.; Tsang, S. H.; Zhu, M.; Loeblein, M.; Jing, L.; Leong, F. N.; Teo, E. H. T. Trimethylamine Borane: A New Single-Source Precursor for Monolayer h-BN Single Crystals and h-BCN Thin Films. *Chem. Mater.* **2016**, *28* (7), 2180–2190. https://doi.org/10.1021/acs.chemmater.6b00114.

(108) Beniwal, S.; Hooper, J.; Miller, D. P.; Costa, P. S.; Chen, G.; Liu, S.-Y.; Dowben, P. A.; Sykes, E. C. H.; Zurek, E.; Enders, A. Graphene-like Boron–Carbon–Nitrogen Monolayers. *ACS Nano* **2017**, *11* (3), 2486–2493. https://doi.org/10.1021/acsnano.6b08136.

(109) Wang, Y.; Meng, J.; Tian, Y.; Chen, Y.; Wang, G.; Yin, Z.; Jin, P.; You, J.; Wu, J.; Zhang, X. Deep Ultraviolet Photodetectors Based on Carbon-Doped Two-Dimensional Hexagonal Boron Nitride. *ACS Appl. Mater. Interfaces* **2020**, *12* (24), 27361–27367. https://doi.org/10.1021/acsami.0c05850.

(110) Cheng, L.; Meng, J.; Pan, X.; Lu, Y.; Zhang, X.; Gao, M.; Yin, Z.; Wang, D.; Wang, Y.; You, J.; Zhang, J.; Xie, E. Two-Dimensional Hexagonal Boron-Carbon-Nitrogen Atomic Layers. *Nanoscale* **2019**, *11* (21), 10454–10462. https://doi.org/10.1039/c9nr00712a.

(111) Chen, M.; Guan, R.; Yang, S. Hybrids of Fullerenes and 2D Nanomaterials. *Adv. Sci.* **2019**, *6* (1). https://doi.org/10.1002/advs.201800941.

(112) O'Hayre, R.; Cha, S.-W.; Colella, W.; Prinz, F. B. *Fuel Cell Fundamentals*; John Wiley & Sons, Inc: Hoboken, NJ, USA, 2016; Vol. 15. https://doi.org/10.1002/9781119191766.

(113) Voiry, D.; Shin, H. S.; Loh, K. P.; Chhowalla, M. Low-Dimensional Catalysts for Hydrogen Evolution and CO_2 Reduction. *Nat. Rev. Chem.* **2018**, *2* (1), 0105. https://doi.org/10.1038/s41570-017-0105.

(114) Puente Santiago, A. R.; He, T.; Eraso, O.; Ahsan, M. A.; Nair, A. N.; Chava, V. S. N.; Zheng, T.; Pilla, S.; Fernandez-Delgado, O.; Du, A.; Sreenivasan, S. T.; Echegoyen, L. Tailoring the Interfacial Interactions of van Der Waals 1T-MoS_2/C_{60} Heterostructures for High-

Performance Hydrogen Evolution Reaction Electrocatalysis. *J. Am. Chem. Soc.* **2020**, *142* (42), 17923–17927. https://doi.org/10.1021/jacs.0c08867.

(115) Gao, R.; Dai, Q.; Du, F.; Yan, D.; Dai, L. C 60 -Adsorbed Single-Walled Carbon Nanotubes as Metal-Free, PH-Universal, and Multifunctional Catalysts for Oxygen Reduction, Oxygen Evolution, and Hydrogen Evolution. *J. Am. Chem. Soc.* **2019**, *141* (29), 11658–11666. https://doi.org/10.1021/jacs.9b05006.

(116) Liang, H.; Gandi, A. N.; Anjum, D. H.; Wang, X.; Schwingenschlögl, U.; Alshareef, H. N. Plasma-Assisted Synthesis of NiCoP for Efficient Overall Water Splitting. *Nano Lett.* **2016**, *16* (12), 7718–7725. https://doi.org/10.1021/acs.nanolett.6b03803.

(117) Hu, X.; Tian, X.; Lin, Y. W.; Wang, Z. Nickel Foam and Stainless Steel Mesh as Electrocatalysts for Hydrogen Evolution Reaction, Oxygen Evolution Reaction and Overall Water Splitting in Alkaline Media. *RSC Adv.* **2019**, *9* (54), 31563–31571. https://doi.org/10.1039/c9ra07258f.

(118) Zhang, L.; Lin, C.; Zhang, D.; Gong, L.; Zhu, Y.; Zhao, Z.; Xu, Q.; Li, H.; Xia, Z. Guiding Principles for Designing Highly Efficient Metal-Free Carbon Catalysts. *Adv. Mater.* **2019**, *31* (13), 1805252. https://doi.org/10.1002/adma.201805252.

(119) Online, V. A.; Chronopoulos, D. D.; Stangel, C.; Scheibe, M.; Tagmatarchis, N.; Otyepka, M. ChemComm Covalent Non-Metal Graphene – Fullerene Hybrid †. **2022**, 8396–8399. https://doi.org/10.1039/d2cc02272a.

(120) Du, Z.; Jannatun, N.; Yu, D.; Ren, J.; Huang, W.; Lu, X. C60-Decorated Nickel–cobalt Phosphide as an Efficient and Robust Electrocatalyst for Hydrogen Evolution Reaction. **2018**, 23070–23079. https://doi.org/10.1039/c8nr07472k.

(121) Fernandez-delgado, O.; Santiago, A. R. P.; Betancourth, J. G.; Sanad, M. F.; Sreenivasan, S. T.; Echegoyen, L. Diazonium Functionalized Fullerenes : A New Class of e Ffi Cient Molecular Catalysts for the Hydrogen Evolution Reaction †. **2022**, 3858–3864. https://doi.org/10.1039/d1nr05498h.

(122) Santiago, A. R. P.; He, T.; Eraso, O.; Ahsan, A.; Nair, A. N.; Chava, V. S. N.; Zheng, T.; Pilla, S.; Fernandez-delgado, O.; Du, A.; Sreenivasan, S. T.; Echegoyen, L. Tailoring the Interfacial Interactions of van Der Waals 1T-MoS_2/C_{60} Heterostructures for High-Performance Hydrogen Evolution Reaction Electrocatalysis. **2020**. https://doi.org/10.1021/jacs.0c08867.

(123) Chiral, C.; Li, Q.; Wudl, F.; Thilgen, C.; Whetten, R. L.; Diederich, F. Unusual Electrochemical Properties of the Higher. **1992**, No. 4, 3994–3996.

(124) Puente Santiago, A. R.; Fernandez-Delgado, O.; Gomez, A.; Ahsan, M. A.; Echegoyen, L.; Barzegar, H. R.; Gracia-Espino, E.; Yan, A.; Ojeda-Aristizabal, C.; Dunn, G.; Wågberg, T.; Zettl, A. C 60 /Collapsed Carbon Nanotube Hybrids: A Variant of Peapods. *Angew. Chemie Int. Ed.* **2015**, *15* (2), 122–141. https://doi.org/10.1002/anie.202009449.

(125) Song, F.; Bai, L.; Moysiadou, A.; Lee, S.; Hu, C.; Liardet, L.; Hu, X. Transition Metal Oxides as Electrocatalysts for the Oxygen Evolution Reaction in Alkaline Solutions: An Application-Inspired Renaissance. *J. Am. Chem. Soc.* **2018**, *140* (25), 7748–7759. https://doi.org/10.1021/jacs.8b04546.

(126) Kumaravel, S.; Karthick, K.; Sankar, S. S.; Karmakar, A.; Madhu, R.; Bera, K.; Kundu, S. Current Progressions in Transition Metal Based Hydroxides as Bi-Functional Catalysts towards Electrocatalytic Total Water Splitting. *Sustain. Energy Fuels* **2021**, *5* (24), 6215–6268. https://doi.org/10.1039/D1SE01193F.

(127) Wang, M.; Zhang, L.; He, Y.; Zhu, H. Recent Advances in Transition-Metal-Sulfide-Based Bifunctional Electrocatalysts for Overall Water Splitting. *J. Mater. Chem. A* **2021**, *9* (9), 5320–5363. https://doi.org/10.1039/D0TA12152E.

(128) Wang, Y.; Kong, B.; Zhao, D.; Wang, H.; Selomulya, C. Strategies for Developing Transition Metal Phosphides as Heterogeneous Electrocatalysts for Water Splitting. *Nano Today* **2017**, *15*, 26–55. https://doi.org/10.1016/j.nantod.2017.06.006.

(129) Xu, J.; Li, J.; Xiong, D.; Zhang, B.; Liu, Y.; Wu, K.-H.; Amorim, I.; Li, W.; Liu, L. Trends in Activity for the Oxygen Evolution Reaction on Transition Metal (M = Fe, Co, Ni) Phosphide Pre-Catalysts. *Chem. Sci.* **2018**, *9* (14), 3470–3476. https://doi.org/10.1039/C7SC05033J.

(130) Chen, P.; Ye, J.; Wang, H.; Ouyang, L.; Zhu, M. Recent Progress of Transition Metal Carbides/Nitrides for Electrocatalytic Water Splitting. *J. Alloys Compd.* **2021**, *883*, 160833. https://doi.org/10.1016/j.jallcom.2021.160833.

(131) Gomaa, A. K.; Shaheen, B. S.; Khedr, G. E.; Mokhtar, A. M.; Allam, N. K. Facile Surface Treatment of Industrial Stainless Steel Waste Meshes at Mild Conditions to Produce E Ffi Cient Oxygen Evolution Catalysts. **2022**. https://doi.org/10.1021/acs.energyfuels.2c01562.

(132) Li, S.; Li, E.; An, X.; Hao, X.; Jiang, Z.; Guan, G. Transition Metal-Based Catalysts for

Electrochemical Water Splitting at High Current Density: Current Status and Perspectives. *Nanoscale* **2021**, *13* (30), 12788–12817. https://doi.org/10.1039/D1NR02592A.

(133) Tüysüz, H.; Hwang, Y. J.; Khan, S. B.; Asiri, A. M.; Yang, P. Mesoporous Co3O4 as an Electrocatalyst for Water Oxidation. *Nano Res.* **2013**, *6* (1), 47–54. https://doi.org/10.1007/s12274-012-0280-8.

(134) Wang, Y.; Zhou, T.; Jiang, K.; Da, P.; Peng, Z.; Tang, J.; Kong, B.; Cai, W.-B.; Yang, Z.; Zheng, G. Reduced Mesoporous Co_3O_4 Nanowires as Efficient Water Oxidation Electrocatalysts and Supercapacitor Electrodes. *Adv. Energy Mater.* **2014**, *4* (16), 1400696. https://doi.org/10.1002/aenm.201400696.

(135) Liu, S. Controlled Synthesis of Co_3O_4 Electrocatalysts with Different Morphologies and Their Application for Oxygen Evolution Reaction. *Int. J. Electrochem. Sci.* **2018**, 3843–3854. https://doi.org/10.20964/2018.04.54.

(136) Xu, L.; Jiang, Q.; Xiao, Z.; Li, X.; Huo, J.; Wang, S.; Dai, L. Plasma-Engraved Co_3O_4 Nanosheets with Oxygen Vacancies and High Surface Area for the Oxygen Evolution Reaction. *Angew. Chemie Int. Ed.* **2016**, *55* (17), 5277–5281. https://doi.org/10.1002/anie.201600687.

(137) Yao, X.; Wang, X.; Sun, L.; Li, L.; Kan, E.; Ouyang, B.; Zhang, W. Popcorn-like Co_3O_4 Nanoparticles Confined in a Three-Dimensional Hierarchical N-Doped Carbon Nanotube Network as a Highly-Efficient Trifunctional Electrocatalyst for Zinc–air Batteries and Water Splitting Devices. *Inorg. Chem. Front.* **2022**, *9* (11), 2517–2529. https://doi.org/10.1039/D2QI00261B.

(138) Loni, E.; Shokuhfar, A.; Siadati, M. H. Cobalt-Based Electrocatalysts for Water Splitting: An Overview. *Catal. Surv. from Asia* **2021**, *25* (2), 114–147. https://doi.org/10.1007/s10563-021-09329-5.

(139) Li, A.; Sun, Y.; Yao, T.; Han, H. Earth-Abundant Transition-Metal-Based Electrocatalysts for Water Electrolysis to Produce Renewable Hydrogen. *Chem. – A Eur. J.* **2018**, *24* (69), 18334–18355. https://doi.org/10.1002/chem.201803749.

(140) Najafpour, M. M.; Renger, G.; Hołyńska, M.; Moghaddam, A. N.; Aro, E.-M.; Carpentier, R.; Nishihara, H.; Eaton-Rye, J. J.; Shen, J.-R.; Allakhverdiev, S. I. Manganese Compounds as Water-Oxidizing Catalysts: From the Natural Water-Oxidizing Complex to Nanosized Manganese Oxide Structures. *Chem. Rev.* **2016**, *116* (5), 2886–2936.

https://doi.org/10.1021/acs.chemrev.5b00340.

(141) Meng, Y.; Song, W.; Huang, H.; Ren, Z.; Chen, S.-Y.; Suib, S. L. Structure–Property Relationship of Bifunctional MnO_2 Nanostructures: Highly Efficient, Ultra-Stable Electrochemical Water Oxidation and Oxygen Reduction Reaction Catalysts Identified in Alkaline Media. *J. Am. Chem. Soc.* **2014**, *136* (32), 11452–11464. https://doi.org/10.1021/ja505186m.

(142) Heidari, S.; Singh, J. P.; Feizi, H.; Bagheri, R.; Chae, K. H.; Song, Z.; Khatamian, M.; Najafpour, M. M. Electrochemical Water Oxidation by Simple Manganese Salts. *Sci. Rep.* **2019**, *9* (1), 7749. https://doi.org/10.1038/s41598-019-44001-z.

(143) Melder, J.; Bogdanoff, P.; Zaharieva, I.; Fiechter, S.; Dau, H.; Kurz, P. Water-Oxidation Electrocatalysis by Manganese Oxides: Syntheses, Electrode Preparations, Electrolytes and Two Fundamental Questions. *Zeitschrift für Phys. Chemie* **2020**, *234* (5), 925–978. https://doi.org/10.1515/zpch-2019-1491.

(144) Liu, X.; Liu, W.; Ko, M.; Park, M.; Kim, M. G.; Oh, P.; Chae, S.; Park, S.; Casimir, A.; Wu, G.; Cho, J. Metal (Ni, Co)-Metal Oxides/Graphene Nanocomposites as Multifunctional Electrocatalysts. *Adv. Funct. Mater.* **2015**, *25* (36), 5799–5808. https://doi.org/10.1002/adfm.201502217.

(145) Louie, M. W.; Bell, A. T. An Investigation of Thin-Film Ni–Fe Oxide Catalysts for the Electrochemical Evolution of Oxygen. *J. Am. Chem. Soc.* **2013**, *135* (33). https://doi.org/10.1021/ja405351s.

(146) Qayum, A.; Peng, X.; Yuan, J.; Qu, Y.; Zhou, J.; Huang, Z.; Xia, H.; Liu, Z.; Tan, D. Q.; Chu, P. K.; Lu, F.; Hu, L. Highly Durable and Efficient Ni-FeO_x/$FeNi_3$ Electrocatalysts Synthesized by a Facile *In Situ* Combustion-Based Method for Overall Water Splitting with Large Current Densities. *ACS Appl. Mater. Interfaces* **2022**, *14* (24), 27842–27853. https://doi.org/10.1021/acsami.2c04562.

(147) Lee, W. H.; Han, M. H.; Lee, U.; Chae, K. H.; Kim, H.; Hwang, Y. J.; Min, B. K.; Choi, C. H.; Oh, H.-S. Oxygen Vacancies Induced NiFe-Hydroxide as a Scalable, Efficient, and Stable Electrode for Alkaline Overall Water Splitting. *ACS Sustain. Chem. Eng.* **2020**, *8* (37), 14071–14081. https://doi.org/10.1021/acssuschemeng.0c04542.

(148) Bodhankar, P. M.; Sarawade, P. B.; Singh, G.; Vinu, A.; Dhawale, D. S. Recent Advances in Highly Active Nanostructured NiFe LDH Catalyst for Electrochemical Water Splitting. *J.*

Mater. Chem. A **2021**, *9* (6), 3180–3208. https://doi.org/10.1039/D0TA10712C.

(149) Buccheri, B.; Ganci, F.; Patella, B.; Aiello, G.; Mandin, P.; Inguanta, R. Ni-Fe Alloy Nanostructured Electrodes for Water Splitting in Alkaline Electrolyser. *Electrochim. Acta* **2021**, *388*, 138588. https://doi.org/10.1016/j.electacta.2021.138588.

(150) Liang, C.; Zou, P.; Nairan, A.; Zhang, Y.; Liu, J.; Liu, K.; Hu, S.; Kang, F.; Fan, H. J.; Yang, C. Exceptional Performance of Hierarchical Ni–Fe Oxyhydroxide@NiFe Alloy Nanowire Array Electrocatalysts for Large Current Density Water Splitting. *Energy Environ. Sci.* **2020**, *13* (1), 86–95. https://doi.org/10.1039/C9EE02388G.

(151) Gong, M.; Dai, H. A Mini Review of NiFe-Based Materials as Highly Active Oxygen Evolution Reaction Electrocatalysts. *Nano Res.* **2015**, *8* (1). https://doi.org/10.1007/s12274-014-0591-z.

(152) Bates, M. K.; Jia, Q.; Doan, H.; Liang, W.; Mukerjee, S. Charge-Transfer Effects in Ni–Fe and Ni–Fe–Co Mixed-Metal Oxides for the Alkaline Oxygen Evolution Reaction. *ACS Catal.* **2016**, *6* (1), 155–161. https://doi.org/10.1021/acscatal.5b01481.

(153) Guzmán-Vargas, A.; Vazquez-Samperio, J.; Oliver-Tolentino, M. A.; Nava, N.; Castillo, N.; Macías-Hernández, M. J.; Reguera, E. Influence of Cobalt on Electrocatalytic Water Splitting in NiCoFe Layered Double Hydroxides. *J. Mater. Sci.* **2018**, *53* (6), 4515–4526. https://doi.org/10.1007/s10853-017-1882-z.

(154) Jeung, Y.; Jung, H.; Kim, D.; Roh, H.; Lim, C.; Han, J. W.; Yong, K. 2D-Structured V-Doped Ni(Co,Fe) Phosphides with Enhanced Charge Transfer and Reactive Sites for Highly Efficient Overall Water Splitting Electrocatalysts. *J. Mater. Chem. A* **2021**, *9* (20), 12203–12213. https://doi.org/10.1039/D1TA02149D.

(155) Xu, S.; Zhao, H.; Li, T.; Liang, J.; Lu, S.; Chen, G.; Gao, S.; Asiri, A. M.; Wu, Q.; Sun, X. Iron-Based Phosphides as Electrocatalysts for the Hydrogen Evolution Reaction: Recent Advances and Future Prospects. *J. Mater. Chem. A* **2020**, *8* (38), 19729–19745. https://doi.org/10.1039/D0TA05628F.

(156) Deng, R.; Guo, M.; Wang, C.; Zhang, Q. Recent Advances in Cobalt Phosphide-Based Materials for Electrocatalytic Water Splitting: From Catalytic Mechanism and Synthesis Method to Optimization Design. *Nano Mater. Sci.* **2022**. https://doi.org/10.1016/j.nanoms.2022.04.003.

(157) Zhou, J.; Huang, C.; Zhou, Q.; Xie, Y.; Yang, L.; Yu, L.; Yu, Y. Electronic Structure

Regulation of Nickel Phosphide for Efficient Overall Water Splitting. *Inorg. Chem.* **2022**, *61* (24), 9318–9327. https://doi.org/10.1021/acs.inorgchem.2c01070.

(158) Salem, K. E.; Saleh, A. A.; Khedr, G. E.; Shaheen, B. S.; Allam, N. K. Unveiling the Optimal Interfacial Synergy of Plasma Modulated Trimetallic Mn-Ni-Co Phosphides: Tailoring Deposition Ratio for Complementary Water Splitting. *Energy Environ. Mater.* **2021**, 1–13. https://doi.org/10.1002/eem2.12324.

(159) Woldetinsay, M.; Soreta, T. R.; Maiyalagan, T.; Femi, O. E. Effect of Support Material on the Electrocatalytic Activity of Palladium Nanoparticle toward Hydrogen Evolution Reaction. *Mater. Res. Express* **2021**, *8* (2), 025501. https://doi.org/10.1088/2053-1591/abdf1c.

(160) Sharma, S.; Pollet, B. G. Support Materials for PEMFC and DMFC Electrocatalysts—A Review. *J. Power Sources* **2012**, *208*, 96–119. https://doi.org/10.1016/j.jpowsour.2012.02.011.

(161) Malaie, K.; Heydari, Z.; Brousse, T. Methods—On the Reliability of the Electrochemical Data Recorded on Nickel Foam in Alkaline Solution: The Illusive Surface Oxide Layer. *J. Electrochem. Soc.* **2021**, *168* (12), 120547. https://doi.org/10.1149/1945-7111/ac4129.

(162) Zhang, Y.; Fu, C.; Fan, J.; Lv, H.; Hao, W. Preparation of Ti@NiB Electrode via Electroless Plating toward High-Efficient Alkaline Simulated Seawater Splitting. *J. Electroanal. Chem.* **2021**, *901*, 115761. https://doi.org/10.1016/j.jelechem.2021.115761.

(163) Ahsan, A.; Santiago, A. R. P.; Hong, Y.; Zhang, N.; Cano, M.; Rodriguez-castellon, E.; Echegoyen, L.; Sreenivasan, S. T.; Noveron, J. C. Tuning of Trifunctional NiCu Bimetallic Nanoparticles Con Fi Ned in a Porous Carbon Network with Surface Composition and Local Structural Distortions for the Electrocatalytic Oxygen Reduction , Oxygen and Hydrogen Evolution Reactions. **2020**. https://doi.org/10.1021/jacs.0c06960.

(164) Kano, E.; Kvashnin, D. G.; Sakai, S.; Chernozatonskii, L. A.; Sorokin, P. B.; Hashimoto, A.; Takeguchi, M. One-Atom-Thick 2D Copper Oxide Clusters on Graphene. *Nanoscale* **2017**, *9* (11), 3980–3985. https://doi.org/10.1039/c6nr06874j.

(165) El-Nahas, A. M.; Khedr, G. E.; Emam, S. M. Thermodynamic and Kinetic Stability of Magnesium Dication Solvated by Tetramethylethylenediamine. *Comput. Theor. Chem.* **2011**, *978* (1–3), 104–109. https://doi.org/10.1016/j.comptc.2011.09.042.

(166) Westbroek, P.; Priniotakis, G.; Kiekens, P. *Analytical Electrochemistry in Textiles*; Woodhead

Publishing Limited, 2005. https://doi.org/10.1533/9781845690878.

(167) Naveen, M. H.; Khan, R.; Bang, J. H. Gold Nanoclusters as Electrocatalysts: Atomic Level Understanding from Fundamentals to Applications. *Chem. Mater.* **2021**, *33* (19), 7595–7612. https://doi.org/10.1021/acs.chemmater.1c02112.

(168) Sylvestre, J.-P.; Kabashin, A. V.; Sacher, E.; Meunier, M.; Luong, J. H. T. Nanoparticle Size Reduction during Laser Ablation in Aqueous Solutions of Cyclodextrins. *Phot. Process. Microelectron. Photonics III* **2004**, *5339* (January 2014), 84. https://doi.org/10.1117/12.525499.

(169) Smirnov, M. Y.; Kalinkin, A. V.; Vovk, E. I.; Bukhtiyarov, V. I. Analysis of the Oxidation State of Platinum Particles in Supported Catalysts by Double Differentiation of XPS Lines. *J. Struct. Chem.* **2016**, *57* (6), 1127–1133. https://doi.org/10.1134/S002247661606010X.

(170) Yi, Y.; Weinberg, G.; Prenzel, M.; Greiner, M.; Heumann, S.; Becker, S.; Schlögl, R. Electrochemical Corrosion of a Glassy Carbon Electrode. *Catal. Today* **2017**, *295*, 32–40. https://doi.org/10.1016/j.cattod.2017.07.013.

(171) Park, H. J.; Cha, J.; Choi, M.; Kim, J. H.; Tay, R. Y.; Teo, E. H. T.; Park, N.; Hong, S.; Lee, Z. One-Dimensional Hexagonal Boron Nitride Conducting Channel. *Sci. Adv.* **2020**, *6* (10). https://doi.org/10.1126/sciadv.aay4958.

(172) Liu, Y.; Ali, R.; Jiao, W.; Yin, L.; Mu, C.; Jian, X. Graphene-Decorated Boron − Carbon − Nitride-Based Metal-Free Catalysts for an Enhanced Hydrogen Evolution Reaction. **2021**. https://doi.org/10.1021/acsaem.1c00238.

(173) Shu, J.; Cheng, S.; Xia, H.; Zhang, L.; Peng, J.; Li, C.; Zhang, S. Copper Loaded on Activated Carbon as an Efficient Adsorbent for Removal of Methylene Blue. *RSC Adv.* **2017**, *7* (24), 14395–14405. https://doi.org/10.1039/c7ra00287d.

(174) FTIR-Copper(II) α-Amino Acid Chelates in ATR-FTIR Spectra, 2019.Pdf.

(175) Zheng, Y.; Jiao, Y.; Ge, L.; Jaroniec, M.; Qiao, S. Z. Two-Step Boron and Nitrogen Doping in Graphene for Enhanced Synergistic Catalysis. *Angew. Chemie - Int. Ed.* **2013**, *52* (11), 3110–3116. https://doi.org/10.1002/anie.201209548.

(176) Nanoscale, C.; Qin, L.; Yu, J.; Kuang, S.; Bai, X. Nanoscale Few-Atomic-Layered Boron Carbonitride Nanosheets Prepared by Chemical Vapor Deposition. **2012**, *2*, 120–123. https://doi.org/10.1039/c1nr11387a.

(177) Lei, W. Porous Boron Carbon Nitride Nanosheets As. **2017**.

https://doi.org/10.1021/acsenergylett.6b00602.

(178) Ci, L.; Song, L.; Jin, C.; Jariwala, D.; Wu, D.; Li, Y.; Srivastava, A. Atomic Layers of Hybridized Boron Nitride and Graphene Domains. *Nat. Mater.* **2010**, *9* (5), 430–435. https://doi.org/10.1038/nmat2711.

(179) Lee, Y. T.; Park, J.; Choi, Y. S.; Ryu, H.; Lee, H. J. Temperature-Dependent Growth of Vertically Aligned Carbon Nanotubes in the Range 800−1100 °C. *J. Phys. Chem. B* **2002**, *106* (31), 7614–7618. https://doi.org/10.1021/jp020488l.

(180) Iyyamperumal, E.; Wang, S.; Dai, L. Vertically Aligned BCN Nanotubes with High Capacitance. *ACS Nano* **2012**, *6* (6), 5259–5265. https://doi.org/10.1021/nn301044v.

(181) Dou, S.; Huang, X.; Ma, Z.; Wu, J.; Wang, S. A Simple Approach to the Synthesis of BCN Graphene with High Capacitance. *Nanotechnology* **2015**, *26* (4), 045402. https://doi.org/10.1088/0957-4484/26/4/045402.

(182) Liu, X.; Wang, Y.; Dong, L.; Chen, X.; Xin, G.; Zhang, Y.; Zang, J. One-Step Synthesis of Shell/Core Structural Boron and Nitrogen Co-Doped Graphitic Carbon/Nanodiamond as Efficient Electrocatalyst for the Oxygen Reduction Reaction in Alkaline Media. *Electrochim. Acta* **2016**, *194*, 161–167. https://doi.org/10.1016/j.electacta.2016.02.002.

(183) Ling, Z.; Wang, Z.; Zhang, M.; Yu, C.; Wang, G.; Dong, Y.; Liu, S.; Wang, Y.; Qiu, J. Sustainable Synthesis and Assembly of Biomass-Derived B/N Co-Doped Carbon Nanosheets with Ultrahigh Aspect Ratio for High-Performance Supercapacitors. *Adv. Funct. Mater.* **2016**, *26* (1), 111–119. https://doi.org/10.1002/adfm.201504004.

(184) Jiang, Z.; Zhao, X.; Tian, X.; Luo, L.; Fang, J.; Gao, H.; Jiang, Z.-J. Hydrothermal Synthesis of Boron and Nitrogen Codoped Hollow Graphene Microspheres with Enhanced Electrocatalytic Activity for Oxygen Reduction Reaction. *ACS Appl. Mater. Interfaces* **2015**, *7* (34), 19398–19407. https://doi.org/10.1021/acsami.5b05585.

(185) Lei, W.; Portehault, D.; Dimova, R.; Antonietti, M. Boron Carbon Nitride Nanostructures from Salt Melts: Tunable Water-Soluble Phosphors. *J. Am. Chem. Soc.* **2011**, *133* (18), 7121–7127. https://doi.org/10.1021/ja200838c.

(186) Li, X.; Liu, G.; Popov, B. N. Activity and Stability of Non-Precious Metal Catalysts for Oxygen Reduction in Acid and Alkaline Electrolytes. *J. Power Sources* **2010**, *195* (19), 6373–6378. https://doi.org/10.1016/j.jpowsour.2010.04.019.

(187) Zhao, D.; Sun, K.; Cheong, W. C.; Zheng, L.; Zhang, C.; Liu, S.; Cao, X.; Wu, K.; Pan, Y.;

Zhuang, Z.; Hu, B.; Wang, D.; Peng, Q.; Chen, C.; Li, Y. Synergistically Interactive Pyridinic-N–MoP Sites: Identified Active Centers for Enhanced Hydrogen Evolution in Alkaline Solution. *Angew. Chemie - Int. Ed.* **2020**, *59* (23), 8982–8990. https://doi.org/10.1002/anie.201908760.

(188) Gao, Y.; Yang, F.; Yu, Q.; Fan, R.; Yang, M.; Rao, S.; Lan, Q.; Yang, Z. Three-Dimensional Porous Cu @ Cu_2O Aerogels for Direct Voltammetric Sensing of Glucose. **2019**.

(189) Xing, X.; Song, Y.; Jiang, W.; Zhang, X. Sustainable Energy & Fuels CuFe–P from a Prussian Blue Analogue as an Electrocatalyst for e Ffi Cient Full Water Splitting †. **2020**, 3985–3991. https://doi.org/10.1039/d0se00402b.

(190) Parvez, K.; Li, R.; Puniredd, S. R.; Hernandez, Y.; Hinkel, F.; Wang, S.; Feng, X.; Mu, K.; Engineering, C.; Road, D. Electrochemically Exfoliated Graphene as Solution-Processable , Highly Conductive Electrodes For. **2013**, No. 4, 3598–3606.

(191) Shan, A.; Teng, X.; Zhang, Y.; Zhang, P.; Xu, Y.; Liu, C.; Li, H.; Ye, H.; Wang, R. Interfacial Electronic Structure Modulation of Pt-MoS_2 Heterostructure for Enhancing Electrocatalytic Hydrogen Evolution Reaction. *Nano Energy* **2022**, *94*, 106913. https://doi.org/10.1016/j.nanoen.2021.106913.

(192) Ali, B. A.; Biby, A. H.; Allam, N. K. Fullerene C_{76}: An Unexplored Superior Electrode Material with Wide Operating Potential Window for High-Performance Supercapacitors. *ChemElectroChem* **2020**, *7* (7), 1672–1678. https://doi.org/10.1002/celc.202000192.

(193) Ţucureanu, V.; Matei, A.; Avram, A. M. FTIR Spectroscopy for Carbon Family Study. *Crit. Rev. Anal. Chem.* **2016**, *46* (6), 502–520. https://doi.org/10.1080/10408347.2016.1157013.

(194) Diwany, F. A. El; Ali, B. A.; Allam, N. K. All-Vanadium Redox Flow Batteries †. **2020**, No. June. https://doi.org/10.1039/D0CC03544K.

(195) Kim, Y. H.; Jin, X.; Hwang, S.-J. Fullerene as an Efficient Hybridization Matrix for Exploring High-Performance Layered-Double-Hydroxide-Based Electrodes. *J. Mater. Chem. A* **2019**, *7* (18), 10971–10979. https://doi.org/10.1039/C9TA01532A.

(196) Huang, Y.; Zhang, X.; Ma, Z.; Li, W.; Zhou, Y.; Zhou, J.; Zheng, W.; Sun, C. Q. Size, Separation, Structural Order and Mass Density of Molecules Packing in Water and Ice. *Sci. Rep.* **2013**, *3* (1), 3005. https://doi.org/10.1038/srep03005.

(197) Tai, F. C.; Lee, S. C.; Wei, C. H.; Tyan, S. L. Correlation between ID/IG Ratio from Visible Raman Spectra and Sp^2 /Sp^3 Ratio from XPS Spectra of Annealed Hydrogenated DLC Film

Correlation between I D = I G Ratio from Visible Raman Spectra and Sp^2 / Sp^3 Ratio from XPS Spectra of Annealed Hydrogena. **2006**, No. July. https://doi.org/10.2320/matertrans.47.1847.

(198) Vijayakumar, M.; Wang, W.; Nie, Z.; Sprenkle, V.; Hu, J. Elucidating the Higher Stability of Vanadium (V) Cations in Mixed Acid Based Redox Fl Ow Battery Electrolytes. *J. Power Sources* **2013**, *241*, 173–177. https://doi.org/10.1016/j.jpowsour.2013.04.072.

(199) Park, S. M.; Kim, J. H.; Skyllas-kazacos, M. As Featured In : **2015**. https://doi.org/10.1039/c5ta02613j.

(200) Singh, C.; S., N.; Jana, A.; Mishra, A. K.; Paul, A. Proton Conduction through Oxygen Functionalized Few-Layer Graphene. *Chem. Commun.* **2016**, *52* (85), 12661–12664. https://doi.org/10.1039/C6CC07231C.

(201) Han, P.; Yue, Y.; Liu, Z.; Xu, W.; Zhang, L.; Xu, H.; Dong, S.; Cui, G. Graphene Oxide Nanosheets/Multi-Walled Carbon Nanotubes Hybrid as an Excellent Electrocatalytic Material towards VO^{2+}/VO^{2+} Redox Couples for Vanadium Redox Flow Batteries. *Energy Environ. Sci.* **2011**, *4* (11), 4710. https://doi.org/10.1039/c1ee01776d.

(202) Strauss, V.; Marsh, K.; Kowal, M. D.; El-Kady, M.; Kaner, R. B. A Simple Route to Porous Graphene from Carbon Nanodots for Supercapacitor Applications. *Adv. Mater.* **2018**, *30* (8), 1704449. https://doi.org/10.1002/adma.201704449.

(203) Oh, Y. J.; Yoo, J. J.; Kim, Y. Il; Yoon, J. K.; Yoon, H. N.; Kim, J.-H.; Park, S. Bin. Oxygen Functional Groups and Electrochemical Capacitive Behavior of Incompletely Reduced Graphene Oxides as a Thin-Film Electrode of Supercapacitor. *Electrochim. Acta* **2014**, *116*, 118–128. https://doi.org/10.1016/j.electacta.2013.11.040.

(204) Singh, R. K.; Kumar, R.; Singh, D. P. Graphene Oxide: Strategies for Synthesis, Reduction and Frontier Applications. *RSC Adv.* **2016**, *6* (69), 64993–65011. https://doi.org/10.1039/C6RA07626B.

(205) Ferrari, A. C.; Robertson, J. Interpretation of Raman Spectra of Disordered and Amorphous Carbon. *Phys. Rev. B* **2000**, *61* (20), 14095–14107. https://doi.org/10.1103/PhysRevB.61.14095.

(206) Pimenta, M. A.; Dresselhaus, G.; Dresselhaus, M. S.; Cançado, L. G.; Jorio, A.; Saito, R. Studying Disorder in Graphite-Based Systems by Raman Spectroscopy. *Phys. Chem. Chem. Phys.* **2007**, *9* (11), 1276–1290. https://doi.org/10.1039/B613962K.

(207) Shin, H.-C.; Liu, M. Copper Foam Structures with Highly Porous Nanostructured Walls. *Chem. Mater.* **2004**, *16* (25), 5460–5464. https://doi.org/10.1021/cm048887b.

(208) Shin, H.-C.; Dong, J.; Liu, M. Nanoporous Structures Prepared by an Electrochemical Deposition Process. *Adv. Mater.* **2003**, *15* (19), 1610–1614. https://doi.org/10.1002/adma.200305160.

(209) Xia, X. H.; Tu, J. P.; Zhang, Y. Q.; Mai, Y. J.; Wang, X. L.; Gu, C. D.; Zhao, X. B. Three-Dimentional Porous Nano-Ni/Co(OH) 2 Nanoflake Composite Film: A Pseudocapacitive Material with Superior Performance. *J. Phys. Chem. C* **2011**, *115* (45), 22662–22668. https://doi.org/10.1021/jp208113j.

(210) Ali, G. A. M.; Yusoff, M. M.; Ng, Y. H.; Lim, H. N.; Chong, K. F. Potentiostatic and Galvanostatic Electrodeposition of Manganese Oxide for Supercapacitor Application: A Comparison Study. *Curr. Appl. Phys.* **2015**, *15* (10), 1143–1147. https://doi.org/10.1016/j.cap.2015.06.022.

(211) Khan, M.; Tahir, M. N.; Adil, S. F.; Khan, H. U.; Siddiqui, M. R. H.; Al-Warthan, A. A.; Tremel, W. Graphene Based Metal and Metal Oxide Nanocomposites: Synthesis, Properties and Their Applications. *J. Mater. Chem. A* **2015**, *3* (37), 18753–18808. https://doi.org/10.1039/c5ta02240a.

(212) Xiao, C.; Li, Y.; Lu, X.; Zhao, C. Bifunctional Porous NiFe/NiCo2O4/Ni Foam Electrodes with Triple Hierarchy and Double Synergies for Efficient Whole Cell Water Splitting. *Adv. Funct. Mater.* **2016**, *26* (20), 3515–3523. https://doi.org/10.1002/adfm.201505302.

(213) Zhan, K.; Feng, C.; Feng, X.; Zhao, D.; Yue, S.; Li, Y.; Jiao, Q.; Li, H.; Zhao, Y. Iron-Doped Nickel Cobalt Phosphide Nanoarrays with Urchin-like Structures as High-Performance Electrocatalysts for Oxygen Evolution Reaction. *ACS Sustain. Chem. Eng.* **2020**, *8* (16), 6273–6281. https://doi.org/10.1021/acssuschemeng.9b07781.

(214) Zhang, Q.; Yan, D.; Nie, Z.; Qiu, X.; Wang, S.; Yuan, J.; Su, D.; Wang, G.; Wu, Z. Iron-Doped NiCoP Porous Nanosheet Arrays as a Highly Efficient Electrocatalyst for Oxygen Evolution Reaction. *ACS Appl. Energy Mater.* **2018**, *1* (2), 571–579. https://doi.org/10.1021/acsaem.7b00143.

(215) Yan, D.; Li, Y.; Huo, J.; Chen, R.; Dai, L.; Wang, S. Defect Chemistry of Nonprecious-Metal Electrocatalysts for Oxygen Reactions. *Adv. Mater.* **2017**, *29* (48), 1–20. https://doi.org/10.1002/adma.201606459.

(216) Gong, K.; Xu, F.; Grunewald, J. B.; Ma, X.; Zhao, Y.; Gu, S.; Yan, Y. All-Soluble All-Iron Aqueous Redox-Flow Battery. *ACS Energy Lett.* **2016**, *1* (1), 89–93. https://doi.org/10.1021/acsenergylett.6b00049.

(217) Salem, K. E.; Saleh, A. A.; Khedr, G. E.; Shaheen, B. S.; Allam, N. K. Unveiling the Optimal Interfacial Synergy of Plasma-Modulated Trimetallic Mn-Ni-Co Phosphides: Tailoring Deposition Ratio for Complementary Water Splitting. *ENERGY Environ. Mater.* **2022**. https://doi.org/10.1002/eem2.12324.

(218) Kanan, M. W.; Nocera, D. G. In Situ Formation of an Oxygen-Evolving Catalyst in Neutral Water Containing Phosphate and Co^{2+}. *Science (80-.).* **2008**, *321* (5892), 1072–1075. https://doi.org/10.1126/science.1162018.

(219) Saleh, A. A.; Ahmed, N.; Biby, A. H.; Allam, N. K. Supercapattery Electrode Materials by Design: Plasma-Induced Defect Engineering of Bimetallic Oxyphosphides for Energy Storage. *J. Colloid Interface Sci.* **2021**, *603*, 478–490. https://doi.org/10.1016/j.jcis.2021.06.125.

(220) Das, J. K.; Samantara, A. K.; Satyarthy, S.; Rout, C. S.; Behera, J. N. Three-Dimensional NiCoP Hollow Spheres: An Efficient Electrode Material for Hydrogen Evolution Reaction and Supercapacitor Applications. *RSC Adv.* **2020**, *10* (8), 4650–4656. https://doi.org/10.1039/C9RA09714G.

(221) Adam, A.; Suliman, M. H.; Siddiqui, M. N.; Yamani, Z. H.; Merzougui, B.; Qamar, M. Interconnected Hollow Cobalt Phosphide Grown on Carbon Nanotubes for Hydrogen Evolution Reaction. *ACS Appl. Mater. Interfaces* **2018**, *10* (35), 29407–29416. https://doi.org/10.1021/acsami.8b03427.

(222) Jeon, T. H.; Choi, W.; Park, H. Cobalt–phosphate Complexes Catalyze the Photoelectrochemical Water Oxidation of $BiVO_4$ Electrodes. *Phys. Chem. Chem. Phys.* **2011**, *13* (48), 21392. https://doi.org/10.1039/c1cp23135a.

(223) Tian, J.; Liu, Q.; Asiri, A. M.; Sun, X. Self-Supported Nanoporous Cobalt Phosphide Nanowire Arrays: An Efficient 3D Hydrogen-Evolving Cathode over the Wide Range of PH 0–14. *J. Am. Chem. Soc.* **2014**, *136* (21), 7587–7590. https://doi.org/10.1021/ja503372r.

(224) Chen, Y. S.; Kang, J. F.; Chen, B.; Gao, B.; Liu, L. F.; Liu, X. Y.; Wang, Y. Y.; Wu, L.; Yu, H. Y.; Wang, J. Y.; Chen, Q.; Wang, E. G. Microscopic Mechanism for Unipolar Resistive Switching Behaviour of Nickel Oxides. *J. Phys. D. Appl. Phys.* **2012**, *45* (6), 065303.

https://doi.org/10.1088/0022-3727/45/6/065303.

(225) Saleh, A. A.; Sayed, D. M.; Nagle-Cocco, L. A. V.; Divitini, G.; Ghanem, L. G.; Ducati, C.; Allam, N. K. Deciphering the In Situ Surface Reconstruction of Supercapacitive Bimetallic Ni-Co Oxyphosphide during Electrochemical Activation Using Multivariate Statistical Analyses. *ACS Appl. Energy Mater.* **2022**, *5* (6), 7661–7673. https://doi.org/10.1021/acsaem.2c01122.

(226) Katkar, P. K.; Marje, S. J.; Pujari, S. S.; Khalate, S. A.; Deshmukh, P. R.; Patil, U. M. Single-Pot Hydrothermal Synthesis of Manganese Phosphate Microrods as a Cathode Material for Highly Stable Flexible Solid-State Symmetric Supercapacitors. *Synth. Met.* **2020**, *267*, 116446. https://doi.org/10.1016/j.synthmet.2020.116446.

(227) Yang, H.; Yuan, M.; Wang, D.; Sun, Z.; Li, H.; Sun, G. 3D Cross-Linked Structure of Manganese Nickel Phosphide Ultrathin Nanosheets: Electronic Structure Optimization for Efficient Bifunctional Electrocatalysts. *ACS Appl. Energy Mater.* **2021**, *4* (8), 8563–8571. https://doi.org/10.1021/acsaem.1c01756.

(228) Cho, G.; Kim, H.; Park, Y. S.; Hong, Y.-K.; Ha, D.-H. Phase Transformation of Iron Phosphide Nanoparticles for Hydrogen Evolution Reaction Electrocatalysis. *Int. J. Hydrogen Energy* **2018**, *43* (24), 11326–11334. https://doi.org/10.1016/j.ijhydene.2018.02.197.

(229) Zhang, Z.; Hao, J.; Yang, W.; Lu, B.; Tang, J. Modifying Candle Soot with FeP Nanoparticles into High-Performance and Cost-Effective Catalysts for the Electrocatalytic Hydrogen Evolution Reaction. *Nanoscale* **2015**, *7* (10), 4400–4405. https://doi.org/10.1039/C4NR07436J.

(230) Yao, Q.; Zhou, X.; Xiao, S.; Chen, J.; Abdelhafeez, I. A.; Yu, Z.; Chu, H.; Zhang, Y. Amorphous Nickel Phosphide as a Noble Metal-Free Cathode for Electrochemical Dechlorination. *Water Res.* **2019**, *165*, 114930. https://doi.org/10.1016/j.watres.2019.114930.

(231) Lin, L.; Chen, M.; Wu, L. Hierarchical MoP/NiFeP Hybrid Hollow Spheres as Highly Efficient Bifunctional Electrocatalysts for Overall Water Splitting. *Mater. Chem. Front.* **2021**, *5* (1), 375–385. https://doi.org/10.1039/D0QM00635A.

(232) Perez Bakovic, S. I.; Acharya, P.; Watkins, M.; Thornton, H.; Hou, S.; Greenlee, L. F. Electrochemically Active Surface Area Controls HER Activity for FexNi100−x Films in

Alkaline Electrolyte. *J. Catal.* **2021**, *394*, 104–112. https://doi.org/10.1016/j.jcat.2020.12.037.

(233) Kibsgaard, J.; Jaramillo, T. F. Molybdenum Phosphosulfide: An Active, Acid-Stable, Earth-Abundant Catalyst for the Hydrogen Evolution Reaction. *Angew. Chemie Int. Ed.* **2014**, *53* (52), 14433–14437. https://doi.org/10.1002/anie.201408222.

(234) Liang, H.; Gandi, A. N.; Anjum, D. H.; Wang, X.; Schwingenschlögl, U.; Alshareef, H. N. Plasma-Assisted Synthesis of NiCoP for Efficient Overall Water Splitting. *Nano Lett.* **2016**, *16* (12), 7718–7725. https://doi.org/10.1021/acs.nanolett.6b03803.

(235) Sivanantham, A.; Ganesan, P.; Shanmugam, S. Hierarchical NiCo 2 S 4 Nanowire Arrays Supported on Ni Foam: An Efficient and Durable Bifunctional Electrocatalyst for Oxygen and Hydrogen Evolution Reactions. *Adv. Funct. Mater.* **2016**, *26* (26), 4661–4672. https://doi.org/10.1002/adfm.201600566.

(236) Surendranath, Y.; Kanan, M. W.; Nocera, D. G. Mechanistic Studies of the Oxygen Evolution Reaction by a Cobalt-Phosphate Catalyst at Neutral PH. *J. Am. Chem. Soc.* **2010**, *132* (46), 16501–16509. https://doi.org/10.1021/ja106102b.

(237) Riyajuddin, S.; Azmi, K.; Pahuja, M.; Kumar, S.; Maruyama, T.; Bera, C.; Ghosh, K. Super-Hydrophilic Hierarchical Ni-Foam-Graphene-Carbon Nanotubes-Ni_2 P–CuP_2 Nano-Architecture as Efficient Electrocatalyst for Overall Water Splitting. *ACS Nano* **2021**, *15* (3), 5586–5599. https://doi.org/10.1021/acsnano.1c00647.

(238) Liu, J.; Zheng, Y.; Jiao, Y.; Wang, Z.; Lu, Z.; Vasileff, A.; Qiao, S. NiO as a Bifunctional Promoter for RuO_2 toward Superior Overall Water Splitting. *Small* **2018**, *14* (16), 1704073. https://doi.org/10.1002/smll.201704073.